TUC

Technical University of Crete
School of Environmental Engineering

Physical processes of indoor aerosols in modern microenvironments

Doctoral Thesis by

Sofia Eirini Chatoutsidou

Chemical Engineer, Msc

Chania 2016

© Copyright by

Sofia Eirini Chatoutsidou

2016

All rights reserved

The present doctoral thesis was submitted within the postgraduate studies program «Environmental Engineering» at the School of Environmental Engineering in the Technical University of Crete and was supervised by prof. Mihalis Lazaridis. The thesis was carried out at the Norwegian Institute for Air Research (NILU) and was supported by the European Union 7th framework program HEXACOMM (*Human Exposure to Aerosol Contaminants in Modern Microenvironments*) FP7-PEOPLE-2012-ITN under grant agreement № 315760.

Phd Dissertation Committee:

Dr. M. Lazaridis, School of Environmental Engineering, Technical University of Crete (supervisor)

Dr. N. Kalogerakis, Professor, School of Environmental Engineering, Technical University of Crete

Dr. D. Kolokotsa, Assistant Professor, School of Environmental Engineering, Technical University of Crete

Dr. K. Eleftheriadis, Researcher, Institute of Nuclear Technology-Radiation Protection, N.C.S.R. "Demokritos", Athens, Greece

Dr. Y. Drossinos, Researcher, European Commission, Joint Research Centre, Ispra, Italy

Dr. T. Glytsos, School of Environmental Engineering, Technical University of Crete

Dr. E. Diapouli, Institute of Nuclear Technology-Radiation Protection, N.C.S.R. "Demokritos", Athens, Greece

Acknowledgments

I would like to express my thanks to many people that I have collaborated through the present thesis. Their contribution has been generous as well as crucial to the progress of the present the work.

Firstly, special appreciation and thanks goes to my supervisor Prof. Mihalis Lazaridis for giving me the opportunity to work in the phd position offered by NILU. Working with Mihalis was a great experience as his consecutive support and guidance has helped me to improve my work and widen my research. We had fruitful discussions on results and findings of my phd and his strong encouragement is unforgettable.

Profound gratitude goes to Yannis Drossinos who has been a great collaboration. As he was always dedicated to the goal of my research on resuspension, his insightful discussions and suggestions motivated me to work with precision, care and interest on the findings of the present thesis. His patience and attention to details only enlightened hazy components of the most demanding part of my phd.

I am also hugely appreciative to Kjetil Tørseth. He gave me a warm welcome coming to NILU and he always replied my e-mails and my queries very fast. He has been very supportive with administrative subjects and he was more than willing performing measurements in his office although using very noisy equipment.

Special mention goes to Jiří Smolík for his valuable comments and guidance for improving investigation of modeling results in the Baroque Library Hall campaign. I sincerely thank Jakub Ondráček and Vladimir Zdimal for providing the instruments for performing measurements in offices in Norway and their continuous support and advice on the experimental procedure and analysis of the results.

I would also like to thank the people from the Atmospheric Aerosol Laboratory in the Technical University of Crete. Norbert Serfozo for his essential help performing measurements in the lab and in several offices in the university, Thodoros Glytsos for the useful discussions, helping with measurements and for sharing his office the period I spend in Chania. Also Elena Mami-Galani for all her help (both personal and research related) during my secondment in Chania.

I am very grateful to all the people in NILU and my colleges in ATMOS for all the help and guidance they provided me during the last three years. Special thanks to Markus Fiebig and his great help during my first days in NILU.

Abstract

The work presented herein deals with characteristics of particle number and mass concentrations in modern workplace environments including modeling of the most significant physical processes indoors that lead to airborne particles. Accordingly, airborne particles that are not emitted by primary indoor sources, can be transported from outdoors or re-suspended from indoor surfaces.

In particular, measurement campaigns were conducted in offices in Kjeller, Norway and in Chania, Greece. Indoor and outdoor particle (number and mass) concentrations were measured simultaneously in several offices equipped with mechanical ventilation system. Each office was characterized by different occupational scheme, however, the results have shown that the outdoor environment plays an important role on indoor particle levels when the offices were vacant. In this case, outdoor fluctuations of both mass and number concentrations determined indoor particle fluctuations. Moreover, in the absence of a source emitting particles to the indoor air (e.g. printers), resuspension of the already existing particles on the indoor surfaces found to be the dominating origin of the airborne particles. Subsequently, particle infiltration characteristics and particle resuspension were modelled as the main contribution to the indoor air that are not associated with primary emissions.

Infiltration of particles through leaks and gaps in the building envelope is governed by particle dynamics. Accordingly, a mass balance model was applied to a set of particle number concentration data in a naturally ventilated building. The mass balance model assumed particle losses due to deposition on indoor surfaces and removal due to air exchange rate, whereas, the outdoor environment was considered as a source of infiltrated particles indoors. The model was used to determine the deposition rate and the penetration efficiency in 13 discrete size intervals ranging from 0.014 μm to 20 μm. Deposition was found to depend strongly on particle size with higher rates for ultrafine (0.014-0.1 μm) and coarse (3-20 μm) particles, whereas, penetration was not clearly related with size probably due to building characteristics.

The particle resuspension rate was obtained using a set of mass balance equations, one for the particle mass concentration of the indoor air and one for the dust loading on the floor. The mass balance model was applied to a set of experimental data for resuspension due to human walking. The resuspension rate was obtained under different dust loadings where results have shown that higher dust loading is not associated with higher resuspension rate. Moreover, the results suggested that resuspension of particles from indoor surfaces is easier for bigger particles.

Furthermore, a stochastic model of particle resuspension due to the act of a turbulent airflow was used to evaluate resuspension from a monolayer and a multilayer deposit. Intermolecular interactions between

the particle and the surface or between particles were modelled using the integrated Lennard-Jones potential. The resuspension rate was calculated by a kinetic force-balance approximation whereby particle detachment occurs when the instantaneous joint contribution of the lift and drag forces exceeds the total adhesive force of the particle-surface system. An enhanced aerodynamic removal process driven by the moments of the lift and drag forces was calculated. The role of particle size, surface roughness and particle electric charge was investigated in the case of a monolayer deposit. On the other hand, the impact of exposure time to the airflow and friction velocity induced by the airflow to the single-layer resuspension rate was studied for a multilayer deposit where particles sit on top of others.

An alternative resuspension mechanism is also presented where particles are detached due to an external vibrating force that acts normal on the surface and at a distance from the particle. Implementation of the force causes deformation into the body of the plate which propagates via elastic waves (bending waves). Momentum transfer through the plate to the particle causes particle oscillation in the vertical direction as long as particle mass inertia is overcome. Subsequently, particle detachment occurs when the force whereby the particle oscillates on the plate exceeds the adhesive force that binds the particle to the surface.

Table of contents

Acknowledgments iii
Abstract v
Table of contents vii

Chapter 1 Introduction to physical processes of particles in indoor environments

1.1 Introduction 1
1.2 Particle fundamentals 2
1.2.1 Particle size and shape 2
1.2.2 Chemical composition 3
1.2.3 Particle size distributions 4
1.3 Fundamentals of physical processes of indoor particles 6
1.4 Material balance model for indoor particle concentration 9
1.5 Objective of the present thesis 10
1.6 Contribution and novelty of the present thesis 11

Chapter 2 Characteristics of particle mass/number concentrations in modern offices

2.1 Introduction 12
2.2 Measurement of particle concentrations in offices in Norway 13
2.2.1 Location/office description 13
2.2.2 Experimental set up 15
2.2.3 Office occupation 16
2.2.4 Ventilation/Filters 17
2.2.5 Indoor and outdoor particle concentrations 18
2.2.5.1 Particle number concentrations 18
2.2.5.2 Particle mass concentrations 21
2.2.6 Influence of indoor/outdoor sources 23
2.2.6.1 Office A 24
2.2.6.2 Office B 26
2.2.7 I/O ratio 28
2.3 Measurement of particle concentrations in offices in Greece 30

2.3.1 Sampling site 30
2.3.2 Instrumentation 32
2.3.3 PN concentrations in Printer Room 33
2.3.4 PM concentrations in Printer Room 36
2.3.5 I\O ratio 38
2.3.6 Impact of printer emissions in other offices 40
2.3.7 Black carbon 43
2.4 Conclusions 44

Chapter 3 Modeling of particle infiltration characteristics

3.1 Introduction 46
3.2 Measurement site/Instrumentation 46
3.3 Mass balance model 48
3.4 Estimation of air exchange rate 49
3.5 Indoor and outdoor particle concentration 50
3.6 Indoor/Outdoor Ratio 52
3.7 Modeling of the indoor particle concentration 53
3.7.1 Methodology for estimating deposition rate and penetration efficiency 53
3.7.2 Averaged values of k and P 57
3.8 Infiltration factor and comparison with I/O ratio 60
3.9 Influence from indoor sources 62
3.10 Conclusions 64

Chapter 4 Particle resuspension rate in the indoor environment induced by human walking

4.1 Introduction 65
4.2 Laboratory experiments 65
4.2.1 Layout and instrumentation 65
4.2.2 Measurement protocol 67
4.3 Estimation of the resuspension rate 68
4.3.1 Resuspension rate model 68
4.3.2 Infiltration rate 70
4.3.3 Air exchange rate 71
4.4 Indoor particle number and mass concentrations 71

4.5 Indoor PM_{10} mass concentration at different dust loadings 74
4.6 Estimation of infiltration rate 75
4.7 Dust loading 76
4.8 Resuspension rate 78
4.8.1 Influence of environmental factors 80
4.8.2 Resuspension rate time dependence 80
4.9 Indoor model performance 81
4.10 Conclusions 82

Chapter 5 Modeling of particle resuspension by a turbulent airflow

5.1 Introduction 84
5.2 Adhesion models 85
5.3 Lennard-Jones intermolecular potential 87
5.3.1 Particle-surface interaction with deformation 87
5.3.2 Particle-surface interaction without deformation 88
5.3.3 Particle-particle interaction without deformation 90
5.4 Model for particle resuspension 91
5.4.1 Resuspension rate constant 91
5.4.2 Adhesive force distribution 92
5.5 Aerodynamic removal forces 94
5.5.1 Moments of aerodynamic forces 94
5.5.2 Mean and fluctuating components of the aerodynamic forces 96
5.6 Lennard-Jones parameters 97
5.7 Electrostatic forces 98
5.8 Monolayer resuspension 99
5.8.1 *Tabor* number 99
5.8.2 Reeks and Hall (2001) experiments 101
5.8.3 Ibrahim et al. (2003) experiments 106
5.8.4 The effect of electrostatic forces 109
5.9 Multilayer resuspension 112
5.9.1 Kinetics of a multilayer deposit 112
5.9.2 Analytical solutions of the differential equations 114
5.9.3 Characteristics of a two-layer deposit 116

5.9.4 Comparison of different kinetics 119
5.9.5 Resuspension from multiple layers 120
5.9.6 Fractional resuspension rate Λ(t) 122
5.9.6.1 Evolution of Λ(t) for a multilayer deposit 122
5.9.6.2 Influence of exposure time and the $1/t$ law 123
5.9.6.3 Influence of friction velocity 125
5.10 Conclusions 127

Chapter 6 Modeling of particle resuspension due to surface vibration

6.1 Introduction 129
6.2 Bending waves as force propagator 129
6.3 Condition for particle resuspension 131
6.4 Approximation of the force of oscillation 132
6.4.1 Approximation of the force of oscillation from an external force acting as a δ function in time and space 132
6.4.2 Approximation of the force of oscillation from an external force acting as a function periodic in time and as δ function in space 133
6.4.3 Approximation of the force of oscillation from an external force acting as a function periodic in time and Gaussian in space 134
6.5 Adhesive force distribution 135
6.6 Displacement of the plate 136
6.7 Force of oscillation 139
6.8 Particle resuspension 140
6.9 Conclusions 142

Chapter 7 Conclusions and recommendations for future work

7.1 General conclusions 144
7.1.1 Measurement campaigns 144
7.1.2 Modeling of particle infiltration and resuspension 145
7.2 Recommendations 146

References 147

Appendix A: Publications 162
A.1 Scientific Journals (Peer Reviewed) 162
A.2 Conferences 163

Chapter 1

Introduction to physical processes of particles in indoor environments

1.1 Introduction

Atmospheric pollution has played an important role on everyday life in modern societies. Atmospheric conditions have strong impact on environmental pollution. Urban areas are of great concern with the population in major cities still increasing. People can be exposed to harmful species such as particles, gases and chemical compounds. Airborne particles, chemical compounds and gases are usually the product of anthropogenic activities (fuel combustion, industrial processes, energy production), whilst natural air pollution can also contribute (forest fires, volcano eruptions) significantly (Austin, Brimblecombe and Sturges 2002). Although, the latter cannot be controlled or avoided, the impact from anthropogenic sources of pollution can be restricted. Therefore, international organizations such as EPA (Environmental Protection Agency) and WHO (World Health Organization) emerged by the need of protecting the environment and human health, by defining international standards or limits in emissions and concentrations of the pollutants into the ambient air.

However, it was only until recently realized that people spend the majority of their time indoors, thus are exposed to indoor contaminants. Investigation of air pollution, then became a subject of indoor conditions and as important as outdoor atmospheric pollution. Indoor air quality (IAQ) is the general term that refers to air quality within buildings and involves the characterization of indoor sources, investigation of hazardous contaminants and their impact to the ambient air. Adverse health effects are closely associated with air pollution through human exposure to indoor contaminants, as many studies have already shown (Pope and Dockery 2006; Franck et al. 2011; Sarigiannis et al. 2011; Morawska et al. 2013). They usually include cardiovascular disease, irritations, asthma, nausea, dizziness, central nervous system damage, cancer and even death. The human respiratory system operates as an entry for the ambient air. Eventually, the lungs are the recipients of the inhaled air. To this end, it is important to understand how people are exposed to airborne particles during everyday life where implications to their health may become substantial.

1.2 Particle fundamentals

1.2.1 Particle size and shape

Several terms are used to denote the suspended microscopic particles in the air, where the definitions usually indicate the physical form of the particles. The most common of them is *aerosol*, which is defined as a suspension of solid or liquid particles in a gas (Hinds 1999). The term includes both the particles and the suspended gas (which is usually air) and strongly states the two-phase system of the aerosol. Particulate matter is another widely used term that is equivalent to the definition of aerosol and refers to either liquid or solid particles.

Particles in the ambient air vary considerably in size and shape. Most of their properties depend on these parameters, thus knowledge of the variability of particle physical characteristics becomes substantial. Moreover, in many cases particle physical characteristics are directly linked with their origin or method of generation.

Particle size is the most important parameter that determines its properties and behavior. Physical principles of particles depend considerably on particle size such that particles of different sizes are governed by different laws. Particle size covers a wide range, from a few nanometers up to several micrometers. A very common classification of particles based on its size defines the *ultra-fine* particles (particles with diameter smaller than 0.1 μm), the *fine* particles (particles with diameter smaller than 2.5 μm) and the *coarse* particles (particles with diameter higher than 2.5 μm). Alternatively, the term *submicrometer* particles is widely used, referring to those particles with diameter smaller than 1 μm. Particle size is usually defined by its diameter but particle radius is very commonly used.

In general, particle shape is irregular with a very small fraction of airborne particles being spherical. Particles are usually found in many complex shapes varying from long, thin shapes such as fibers or high complexity particles such as agglomerates. Thus, an equivalent diameter is often used to represent the size of the particle. The *particle equivalent diameter* refers to a sphere having the same value of a specific physical property as the irregularly shaped particle under investigation (Kulkarni, Barron and Willeke 2011). The most common equivalent diameters that are used are the aerodynamic equivalent diameter, the mobility equivalent diameter, the mass equivalent diameter and the volume equivalent diameter. The *aerodynamic* equivalent diameter is the diameter of a standard-density sphere having the same gravitational settling velocity as the particle under investigation and is useful for big particles. The particle aerodynamic diameter for particles larger than 1 μm is given:

$$d_a = d_p \left(\frac{\rho_p}{\rho_0}\right)^{1/2} \quad (1.1)$$

where, d_a is the aerodynamic diameter, d_p is the physical particle diameter with particle density ρ_p and ρ_0 is the standard particle density (1000 Kg/m^3). If particle size is much smaller (ultrafine particles) then Brownian motion dominates and the *mobility* equivalent diameter is more appropriate to use. Alternatively, the *mass* equivalent diameter is the diameter of a nonporous sphere that has the same mass as the particle under investigation, whilst the *volume* equivalent diameter corresponds to a spherical particle of the same volume of the particle under investigation.

1.2.2 Chemical composition

The chemical composition of particles depends on the formation process, origin as well as environmental conditions. Physical or chemical processes may alter the chemical composition of the airborne particles such as condensation, evaporation, coagulation or chemical reactions. Particles may be composed by a variety of different chemical compounds both organics, inorganics and trace elements. Airborne particles that are comprised of the same chemical compound are called *homogenous*, whereas, if they are comprised by several chemical compounds they are called *heterogeneous*. Moreover, particles that are emitted directly to the air are called *primary* particles, whilst particles that are formed in the air by chemical reactions are called *secondary* particles (Hinds 1999).

Sulphate and nitrogen compounds are mainly of secondary origin formed in the air by precursors emitted by combustion processes (power generation, biomass burning, vehicular traffic, shipping). On the other hand, natural sources include soil emissions and wildfires (Calvo et al. 2013). Carbonaceous species are also major fraction of atmospheric particulate matter and can be classified into three groups: black carbon, elemental carbon and organic carbon. The main sources are fossil fuel combustion and biomass burning. These species play an essential role on global climate change and radiation. On the other hand, sources in the indoor environment that are associated with a variety of chemical compounds are cooking and smoking. Smoking is identified with emissions of more 4,000 species including both organic (alkanes, sterenes, sterols, aliphatic and cyclic acids, polycyclic aromatic hydrocarbons (PAHs) and organic carbon) and inorganic (ions, elemental carbon and trace elements) (Morawska and Salthammer 2003). In addition, cooking contributes considerably to the indoor air with PAHs, alkanes, fatty acids, aldehydes, organic ions, elemental carbon and inorganic compounds (elemental carbon, Na^+, K^+, Ca^{2+}, Cl^-) (Abdullahi et al. 2013).

1.2.3 Particle size distributions

A mixture of particles may be *monodisperse* or *polydisperse,* where the first term involves single-sized particles (particles that are all of the same size) whereas the second term refers to particles which are found in a variety of different sizes.

In practice, airborne particles are polydisperse with the size range vary considerably covering several orders of magnitude. Particle size and its distribution affects its physical and chemical properties. Therefore, it is necessary to obtain a mathematical description of the size distribution of the airborne particles. A variety of size distributions is used with the most common of them being the *number distribution*. Accordingly, the particle number concentration is plotted against particle diameter. In this way, the particle number concentration is given in discrete size intervals from d_p to $d_p + dd_p$, where d_p is the particle diameter. The number size distribution is:

$$dN = N(d_p)d\ln d_p \tag{1.2}$$

where, $\ln d_p$ was used because the particle diameter ranges over several orders of magnitude. Similarly, the *volume* and *mass* size distributions are frequently used:

$$dV = V(d_p)d\ln d_p \text{ , } dM = M(d_p)d\ln d_p \tag{1.3}$$

In addition to size distributions used to plot the number, volume or mass concentration data several functions are used to model these distributions. The lognormal distribution has been a common choice for particle size distributions. It is symmetrical and is characterized by a peak and a tail around the peak ,which represents the range of the variable, in this case the particle diameter. The lognormal distribution is given:

$$dN = \frac{N}{\sqrt{2\pi}\ln\sigma_g} exp\left[\frac{-(\ln d_p - \ln d_g)^2}{2(\ln\sigma_g)^2}\right] d\ln d_p \tag{1.4}$$

where, N is the total number of particles, d_g is the geometric mean diameter and σ_g is geometric standard deviation. The latter is the measure of the width of the distribution. Moreover, in the case of a lognormal distribution the surface and volume distributions are also lognormal and are given by Equation (1.4) by replacing N with the total surface or volume and by replacing d_g with the surface median (SMD) or volume (VMD) median diameters respectively. The median diameters are related:

$$SMD = d_g exp\left(2\ln^2 \sigma_g\right), VMD = d_g exp\left(3\ln^2 \sigma_g\right) \quad (1.5)$$

Figure 1.1 shows the relation between the number, surface and volume distribution of the same particle size distribution as a function of particle size.

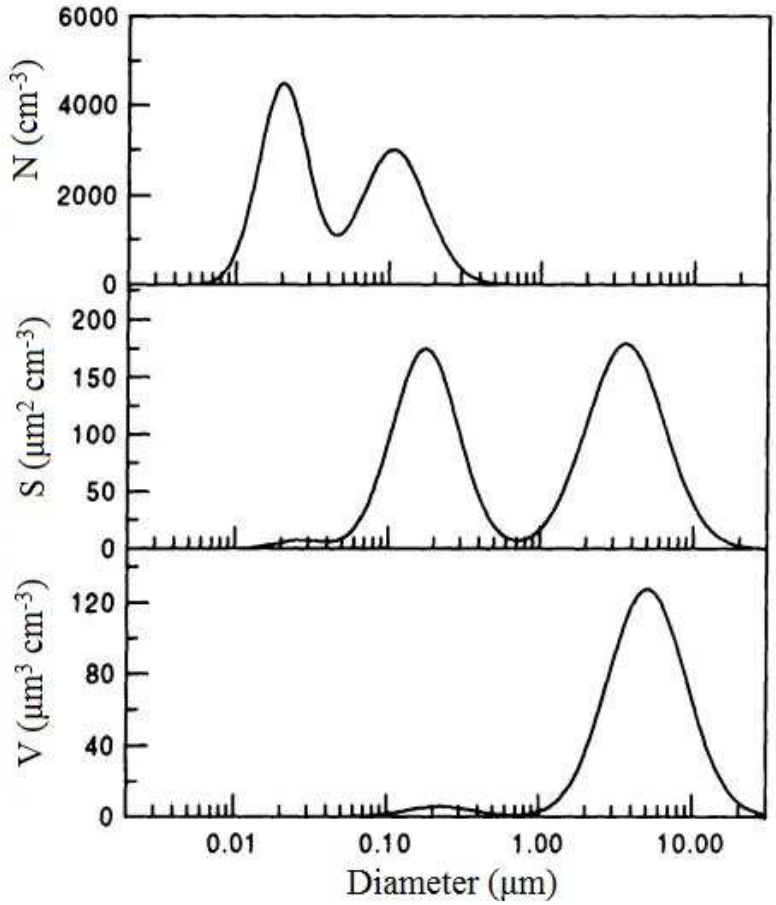

Figure 1.1: Particle number, surface and volume distribution of the same particle size distribution (adapted from Seinfeld and Pandis 2006).

Size distributions have very often more than one peak. This characteristic is associated with the presence of different sources contributing at different size ranges, where the distribution may be fitted by a sum of lognormal distributions. Moreover, other distributions have been applied successfully to particle size distributions such as the modified gamma distribution, the Weibull distribution and the Rosin-Rammler distribution (Hinds 1999; Kulkarni, Barron and Willeke 2011). These distributions apply to special situations and are usually used because of the skewed shape of most particle size distributions.

1.3 Fundamentals of physical processes of indoor particles

Particles can be classified based on their origin. Source-associated properties like chemical composition or particle size play a significant role on particle dynamics, which makes knowledge of the origin a significant factor. Fate of particles in the indoor environment depends on the dynamic behavior of the airborne particles. Once the particles are released or transported indoors, they are subject to interactions, physical processes and reactions that can alter their chemical composition, physical characteristics and concentration. The most significant physical processes indoors are penetration from outdoors, deposition on indoor surfaces, removal by ventilation, resuspension, coagulation and condensation/evaporation (Morawska and Salthammer 2003). Figure 1.2 presents a schematic of the most important processes that particles experience in the indoor environment.

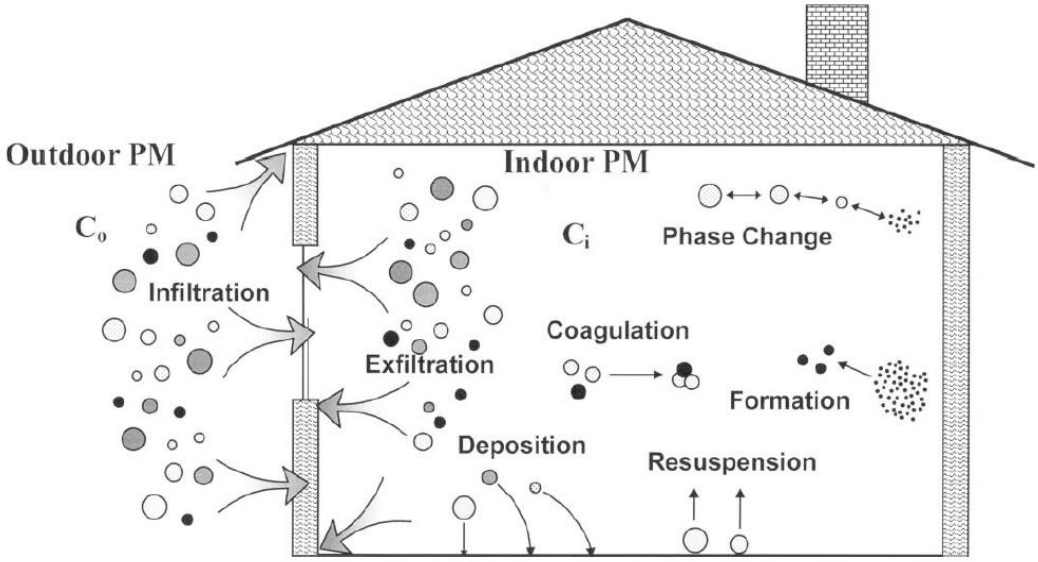

Figure 1.2: Schematic of the most important process that particles experience in the indoor environment (adapted from Thatcher et al. 2003).

Penetration of outdoor originated particles indoors can take place through open windows or doors as well as through leaks in the building envelope. The latter includes any cracks, gaps or holes in the building shell. The parameter that is used as a measure of particle penetration from outdoors is the *penetration factor* often called *penetration coefficient* or *penetration efficiency* (Long et al. 2001; Thornburg et al. 2001; Rim et al. 2010; Chen and Zhao 2011). The penetration efficiency denotes the fractional penetration of outdoor particles indoors, thus, it varies between zero and unity. A unity value for penetration efficiency states

that outdoor particles are easily transported indoor regardless of their properties. This case is usually associated with penetration from open windows or doors, where, airflows between the indoor and outdoor environment are relatively large. However, in the case of penetration through the building envelope, the situation is altered and particle penetration becomes size-dependent. The infiltrated particles enter the building through airflows within the leaks originally driven by temperature of pressure gradients (Liu and Nazaroff 2001; Lai et al. 2012). Particle size is then the dominant factor that governs penetration indoors. Small particles (ultrafine) are easily lost due to Brownian motion, whereas, penetration for large particles (coarse) is limited due to their size. Studies have shown that the most effective penetration lies in the size range between 0.1-1 μm (Abt et al. 2000; Long et al. 2001; Bennett and Koutrakis 2006; Chen and Zhao 2011), namely the *accumulation* size fraction.

Deposition on indoor surfaces involves all the available surfaces that act as a sink for indoor particles. Unlike gas molecules that rebound when they collide with surfaces, particles adhere on the surface (Hinds 1999). Particle deposition is governed by diffusion for small particles and by gravitational settling for larger particles. Besides particle size, deposition on indoor surfaces depends on the area of the surface and its characteristics such that higher surface area increases the possibility for deposition whilst wall texture plays a significant role (Abadie et al. 2001). Particle deposition is defined as the rate of deposition of particles onto a unit area of a surface at any time t and can be also expressed in terms of deposition velocity, i.e. the velocity that particles migrate to a surface (Hinds 1999). However, a useful term that can be found in literature involves the *deposition loss rate coefficient*, which is defined as the number of particles depositing on the total surface available per unit of time (Morawska and Salthammer 2003). While, the deposition velocity is determined by incorporating orientation of the surface (upward, downward or vertical) and depends strongly on the enclosure geometry (Lai and Nazaroff 2000), the deposition loss rate coefficient is easier obtained irrespectively of indoor geometries, thus has a wider application in experimental studies (Thatcher and Layton 1995; Long et al. 2001; Vette et al. 2001; Wallace et al. 2004; Rim et al 2010).

Removal of indoor particles by ventilation includes either natural or mechanical ventilation. The term *exfiltration* occasionally is used to refer to removal by ventilation. In the first case, indoor particles are removed by airflows that carries the particles to the outdoor environment and relies on wind pressure or weather conditions (Chu et al. 2015). On the other hand, mechanical ventilation requires a well-design mechanical ventilation system where the indoor air is driven towards the outdoor environment by using fans. In this case, the airflows are forced by pressure differences where the exchange (or ventilation) rate

of the under study volume is controlled and can be modified according to indoor conditions (Liddament 2000).

Particle resuspension is defined as the detachment of a particle from a surface and its re-suspension to the ambient air. The term denotes that the particle was previously airborne but under specific circumstances re-entrain into the air. These circumstances usually involve the act of a force on the particle that may cause particle detachment from the surface. The forces can be mechanical, aerodynamic or even electrostatic. When a particle lies on a surface, it is subject of adhesion phenomena. Adhesion phenomena arise from intermolecular interactions between two bodies (molecules, particles) and in principle originate from purely physical interactions (Israelachvili 1992). The most important factor for particle resuspension is particle size. While adhesive forces increase linearly with particle diameter, removal forces are size-dependent but with a factor higher than unity. Gravitational, centrifugal and vibrational forces have cubic dependency with particle size, whilst air currents are quadratic dependent with particle size (Hinds 1999). These relationships suggest that as particle size increases the removal force the particle experiences due to its size, increases substantially compared to the increase in the adhesive forces. Therefore, resuspension of bigger particles is easier attainable compared to smaller particles. Several studies have shown that particles with diameter > 2.5 μm are easier resuspended compared to submicron particles (Ferro et al. 2004; Corsi et al. 2008; Rosati et al. 2008; Shaughnessy and Vu 2012).

Coagulation is a process that alters both the particle number size distribution and the number concentration. Accordingly, particles that are subject to Brownian motion collide with each other and form bigger particles. As a result, particle number concentration decreases with time while particle size increases. Coagulation has strong impact on particle number size distribution with the range of particle sizes present playing an important role on the total process. On the contrary, particle mass concentration is not affected at all since the total mass of the particles is preserved. Coagulation is governed by the rate of diffusion of particles towards each other, thus a net movement is caused from a higher concentration to a lower one (Hinds 1999). Studies have shown that coagulation is important for high particle number concentration but can become negligible after a lower threshold is reached (Xu et al. 1994; Hussein et al. 2009).

Condensation is the physical process where particles grow in size by condensation of vapors on their surface. The reverse process, where particles are shrinked in size, refers to evaporation. Both processes involve mass transfer from the bulk phase to or from the particulate phase. The vapor phase can be a mixture of volatile organic compounds (VOCs) and water, where differences between temperature on the surface of the particles and the surrounding causes condensation or evaporation (Saleh and Shihadeh

2007). The driving term arises from a gradient of vapor concentration between the particles and the bulk (Broday and Georgopoulos 2001). Accordingly, a particle exhibits condensation when vapor is condensed on its surface. This process requires the presence of a supersaturated vapor around the particle, which grows in size. On the other hand, the particle experiences evaporation when liquid evaporates from its surface, which in turn results in the reduction of its size. Both processes have great impact on particle mass concentration, whereas number concentration is not affected.

1.4 Material balance model for indoor particle concentration

Fate of indoor particles and their dynamics can be investigated through material balance models. In principle, these models assume that the total mass is conserved. A general mass balance model includes all terms that are associated with particles sources, sinks, transport and transformation in a spatial domain. These models are widely used for IAQ purposes, where inputs, variables and parameters can vary according to the case under study. A mass balance model is usually expressed by changes in indoor particle concentration (either number or mass).

A common assumption in order to apply a material balance model has been the uniform spatial distribution of indoor particle concentration in the under study volume V. Then, the governing equation for the time rate of changes of indoor particle concentration in compartment i and for a selected size range (d_p) will read:

$$\frac{d(C_{in}V)}{dt} = aPVC_{out} - kVC_{in} - aVC_{in} + J_{exch} + J_{coag} + J_{cond} + \dot{S} + \dot{R} \quad (1.6)$$

where, C_{in} is the indoor particle concentration (μg/m^{-3}), C_{out} is the outdoor particle concentration (μg/m^{-3}), a is the air exchange rate with the outdoor environment (h^{-1}), P is the penetration efficiency, k is the deposition loss rate coefficient (h^{-1}), J_{exch} is the exchange rate of particles between compartment i and other interior areas (μg/h^{-1}, for multi-zone environments), J_{coag} is the coagulation rate (μg/h^{-1}), J_{cond} is the condensation (evaporation) rate (μg/h^{-1}), $\dot{S}$ is the emission rate of particles originating from indoor sources (μg/h^{-1}) and $\dot{R}$ is the resuspension rate of indoor particles (μg/h^{-1}).

The above equation can be simplified assuming negligible coagulation and condensation rate. Furthermore, in the absence a multi-zone environment the exchange rate with other interior areas can be

neglected and the general mass balance model for the under study volume and the selected size range is rewritten as:

$$\frac{dC_{in}}{dt} = aPC_{out} - kC_{in} - aC_{in} + \frac{\dot{S}}{V} + \frac{\dot{R}}{V} \quad (1.7)$$

where, the sources in this case include particle generation from indoor sources, resuspension of the deposited particles and infiltration of outdoor originated particles. On the other hand, sinks include exfiltration of indoor particles to the outdoor environment and losses due to deposition on indoor surfaces.

1.5 Objective of the present thesis

In the context of HEXACOMM (*Human Exposure to Aerosol Contaminants in Modern Microenvironments)* and within IAQ purposes, the present thesis examined particle characteristics in modern workplaces accompanied with modeling of the most significant physical processes. With focus on particle infiltration from outdoors and resuspension of indoor particles, the aim was to investigate the physical characteristics that govern both processes and lead to airborne particles indoors.

The main objective of the in-field campaigns was to measure particle concentrations both indoors and outdoors and evaluate the impact of indoor sources as well as the contribution of the outdoor environment. Accordingly, in Chapter 2 human-originated indoor sources where identified in modern offices equipped with mechanical ventilation system whilst the impact of the outdoor environment to indoor concentration levels was investigated. Subsequently, in Chapter 3 size-dependent particle dynamics were examined in order to evaluate infiltration characteristics from the outdoor environment in the case of natural penetration. The resuspension rate arising from human walking was obtained in Chapter 4 using a deterministic indoor model. In further investigation of the process, modeling of the physical situation of particle resuspension was achieved using both stochastic and deterministic approaches. In Chapter 5 a stochastic description of particle interactions and external excitations was employed for resuspension due to the act of a turbulent airflow upon the particles, whereas in Chapter 6 a mechanistically principle was incorporated for particle motion and eventually entrainment to the ambient air when the external force acts normal on the surface at a distance from the particle.

1.6 Contribution and novelty of the present thesis

The present thesis examined the indoor/outdoor sources in mechanically ventilated buildings corresponding to modern working environments. Particle mass and number concentrations were measured simultaneously both indoors and outdoors, which, gives the advantage of investigating particle characteristics both in terms of number and mass concentrations at the same location and provided the impact from the outdoor environment. Thus, it advances the understanding for particle size characteristics and sources in modern buildings with properly designed ventilation system.

Particle infiltration from outdoors was investigated in a naturally ventilated building (library) which provided an appropriate site for investigation of infiltration characteristics due to limited presence of people. Size resolved analysis was used to examine particle penetration from outdoors and the relevant physical processes that govern particle infiltration.

The resuspension rate of indoor particles, induced by human walking, was obtained using a determinist model that uses a set of mass balance equations. Particle resuspension was evaluated under different dust loadings and walking patterns to examine the effect of each parameter to the resuspension rate.

Particle resuspension due to the act of a turbulent airflow was investigated with focus on intermolecular interactions for a monolayer deposit. The role of particle size and the relative surface roughness was investigated using a kinetic approach for estimating particle resuspension, whilst the impact of the electric particle charge was also examined. Moreover, particle resuspension was investigated for multilayer deposits where the kinetics and the single-layer resuspension rate were examined in conjunction with the impact from the exposure time and friction velocity induced by the airflow.

Finally, particle resuspension was examined adopting an alternative approach, which includes mechanical resuspension due to an external vibrating force acting normal on the surface. The impact of momentum transfer through the surface on the particle was investigated along with the role of material properties, surface roughness and particle size.

In summary, the novelty of the present thesis encloses the investigation of modern workplace environments in respect to indoor particle concentrations (both mass and number), the characteristics of particle infiltration by physical penetration through the building shell, the impact of dust loading on the floor in the resuspension rate of indoor particles, the physical situation under which particles resuspend in the case of a turbulent airflow acting upon them or in the case of an external vibrating force, with focus on the influence from particle size and surface roughness.

Chapter 2

Characteristics of particle mass/number concentrations in modern offices

2.1 Introduction

Indoor air quality (IAQ) in office environments has great effect on human comfort and work performance. Thus, it is under investigation since indoor pollutants essentially influence IAQ with human occupational health being on the focus for improving environmental conditions.

Pollutants may originate from indoor sources as the product of human occupation, where, chemical composition and characteristics of indoor pollutants are directly linked with primary sources. IAQ in office environments is highly affected by the use of office equipment, most notably by hardcopy devices and printers (Wensing et al. 2008; Salthammer et al. 2012). Nonetheless, human occupation itself can cause particle emissions with resuspension activities being a very common indoor source (Ferro et al. 2004).

In addition, IAQ in workplaces depends considerably on mechanical ventilation. Ventilation of the building is important and has strong impact on concentration levels indoors (Quang et al. 2013; Park et al. 2014). Ventilation of modern buildings is performed by advanced mechanical ventilation systems where airflows at different compartments and the exchange rate are designed in order to achieve high quality standards**.** Therefore, modern ventilation systems prevent a considerable fraction of outdoor particles to enter the building by using filters of high-selectivity, thus provide the indoor environment with clean air.

The focus of this chapter is to investigate particle concentration characteristics in modern offices. Two measurement campaigns were performed, one in Kjeller, Norway and one in Chania, Greece. Both buildings are located in a rural/suburban location with limited vehicular traffic. Moreover, both buildings are equipped with mechanical ventilation system but different occupation scheme applies in each case. The main objectives are to examine the contribution of the outdoor environment indoors, as well as the influence of human occupation in the indoor environment for each under study case. Indoor sources were investigated in respect to origin and particle size, whilst, infiltration from outdoors was evaluated accounting building characteristics for each case.

2.2 Measurement of particle concentrations in offices in Norway

2.2.1 Location/office description

The offices belong a building located in a rural/suburban area 17 km northeast of the city of Oslo, Norway. It belongs to Norwegian Institute for Air Research and it is part of a science park surrounded by a residential area consisting of urban area and forest with several streets of medium traffic. A map of the location of the building is shown in Figure 2.1. Besides few busses that run through the area and domestic activities there are no other major sources in the vicinity of the area where the building is located.

The building has one main entrance at the front and a second one at the right hand side used for storage purposes. It is a three floor building, mainly consisting of offices and is separated into two sections connected through an inside bridge. The frame of the building is constructed by bricks with a few areas covered by glass (mainly windows and doors). All offices are connected to outdoors with windows. The building is mechanically ventilated, although the windows in the offices can be opened at any time by the occupants. Smoking and burning candles is prohibited inside the building in all areas.

Figure 2.1: Map of the location of the building under study and the surrounding area.

A few open areas cover the indoor space mainly belonging to the entrance hall and the laboratories. The laboratories are a mix of open space and small offices connected through corridors. Two offices were selected to perform the measurement, one at the first floor and one at the second floor. The office on the first floor is located inside a laboratory at the right section of the building, whereas, the office at the second floor is connected through a corridor with other offices located at the left section of the building. Figures 2.2 and 2.3 provide the floor plan and the location for each office. Office A corresponds to the office at the second floor and office B corresponds to the office at the first floor. Office A faces the front of the building and is very close to the main entrance, whereas, office B faces the backside of the building. Several windows connect the two offices both with other indoor places and with outdoors. Figure 2.4 presents a detailed scheme of the two offices.

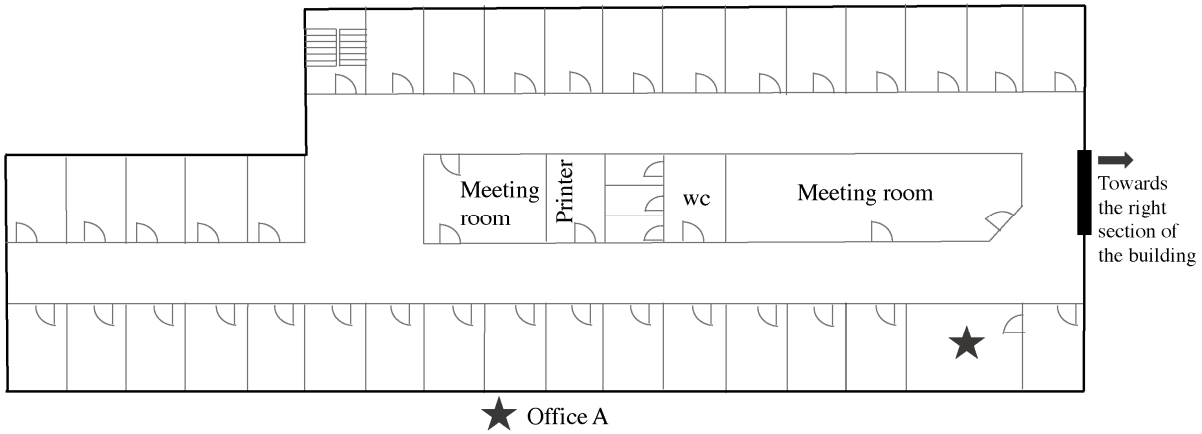

Figure 2.2: Floor plan of the left section of the building. Location of office A.

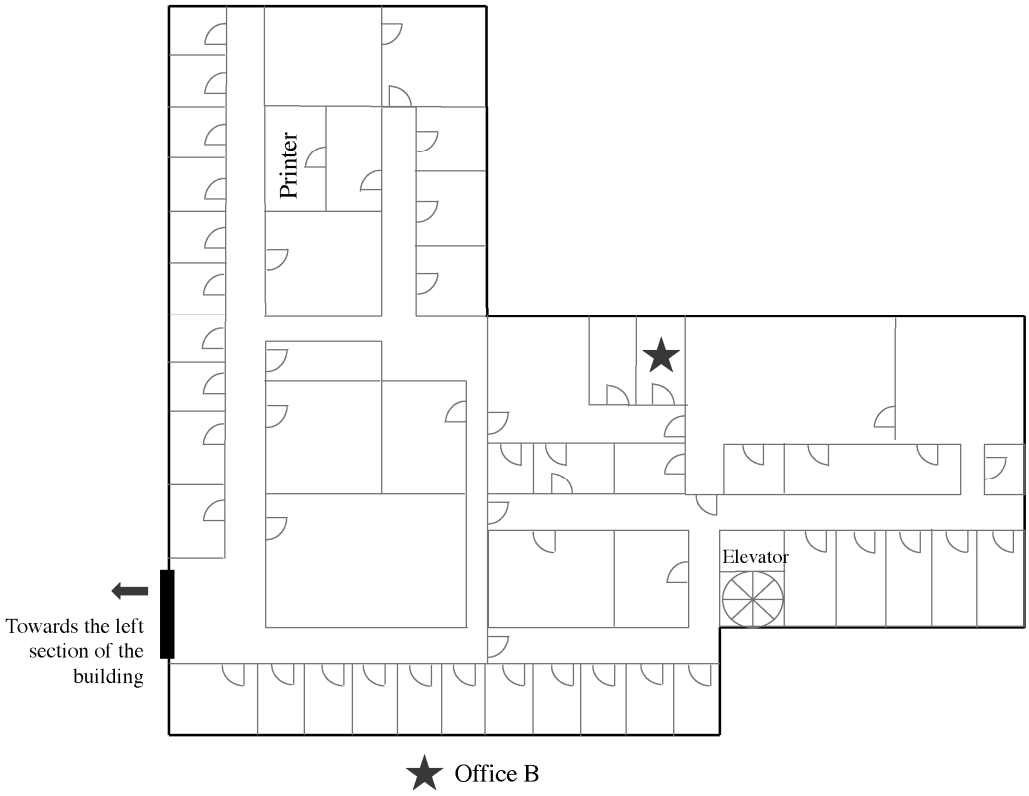

Figure 2.3: Floor plan of the right section of the building. Location of office B.

Office A was furnished with shelves covered by books and papers, a desk with a computer and chairs. Blinds covered the windows at all times both the ones facing indoors and outdoors. The area of office A was 21 m^2 and its volume was 56 m^3. Office B on the other hand, was furnished with a long desk, one chair

and shelves mostly covered with laboratory equipment. No blinds covered the windows. The area of office B was 16 m^2 and its volume was 40 m^3. Office A was connected to the main corridor of the section through a small office of the same width but smaller length, whereas, office B was directly connected to the laboratory through the door. The floor in both offices was covered with linoleum.

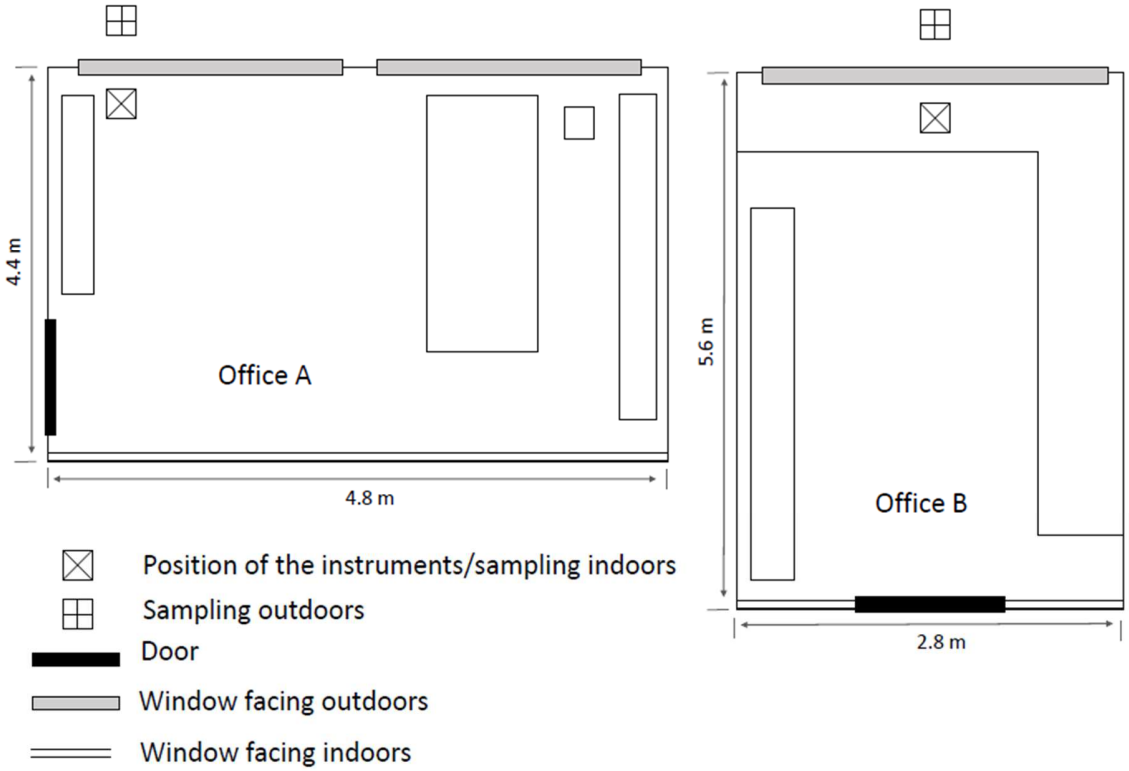

Figure 2.4: Scheme of office A and B, and position of the instruments.

2.2.2 Experimental set up

Particle size distribution was measured with a TSI 3936 Scanning Mobility Particle Sizer (SMPS) and a TSI 3321 Aerodynamic Particle Sizer (APS). SMPS consisted of a TSI 3775 Condensation Particle Counter (CPC), a TSI 3080 Electrostatic Classifier (EC), a TSI 3081 Differential Mobility Analyzer (DMA) using a Neutralizer Nickel-63 as a radioactive source. The SMPS measured particle number size distribution in the size range 14.6 – 685.4 nm in 107 channels and operated with sample flow rate at 0.3 L/min. The APS measured particle number size distribution of particles with aerodynamic diameter in the size range 0.5 – 18.4 µm in 51 channels with sample flow rate 1 L/min. Both SMPS and APS were set to log the data every 5 min.

Additionally, PM_{10} mass concentration was measured with a TSI 8530 Dust - Trak II using flow rate at 1 L/min. The log interval was set to 1 min but 5 min average mass concentration was used in all calculations. All instruments sampled from both indoors and outdoors using a system of tubes for outlets along with a switching valve, attached to the instruments. Two identical tubes of 1 inch diameter were connected with the valve in a straight line (one from the left and one from the right of the valve for sampling indoors and outdoors respectively) at 10 – 20 cm above the instruments. The frame of the window was replaced with a wooden one of exactly the same size. Outdoor sampling was succeeded by connecting the tube with the outdoor environment through a hole on the wooden frame. All gaps were sealed properly both from inside and outside the window. The switching of the valve was controlled by a computer connected with the instruments and an interval of 10 min was selected for sampling indoors/outdoors. The SMPS was scanning 150 s upward and 60 s downward every 5 min, whereas, the APS was scanning 150 s every 5 min. One minute and 30 seconds delay was used in order to separate the samples and flush the tubing after switching of the valve. Hence, a 10 min sampling from indoors with log interval 5 min was followed by a 10 min sampling from outdoors with the same log interval.

2.2.3 Office occupation

The campaign was performed during June 2014, between 02-10/06/2014 in office A and between 10-13/06/2014 in office B. Office A was usually occupied during the working hours (08:00 – 16:00), whereas, no person was using office B. The latter was vacant during the measurements, thus, the indoor concentration was not affected by any indoor source induced by the human presence. On the other hand, the occupants in office A used a diary in order to record all human activities. No printers or any other kind of office equipment that could generate particles were present in the two offices.

Table 2.1 presents the occupied hours during the working days in office A. At non-working days, the office was unoccupied at all times. It indicates that office A was usually occupied between 8 am to 4 pm with maximum 3 people present inside the office during the campaign. Moreover, for small periods (10 - 20 min) during the working hours the office was vacant. All activities, presence of people and opening of the door were recorded in a diary. No special activity was recorded, thus, the number of persons inside the office involves only the physical presence of the people.

One person was using office A permanently, while, several people visited occasionally the office during the working hours. The windows, both those facing indoors and outdoors, were closed at all times. However, the entrance door was selectively closed or open by the occupants. Since, no equipment was present inside office A, indoor sources include any kind of human activities that can be related with particle emissions or

transport from another area of the building. According to Table 2.1, in the period 02-10/06/2014 during two of the typical working days (Monday-Friday) the office was vacant (03/06/2014 and 09/06/2014). Hence, the days when office A was occupied was on 02/06/2014 and on 04-06/06/2014 during the working hours.

Office B, on the other hand, was vacant during the whole measurement period with the door always closed. However, one of the windows facing outdoors was slightly open for one hour on 12/06/2014. Besides that, all other windows (both those facing indoors and outdoors) were closed during the measurements.

Table 2.1: Occupied hours and number of persons in office A. Indication for number of persons corresponds to the range of people that were present in the office during the working hours.

Date	Day	Occupied hours	Number of persons
02/06/2014	Monday	begin of sampling - 16:00	1 - 3
03/06/2014	Tuesday	-	0
04/06/2014	Wednesday	08:15 - 14:00	0 - 3
05/06/2014	Thursday	06:45 - 16:30	0 - 2
06/06/2014	Friday	08:00 – 14:00	0 - 2
07/06/2014	Saturday	-	0
08/06/2014	Sunday	-	0
09/06/2014	Monday	public holiday	0
10/06/2014	Tuesday	08:00 – end of sampling	1

2.2.4 Ventilation/Filters

The building uses a central ventilation system with different sub-systems serving at different parts of the building. The ventilation system is accompanied with heat exchangers and uses of district heating and cooling. The mechanical supply distributes the outdoor air from the ceiling. Glass fiber media filters are used, designed at airflow of 3400 m^3/h. The filters consist of several pockets where the air is distributed over the entire filter surface to achieve efficient removal of particles from the ventilation air. Particle efficiency of the filter meets requirements according to the European standard EN779:2002 for IAQ (Indoor Air Quality), where, the filters are classified based on the overall filtration (or collection) efficiency of liquid DEHS (Di-Ethyl-Hexyl-Sebacat) particles of 0.4 µm diameter. The filters used in the building have the overall filtration efficiency > 80 % and are replaced once per year. During the campaign, the filters were approximately 6 months old.

Low-pressure drop filters are used before the technical installations in the building, whereas, higher-pressure drop filters are used before the redistribution of the air into the building areas. The mechanical ventilation of the building was on during 05:00 – 18:00 on Mondays and 06:00 – 18:00 on Tuesdays – Fridays, while, the ventilation was off during weekends.

2.2.5 Indoor and outdoor particle concentrations

2.2.5.1 Particle number concentrations

Average values of the indoor and outdoor number concentration in the two offices are listed in Table 2.2a. The values represent the 24-hour average concentration of each calendar day for offices A and B. Number concentration of particles was evaluated for particles between 0.014 - 0.5 μm (SMPS) and 0.5 - 18 μm (APS). The separation was based on the particle size range that each instrument measured and also considering that the SMPS measures the particle mobility diameter, whereas, the APS measures the aerodynamic diameter of particles.

In general, average indoor number concentration was higher in office A compared to office B. The daily average indoor concentration in office A ranged between 290 - 601 cm^{-3}, whereas, in office B the indoor concentration ranged between 115 - 392 cm^{-3} for particles between 0.014 - 0.5 μm. Accordingly, bigger particles (0.5 - 18 μm) showed higher concentration in office A than in office B. Daily average number concentration in office A ranged between 0.09 – 0.16 cm^{-3} during working days (02/06/2014, 04-06/06/2014), while, average indoor concentration for non-working days was significantly lower (0.03 – 0.08 cm^{-3}). Office B preserved lower indoor concentration with maximum daily average concentration at 0.05 cm^{-3}. The increased indoor concentration in office A is associated with the presence of people during the working hours and highlights the impact of indoor sources.

Additionally, a comparison between working and non-working days for office A is presented in Table 2.2b. A general remark is that the indoor number concentration during working days was higher than the non-working days, with an increase of 24 % for lower (0.014 - 0.5 μm) and 140 % for higher (0.5 - 18 μm) particle sizes respectively. However, in order to isolate the impact from the presence of people a comparison between occupied and non-occupied hours was introduced. The separation to occupied and non-occupied hours was achieved using the data from periods when office A was occupied or not (no person present inside the office) according to the diary. All occupied hours represent working hours. The average indoor number concentration for particles in the size range 0.014 - 0.5 μm, during occupied hours in office A, was 769 cm^{-3}, whereas, during non-occupied hours was 333 cm^{-3} corresponding to an increase factor of 1.3. Bigger particles (0.5 - 18 μm) were also substantially increased by a factor of 3.8 during occupied hours.

Quang et al. (2013) also found higher particle number concentration during working hours. Higher increased concentration measured for bigger particles during the occupied hours compared to smaller particles suggests that human presence is stronger for higher particle sizes (> 0.5 µm) in the under study office.

Table 2.2: a) Daily average indoor and outdoor number (0.014 - 0.5 µm, 0.5 - 18 µm) and mass concentration (PM_{10}) in offices A and B, and b) average indoor number and mass concentration during working and non-working days and hours in office A.

a)		Office A					
		0.014 - 0.5 µm (cm^{-3})		0.5 - 18 µm (cm^{-3})		PM_{10} ($\mu g/m^3$)	
Date		indoor	outdoor	indoor	outdoor	indoor	outdoor
02/06/2014	Monday	305	3,287	0.14	2.47	1.8	18.0
03/06/2014	Tuesday	325	4,488	0.08	1.82	1.0	12.1
04/06/2014	Wednesday	598	3,503	0.16	1.34	2.1	14.1
05/06/2014	Thursday	356	4,223	0.11	2.37	3.0	21.4
06/06/2014	Friday	290	2,806	0.09	1.97	2.9	14.9
07/06/2014	Saturday	337	5,137	0.03	1.25	2.9	15.8
08/06/2014	Sunday	331	3,946	0.04	1.35	3.2	16.8
09/06/2014	Monday	389	5,284	0.05	1.97	3.5	17.4
10/06/2014	Tuesday	601	6,560	0.08	1.69	3.5	13.7
		Office B					
		0.014 - 0.5 µm (cm^{-3})		0.5 - 18 µm (cm^{-3})		PM_{10} ($\mu g/m^3$)	
Date		indoor	outdoor	indoor	outdoor	indoor	outdoor
10/06/2014	Tuesday	276	3,624	0.026	1.07	1.0	11.2
11/06/2014	Wednesday	392	4,784	0.050	2.72	1.5	18.3
12/06/2014	Thursday	158	5,252	0.008	0.69	-*	3.1
13/06/2014	Friday	115	3,782	0.002	0.24	-*	1.9

b)	Working days	Non-working days	Occupied hours	Non-occupied hours
0.014 - 0.5 µm (cm^{-3})	430	346	769	333
0.5 - 18 µm (cm^{-3})	0.12	0.05	0.29	0.06
PM_{10} ($\mu g/m^3$)	2.7	2.7	3.4	2.6

***** values were excluded from the dataset. Instrument reached detection limit.

Moreover, Figures 2.5 and 2.6 compare the indoor with the outdoor particle number concentration in the two offices. In both cases, the indoor concentration was always lower than the outdoor. Outdoor number concentration of particles at 0.014 - 0.5 μm was usually one to two orders of magnitude higher with average number concentration outside office A 4,268 ± 2,419 cm^{-3} and outside office B 4,613 ± 2,514 cm^{-3}. On the other hand, average indoor number concentration for the same particle size range in office A and B was 383 ± 350 cm^{-3} and 253 ± 152 cm^{-3} respectively. The same characteristic is observed also for bigger particles (0.5 - 18 μm). The values suggest that indoor number concentration is significantly lower than the outdoor. This finding is in agreement with other studies were the indoor concentration of ultrafine particles is considerably lower than outdoor concentration in commercial buildings where smoking is prohibited (Fisk et al. 2000; Matson 2005; Quang et al. 2013; Park et al. 2014). Mechanical ventilation of the building prevents a considerable fraction of outdoor particles to be transported indoors and filters the indoor particle concentrations as well. Together with the building envelope, which operates as a natural particle filter, indoor levels of both fine and coarse particles are considerably reduced inside the two offices in respect to outdoor particle concentration.

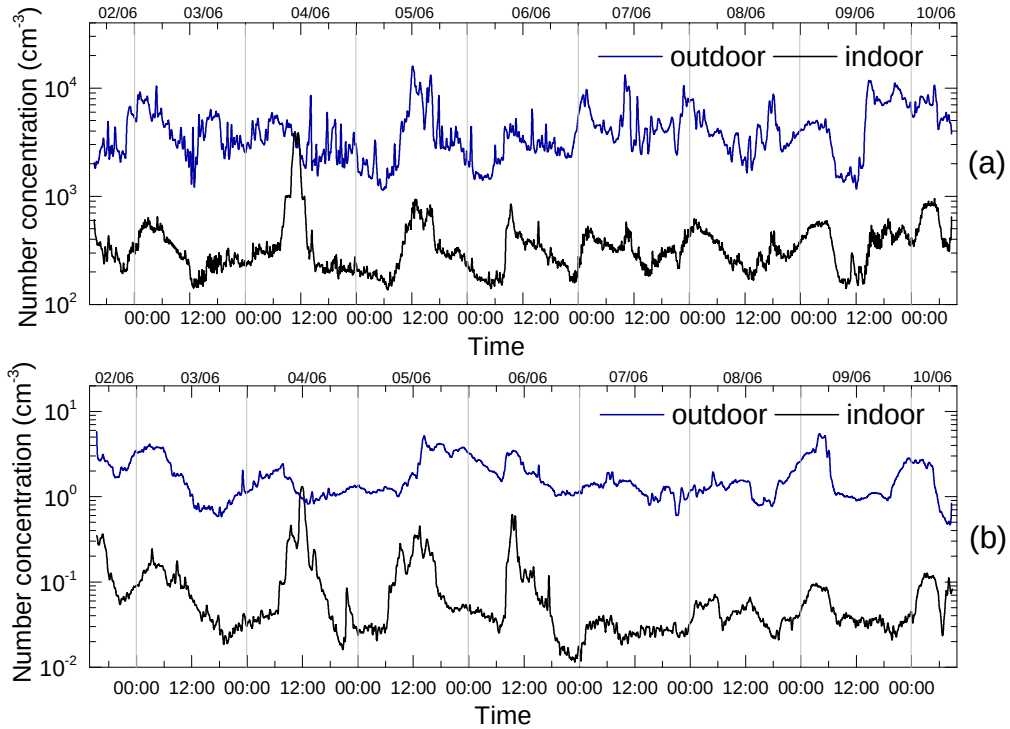

Figure 2.5: Indoor and outdoor particle number concentration at office A (02-10/06/2014) for particles between: a) 0.014 - 0.5 μm and b) 0.5 - 18 μm.

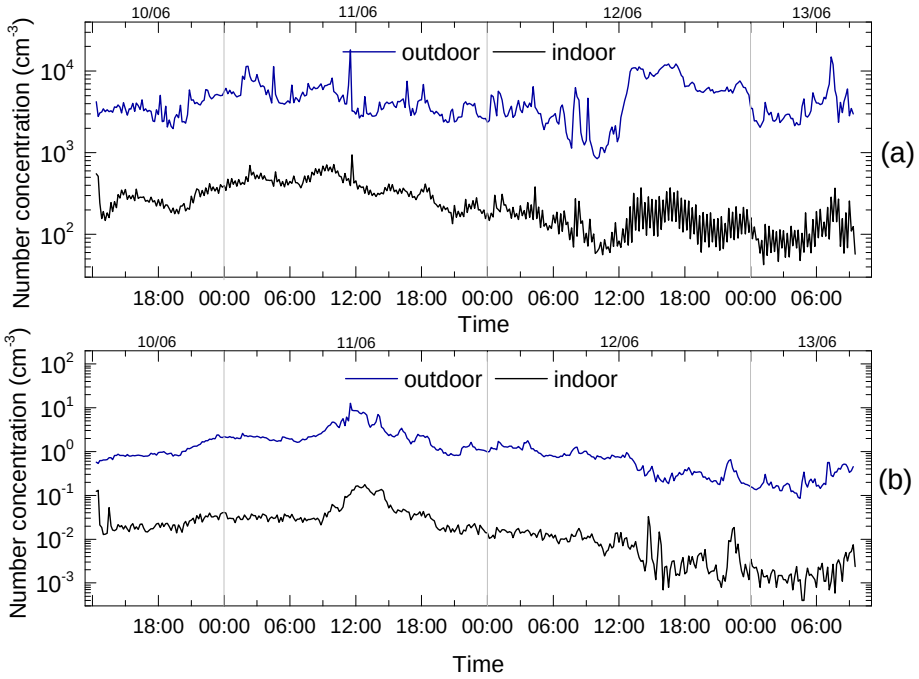

Figure 2.6: Indoor and outdoor particle number concentration at office B (10-13/06/2014) for particles between: a) 0.014 - 0.5 µm and b) 0.5 - 18 µm.

In addition, Table 2.2 indicates that indoor number concentration for particles in the size range 0.014 - 0.5 µm inside both offices is elevated when outdoor concentration was increased as well. Thus, on 03/06/2014 where office A was vacant it is observed that the daily average indoor concentration is higher (325 cm^{-3}) than the previous day (working day). Similar finding is observed for Saturday, Sunday and Monday (07 - 09/06/2014), where the office was unoccupied at all times and the average daily concentration in each day was higher than on 06/06/2014 Friday (290 cm^{-3}) which corresponds to a working day. The same characteristic was not observed for bigger particles (0.5 - 18 µm), where, the values during working days were increased irrespectively of the outdoor particle characteristics.

2.2.5.2 Particle mass concentrations

In general, considerable low levels of indoor mass concentration were observed in the two offices. The highest PM_{10} mass concentration was measured at 5.3 $\mu g/m^3$ in office A, while in office B it was at 3.0 $\mu g/m^3$. The numbers suggest slightly higher mass concentration in office A, probably due to human occupation, with no significant other indoor source. Moreover, the low indoor mass concentration, measured in both offices, is associated with the successful removal of outdoor PM_{10} by the filters while entering the building. Park et al. (2014) has found that mechanically ventilated buildings can reduce

exposure to outdoor particles up to 50%. Figure 2.7 indicates that the outdoor PM_{10} concentration measured in the range between 3 – 41.4 µg/m^3 for office A, while for office B the concentration ranged between 1 - 42.6 µg/m^3. These values indicate substantially higher outdoor mass concentration than indoors and the efficient removal of a major fraction of outdoor PM_{10}. The daily average values of outdoor PM_{10} for both offices are reported in Table 2.2a. Higher outdoor PM concentration outside office environments, in the absence of any significant indoor source is reported in Sangiorgi et al. (2013) and Quang et al. (2013). Finally, the comparable outdoor concentration confirms the influence of human occupation in office A, where higher PM_{10} concentration was observed.

No difference between working and non-working days was observed in office A (Table 2.2b) when comparing daily averaged concentrations, but this is due to effect of the averaged value used in the table. Therefore, average PM_{10} mass concentration was 2.7 µg/m^3 in both cases. Moreover, it is seen in Table 2.2a that the daily average indoor mass concentration is at similar levels for working (02/06/2014, 04-06/06/2014) and non-working days (03/06/2014, 07-09/06/2014). However, the impact of indoor sources is highlighted when comparing occupied and non-occupied hours (Table 2.2b). The latter had average indoor PM_{10} concentration 2.6 µg/m^3, while, the average indoor mass concentration during occupied hours was 3.4 µg/m^3 suggesting an increase of 31 %. Higher indoor concentration of $PM_{2.5}$ during working hours in mechanically ventilated buildings is also reported in literature (Liddament 2000; Quang et al. 2013).

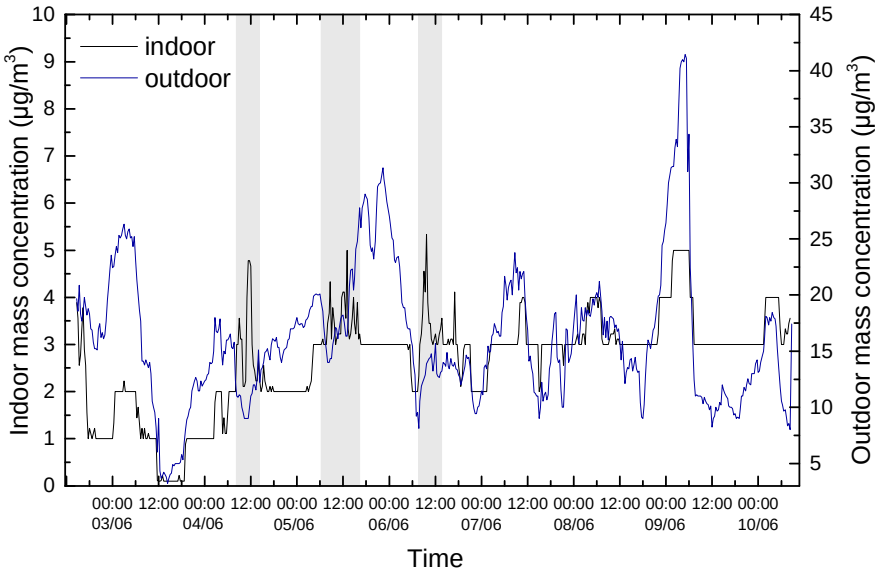

Figure 2.7: Indoor and outdoor PM_{10} mass concentration in office A (02-10/06/2014). Colored areas represent occupied hours.

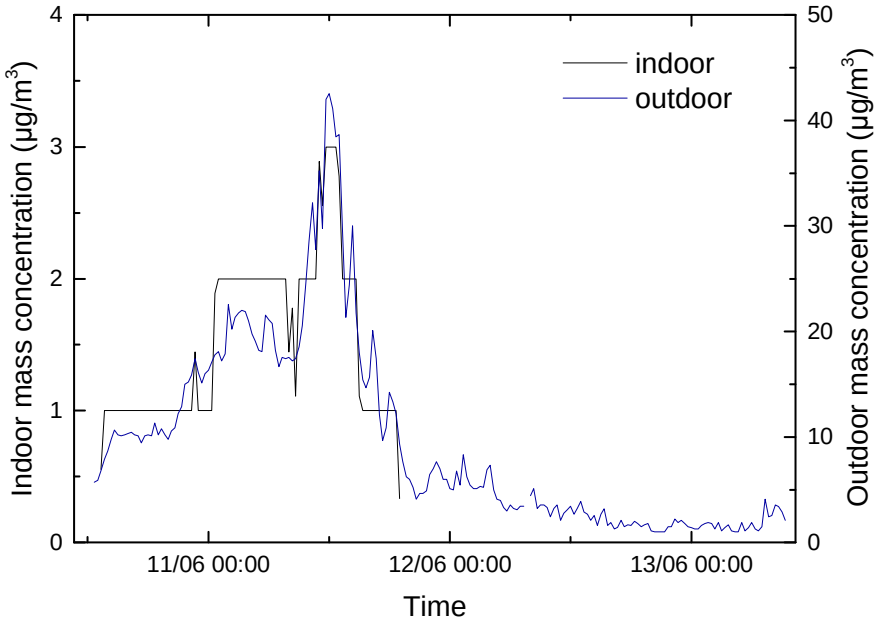

Figure 2.8: Indoor and outdoor PM_{10} mass concentration in office B (10-13/06/14). Indoor data after 6 pm on 11/06/2014 reached very low concentrations close to the detection limit of the instrument and were excluded from the dataset.

2.2.6 Influence of indoor/outdoor sources

Indoor concentration in the two offices was affected by both indoor and outdoor sources. Particle number concentration as well as PM_{10} concentration showed considerable temporal fluctuations during day and night. Since, no source that could generate new particles to indoor air was present inside office A, indoor sources in this case include any kind of human activities during working hours, with most important being the resuspension of indoor particles (Ferro et al. 2004; Rosati et al. 2008; Oberoi et al. 2010).

Figures 2.5-2.8 indicate a strong influence by the outdoor particulate matter indoors both in terms of number and mass concentration, when no major indoor source was present. Numerous studies have already highlighted the contribution from outdoor sources to indoor number and mass concentration (Abt et al. 2000; Ferro et al. 2004; Matson 2005; Cao et al. 2006; McAuley et al. 2010; Quang et al. 2013; Sangiorgi et al. 2013). In general, indoor particles both for number and for mass concentration data presented temporal fluctuations similar to the ones observed outdoors. Although, all windows with access to the outdoor air were closed (except one hour on 12/06/14 in office B) during the measurement, Figures 2.5-2.8 imply that there is an important penetration of outdoor particles inside both offices.

2.2.6.1 Office A

In total, office A was occupied for 4 days during the measurement campaign (02/06/2014, 04-06/06/2014). To determine the impact of human activities during the working days, Figure 2.9 presents a comparison between working and non-working days of indoor concentration for different size intervals. Local maxima that correspond to increased indoor concentration are observed mainly in the period 04 – 06/06/2014. The increased indoor concentration at these periods corresponds to working hours (08:00 – 16:00) and is associated with the presence of people. However, the increased concentration at these periods is not only due to human presence but is also highly influenced by penetration from outdoors. Figure 2.5 denotes temporal increases of the outdoor concentration in the period 04 - 06/06/14 similar to the ones observed indoors. Indeed, outdoor particles penetrate indoors and influence the indoor concentration (Tian et al. 2009; Stephens and Siegel 2012), but it is likely that infiltration of outdoor particles is strongest for particle sizes between 0.1 - 0.5 μm (Taylor et al. 1999; Abt et al. 2000; Long et al. 2001; Chen and Zhao 2011), whereas, human activities that resuspend indoor particles influence mostly higher particle sizes (Ferro et al. 2004; Qian and Ferro 2008; Rosati et al. 2008; Shaughnessy and Vu 2012; Serfozo et al. 2014).

Particle number concentration at sizes > 0.5 μm (especially for coarse particles > 1 μm) presents considerable temporal fluctuations during the working days (04-06/06/2014). All periods with increased indoor concentration were located during the working hours (8 am - 4 pm), while no similar behavior was observed outdoors (Figure 2.9). In addition, Table 2.2a proposes that the indoor concentration during working days was considerably higher than that of non-working days. Daily average concentration ranged between 0.08 – 0.16 cm^{-3} during working days, whereas, during non-working days the daily average concentration did not exceed 0.08 cm^{-3}. It is, therefore concluded that during these periods the indoor concentration was highly affected by the presence of people with most probably resuspension of indoor particles as the main reason for increased concentration. On the other hand, indoor concentration of coarse particles outside the working days (07-09/06/2014) was mainly influenced by the outdoor environment, since the office was vacant.

Similar behavior was found for sub-micron particles, where the indoor concentration for particles in the size range 0.014-0.5 μm preserved temporal fluctuation as the one observed outdoors (Figure 2.5a). This finding strongly associates the easier penetration of fine particles indoors compared to coarse particles. Table 2.2a suggests that during some of the non-working days sub-micron particles maintained higher average concentrations compared to working days such that on 03/06/2014 and 09/06/2014 the average indoor concentration (325 and 389 cm^{-3} respectively) was higher than the previous days (02/06/2014 and 08/06/2014). This behavior is associated with increased levels of outdoor concentration at non-working

days, therefore influencing indoor concentration levels. However, an episode of highly increased number concentration was measured on 04/06/2014 inside office A, while, no similar increase took place outdoors (Figure 2.5). Figure 2.9 implies that the increased concentration corresponds to ultrafine particles (< 0.1 μm), whereas, particles between 0.1-0.5 μm were not affected. Number concentration of ultrafine particles reached 3,875 cm^{-3}, while the average number concentration of ultrafine particles inside office A was 255 cm^{-3} during the campaign. The numbers suggest an increase of indoor concentration by a factor of 15.2 compared to the average particle number concentration in office A. It is likely that this increase was provoked by an indoor source. However, according to the diary no special activity took place during the working hours. The recorded activities included only the presence of several people inside the office during meetings (maximum number of persons 3). Therefore, it is believed that the unusual high indoor concentration was transported from indoors. This assumption is supported by the fact that the door was open on 04/06/2014 until 13:00, along with the absence of any hardcopy devices inside the office, which are strongly related to ultrafine particle emissions (He et al. 2007; Destaillats et al. 2008; Koivisto et al. 2010; Salthammer et al. 2012).

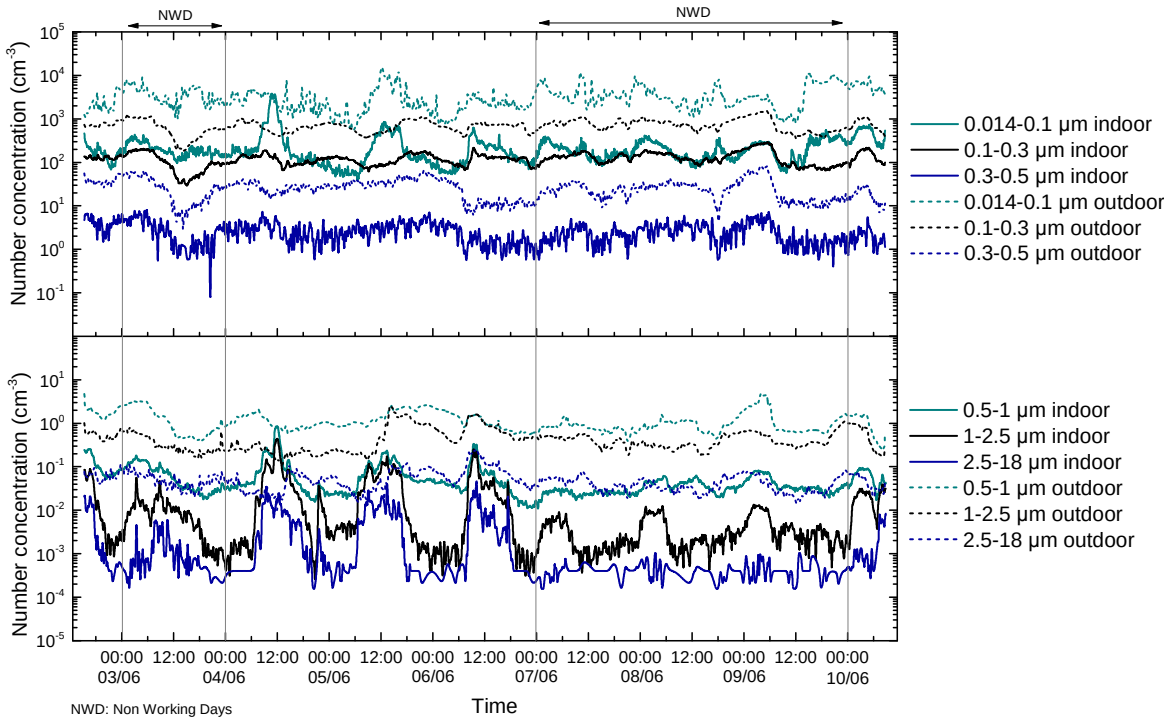

Figure 2.9: Indoor and outdoor number concentration for office A at different size intervals (02-10/06/2014). Comparison between working and non-working days.

In addition, PM_{10} mass concentration was affected by indoor and outdoor sources (Figure 2.7). In the period 04-06/06/2014, which corresponds to working days, the indoor PM_{10} concentration was increased during 8 am to 4 pm in all three cases. Background concentration was between 1-3 μg/m^3, whereas, during the working hours PM_{10} mass concentration reached 4.8, 5 and 5.3 μg/m^3 on 04/06/2014, 05/06/2014 and 06/06/2014 respectively. One local but relatively lower increase of outdoor concentration was observed on 06/06/2014, during the occupied hours. However, it is believed that the indoor concentration was affected by both sources (indoor and outdoor), since indoor PM_{10} concentration reached values similar to those on 04/06/2014 and 05/06/2014, with outdoor concentration almost at the same levels (10 - 30 μg/m^3). Therefore, the increased PM_{10} concentration during 04-06/06/14 was associated with human occupation. On the contrary, in the following days (07-10/06/2014) indoor and outdoor PM_{10} concentration maintained similar temporal fluctuations, implying the significant impact of outdoor particles to the indoor environment. Outdoor PM are found to contribute to indoor levels in naturally ventilated spaces depending on factors such as wind, outdoor concentration and building openings (Liao et al. 2004; Taylor et al. 2014).

2.2.6.2 Office B

Particle number and mass concentrations in office B provide useful characteristics for particle infiltration from outdoors due to the fact that office B was not occupied during the whole campaign. It is evident from Figures 2.6 and 2.8 that infiltration from outdoors was strong for the indoor environment. Indoor number concentration for particles < 0.5 μm (Figure 2.6a) is highly affected by the outdoor temporal fluctuations. Similar characteristic is observed for particles at higher sizes (0.5-18 μm, Figure 2.6b).

In addition, mass concentration was found to depend considerably on outdoor concentration pattern. Figure 2.8 indicates that PM_{10} particles indoors are in strong relationship with outdoor particles. The significant increase of indoor concentration level (11/06/2014) is associated with the same observation outdoors. Several studies have already examined indoor/outdoor relationship of PM and correlated the indoor concentration with the outdoor environment (Ekberg 1996; Long and Sarnat 2004; Cao et al. 2006; Park et al. 2014; Szigeti et al. 2014; Zhao et al. 2015; Zhu et al. 2015). Although, values after 6 pm on the same day were excluded due to the very low measured indoor concentration (reaching detection limits of the instrument), it is important to note that the minimal concentration indoors was the result of the considerable decrease of outdoor PM_{10} concentration (from 43 μg/m^3 to 5 μg/m^3). Taking into account that the office was vacant and no indoor source was present. For this reason, we could not associate the

opening of the window on 12/06/14 (for one hour 14:30 – 15:30) with PM_{10} behavior but we have incorporated the results only with number concentration data.

The effect of the opening of the window to different particles sizes is shown in Figure 2.10, where, the indoor particle number concentration at different size intervals in office B is plotted against time only for the day where the window was opened (12/06/2014). It is demonstrated that the opening the window had no effect on sub-micron particles (Figure 2.10a). The colored area, which corresponds to the time-period when the window was open, suggests that indoor number concentration for all three size intervals (0.014 - 0.1 μm, 0.1 - 0.3 μm and 0.3 - 0.5 μm) presented no significant temporal fluctuation, rather than followed levels similar to the ones before (and after) opening the window. Hence, it is concluded that ultrafine particles penetrate easily inside the building regardless the window was open or not. However, the decreased concentration indoors for at least one order of magnitude in each size interval indicates the successful removal of a major fraction of outdoor ultrafine particles probably through the ventilation system.

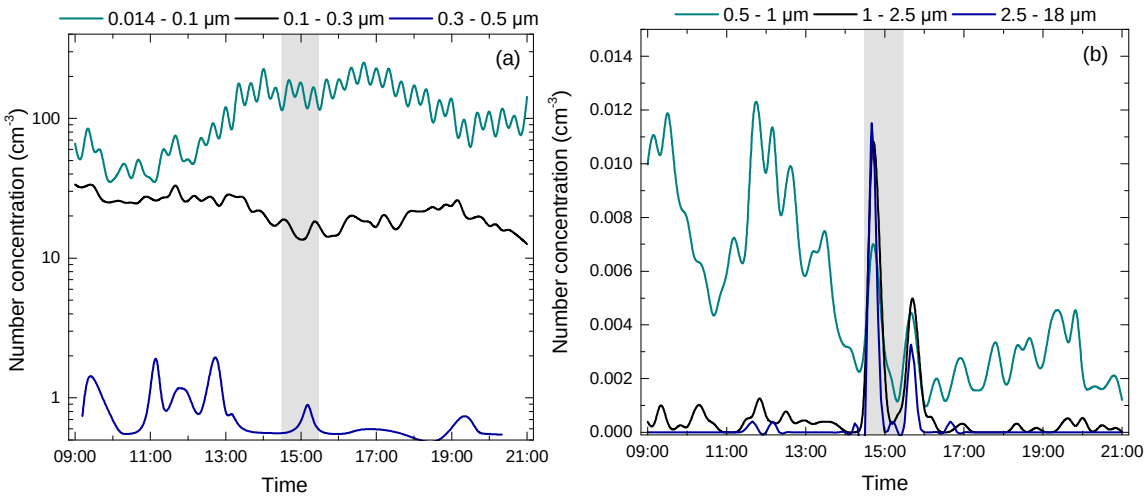

Figure 2.10: Indoor particle number concentration in office B on 12/06/2014. Comparison between different size intervals a) 0.014-0.5 μm and b) 0.5-18 μm. Colored areas represent the opening of the window.

A different behavior is observed for bigger particles (Figure 2.10b). Number concentration of particles for the three size intervals (0.5 - 1 μm, 1 – 2.5 μm, 2.5 - 18 μm) increased immediately while the window was opened. This finding suggests that particles from outdoors at this size range enter inside the building resulting in a substantial increase of indoor concentration. It is well-known that particle penetration at

coarse fraction is limited due to their relatively large size (Diapouli et al. 2013), therefore, the opening of the window resulted in easier penetration of coarse particles indoors. The present findings are in agreement with studies that estimate particle penetration from outdoors and contribution of outdoor sources (Long et al. 2001; Chen and Zhao 2011).

2.2.7 I/O ratio

Indoor to outdoor ratio for both offices was significantly less than 1. Figure 2.11a presents the I/O ratios using the number concentration data at different size intervals and Figure 2.11b presents the I/O ratio for mass concentration data. Particles in the size intervals between 0.014-0.1, 0.5-1, 1-2.5 and 2.5-18 μm preserved higher ratios in office A than in office B. Since, I/O ratio is easily affected by indoor sources (Matson 2005; Challoner and Gill 2014) it is likely that higher ratios observed in office A are due to office occupation. Higher I/O ratio in occupied buildings or offices is also reported in Quang et al. (2013) and in Challoner et al. (2014). Ultrafine particles in office A were influenced by the indoor event on 04/06/2014, where considerably higher concentration was measured. On the other hand, higher ratios for coarse particles are associated with indoor resuspension activities.

A comparison between occupied and non-occupied hours for number and PM_{10} data is presented in Figure 2.12. It is demonstrated that the I/O ratio is higher during occupied hours in all three cases with average ratio 0.22, 0.20 and 0.24 for number (0.014 - 0.5 μm, 0.5 - 18 μm) and PM_{10} respectively. Non-occupied hours presented substantially lower ratios with the highest average ratio 0.17 (PM_{10}). Additionally, Figure 2.11a indicates similar ratios between office A and office B for the size intervals 0.1-0.3 and 0.3-0.5 μm. This finding is related with infiltration of outdoor particles. It indicates that building characteristics and ventilation system has the same impact for indoor particle dynamics, although measured at different offices. Low I/O ratios for particles > 1 μm in office B are due to negligible indoor concentration at these size fractions (vacant office).

I/O ratio for PM_{10} particles presented similar characteristics with number concentration data, thus, office A was characterized by higher I/O ratios compared to office B (Figure 2.11b). Moreover, it is observed that I/O ratio for PM_{10} is shifted to higher values compared to number concentration data with average I/O ratio at 0.18 for PM_{10} in office A, while, the highest I/O ratio for coarse particles was at 0.06 (1-2.5 and 2.5-18 μm). Several studies propose that human resuspension activities are associated with emissions at higher particle sizes (> $PM_{2.5}$) (Thatcher and Layton 1995; Ferro et al. 2004; Qian et al. 2014; Serfozo et al. 2014), which is in agreement with the presented results.

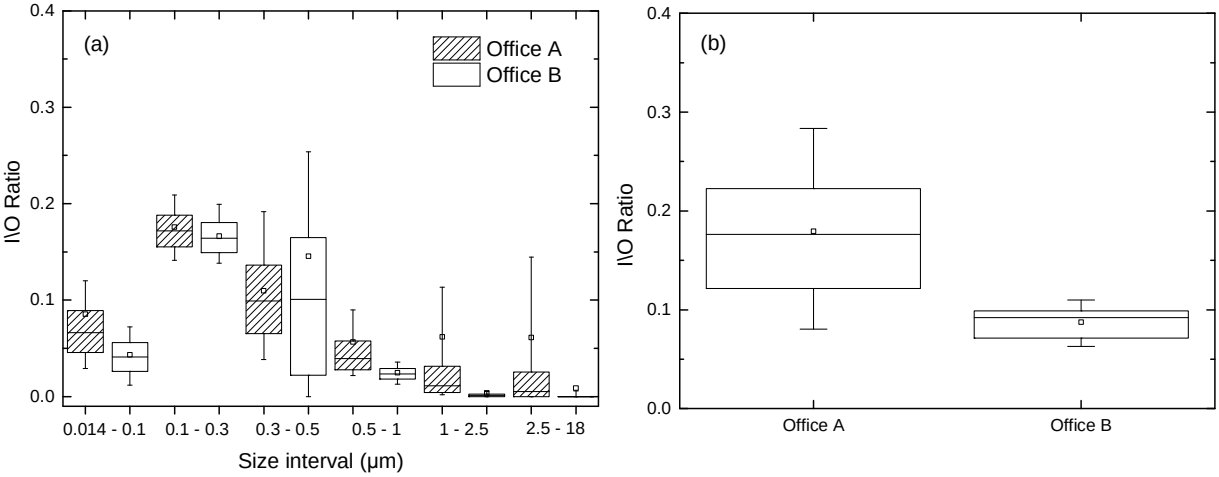

Figure 2.11: a) I/O ratios of number concentration data at different size intervals, b) I/O ratios of mass concentration data. Comparison between office A and B. The box plots represent the 25th and the 75th percentile values, mean value and the horizontal line the median (50th percentile) value. The whiskers represents 10th and 90th percentile. Outliers are excluded.

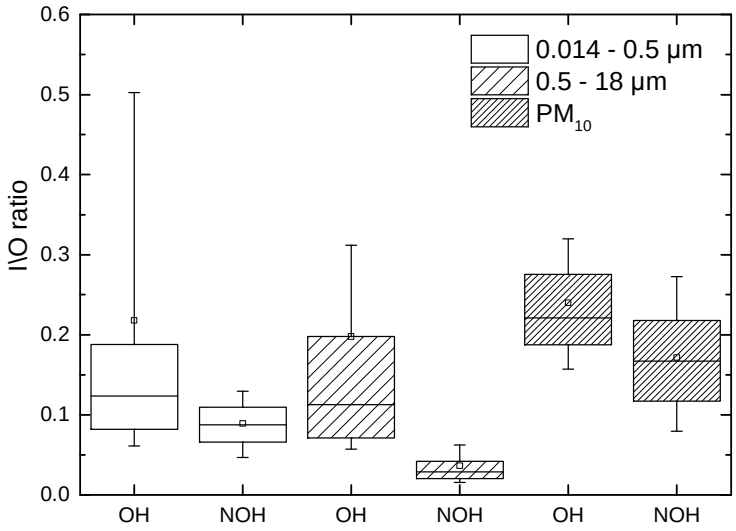

Figure 2.12: Comparison of occupied and non-occupied hours in office A for number concentration (0.014 - 0.5 µm, 0.5 - 18 µm) and mass concentration data (PM_{10}). The box plots represent the 25th and the 75th percentile values, mean value and the horizontal line the median (50th percentile) value. The whiskers represents 10th and 90th percentile. Outliers are excluded.

Additionally, Figure 2.11a provides a relation between particle size and infiltration from outdoors. I/O ratios presented higher values for accumulation fraction (0.1-03 and 0.3-.0.5 µm) for both offices.

Moreover, considerably lower ratios were found for particles > 0.5 μm and for particles < 0.1 μm. This finding is closely associated with particle dynamics, where, easier penetration and higher infiltration corresponds to particle sizes in the range 0.1 - 0.5 μm (Bennett and Koutrakis 2006), whereas, infiltration of ultrafine particles is limited due to Brownian diffusion (Nazaroff 2004) and infiltration of coarse particles is likely less effective due inertial impaction and gravitational settling (Chen and Zhao 2001). Several studies that examined the contribution from outdoor sources to indoors confirm the present findings (Abt et al. 2000; Long et al. 2001; Matson 2005; Cao et al. 2006; McAuley et al. 2010; Chen and Zhao 2011; Stephens and Siegel 2012; Sangiorgi et al. 2013; Chatoutsidou et al. 2015).

The numbers also suggest low I/O ratios in both offices (Figure 2.11a and 2.11b). Low I/O ratios (< 0.5) in a mechanically ventilated building are also reported in Fisk et al. (2000). Despite the strong influence from outdoors, I/O ratio was usually less than 0.3. Median for particles < 0.5 μm reached 0.17, while, for particles > 0.5 μm the highest value was 0.04, indicating that a big fraction of outdoor particles remains outside the building (Figure 2.11a). The values also suggest that enrichment of the offices at lower particle sizes (0.014 - 0.5 μm) are likely caused from penetration from outdoors, whereas, for bigger particles (> 0.5 μm) infiltration from outdoors is considerably reduced due to efficient removal of coarse particles by the filters. The results also ensure that exposure to indoor PM and PN is substantially reduced compared to outdoor levels. Therefore, the ventilation system prevents the entrance of a major fraction from outdoors together with the building envelope that serves as natural particle filter when ventilation is off.

2.3 Measurement of particle concentrations in offices in Greece

2.3.1 Sampling site

Indoor/outdoor one-week sampling campaign was conducted at the Technical University of Crete, Greece during May (19-25) 2015. Indoor sampling was performed in a building located in the university campus that belongs to the School of Environmental Engineering. Outdoor sampling was sited 50 m away from the under study building in approximately 1.5 m above the ground. The area surrounding the university campus corresponds to an urban/semi-rural area and is 5 km north-west of the city of Chania. Detailed description of the area can be found in Lazaridis et al. (2008) and in Kopanakis et al. (2013).

The building consists of offices and computer rooms on the ground floor and offices and a few laboratories on the first floor. All offices and laboratories in each floor are connected to a main corridor, which uses two exits one at each end. The two floors are connected through an elevator, internal stairs and square-

shaped openings areas of 4 m^2 on the ceiling of the ground floor, thus give a feeling of internal balcony. The building is occupied daily on weekdays during open hours, i.e. 08:00 to 21:00.

The building is equipped with mechanical ventilation and separate air condition (AC) system, both of them operated manually by the occupants. Mechanical ventilation uses district ventilation ducts for entrance and exhaust of the airflows. Therefore, the offices are connected with each other through ventilation ducts, depending on their location in the building.

Four offices were selected one of them corresponding to a printer room. Two of them are located on the ground floor and two of them are located on the first floor. Figure 2.13 shows the internal layout of each floor and the location of each office. The offices are of rectangular shape and are connected to outdoors with one window and to indoors with one door. All selected offices face the north side of the building.

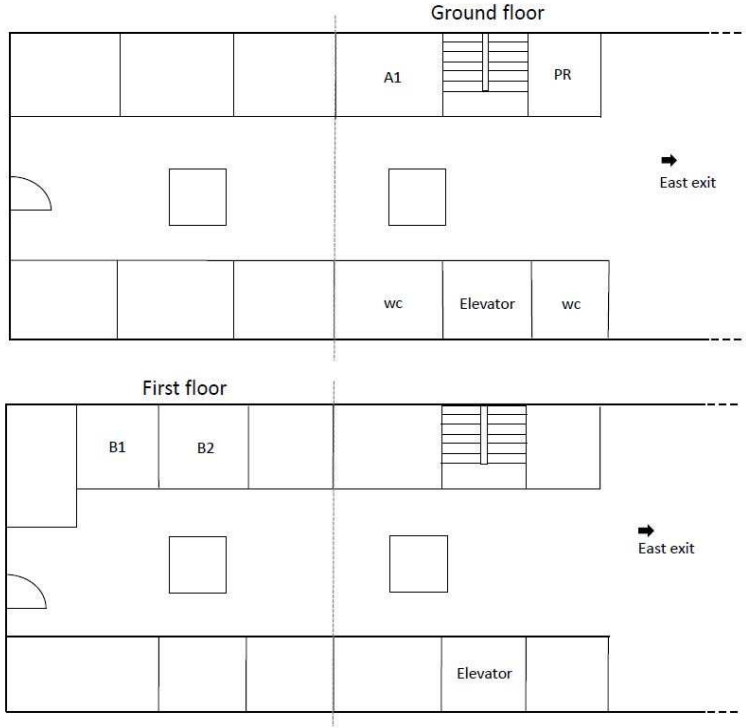

Figure 2.13: Internal layout of each floor and location of each office.

Mechanical ventilation was turned off during the campaign but the air condition system was selectively used by the occupants.

Table 2.3 summarizes the location and use profile for each office. Office A1 was occupied permanently by 2-3 people, but other people entered the office occasionally for a short period. No hardcopy device was present inside A1 but common office equipment (personal computers, telephones) whilst furniture (desks, chairs, shelves, closet) cover the internal area. On the contrary, PR is a printer room where 4 professional printers (Xerox 4110 PS, HP LaserJet 550 and two HP LaserJet 9050) were operated by the users of the building during open hours (08:00-21:00). PR was not permanently occupied but instead several people enter the room briefly. Office B1 was permanently used by 2 people, whereas, office B2 was very rarely occupied. Both offices were covered with common office equipment and furniture like A1. Indoor activities in all occupied offices were recorded in a diary. Windows in all offices were closed during the campaign and smoking was not allowed. The doors in PR and A1 were

constantly opened during open hours of the building, whereas, the doors of B1 and B2 were opened only to enter or exit the office.

Table 2.3: Location, surface area and use profile of each office.

Office	Floor	Surface Area (m^2)	Mechanical ventilation	Air condition	Door open	Window open	Occupation
PR	0	17	no	daily	during open hours	no	during open hours
A1	0	17	no	daily	during open hours	no	during open hours
B1	1	17	no	occasionally	no	no	during open hours
B2	1	17	no	no	no	no	rarely

2.3.2 Instrumentation

Particle number size distribution was measured with a NanoScan SMPS (TSI) 3910, an OPS (TSI) 3330 and an SMPS+C (CPC Model 5.403 and L-DMA - Vienna type, GRIMM). NanoScan was logging the data every 1 min in 13 channels from 0.011 to 0.42 µm. OPS was using a 5-min log interval and recorded particle size distribution from 0.3 to 10 µm in 16 channels. SMPS+C was taking a sample every 6 min and 46 s at flow rate 0.3 lpm in the size range from 0.011 to 1 µm in 44 channels. Additionally, particle number concentration was measured by two P-Traks 8525 (TSI) with a 5-min log interval at flow rate 0.1 lpm.

Indoor particle mass concentration was measured with a DustTrak II 8532 (TSI) at flow rate 3 lpm, a DustTrak 8520 (TSI) at flow rate 1.7 lpm and a DustTrak DRX 8534 (TSI). Outdoor particle mass concentration was measured with a DustTrak II 8530 (TSI) at flow rate 3 lpm. The log interval was chosen at 5 min for all instruments. All DustTrak used a PM_{10} head to sample, whereas, DustTrak DRX measured size-segregated mass fractions for PM_1, $PM_{2.5}$, PM_{10} and respirable particles.

In addition to online monitor of particle number and mass concentrations, black carbon was measured using a MicroAeth AE51 with time resolution 1 min and flow rate at 100 ml/min. Indoor temperature and relative humidity was recorded with Tiny Tag data loggers. Table 2.4 lists which sampling instrument was placed at each office.

Side-by-side tests were conducted for all DustTraks. The PM_{10} concentration was measured during background measurements in a chamber of 7.6 m^3 volume equipped with a HEPA filter (EN 1822). Background measurements were performed whilst incense burning was used as a source for indoor particles. The following least square linear relationships were obtained between the instruments:

$$DTII(8532)[\mu g/m^3] = 1.41DRX + 2.47$$
$$DTII(8532)[\mu g/m^3] = 1.26DTI(8520) + 3.80$$
$$DTII(8532)[\mu g/m^3] = 0.99DTII(8530) - 7.11$$

All measured data from the DustTrak II 8532, DustTrak I 8520 and DustTrak DRX 8534 were converted to the equivalent DustTrak II 8532 reading. Subsequently, all DustTrak II 8532 readings (measured and equivalent) were corrected through the gravimetric instrument Sequential Sampler FH 95 SEQ, THERMO, by operating side-by-side for 10 days. The following least square equation was obtained:

$$corrected\ PM_{10}[\mu g/m^3] = 0.31DTII(8532) + 5.07$$

Table 2.4: Sampling instrument placed at each office.

	PR	A1	B1	B2	Outdoor
PN concentration					
NanoScan	x				
OPS	x				
SMPS+C			x		
P-Trak 8525		x			
P-Trak 8525				x	
PM concentration					
DustTrak II 8532		x			
DustTrak I 8520				x	
DustTrak II 8530					x
DustTrak DRX 8534	x				
Other					
MicroAeth	x				
Tiny Tag	x	x			

2.3.3 PN concentrations in Printer Room

The measured $PN_{0.011\text{-}0.4}$ concentration inside PR during the campaign is plotted in Figure 2.14 along with the total number of printed pages. It is seen that $PN_{0.011\text{-}0.4}$ concentration preserved lower concentrations on weekends and on workdays during closed hours (21:00-08:00). These periods were considered as background concentrations mostly affected by the outdoor concentration. Median concentration during

these hours was 3,080 cm^{-3} for $PN_{0.011-0.4}$. Moreover, Figure 2.14 indicates a substantial increase of the indoor particle number concentration early in the morning (08:00-09:00) for workdays, which is not associated with any printing activity. Peak concentration reached 28,320, 39,672, 30,217, 33,378 and 46,506 cm^{-3} for 19/05, 20/05, 21/05, 22/05 and 25/05 respectively. This sharp increase usually lasted for 5 min and was caused by cleaning of the corridor just outside PR. Emissions from cleaning agents usually involve particle generation in the ultrafine region (Huan et al. 2011; Nørgaard et al. 2014) as the product of secondary organic aerosol formation by primary VOC emissions (Nazaroff and Weschler 2004; Coleman et al. 2008). Ozone-initiated reactions are favored especially in rich-ozone indoor environments such as workplaces equipped with photocopiers or laser printers (Weschler 2000). Figure 2.15 demonstrates that cleaning-generated particles lie in the ultrafine region with the dominant particle size being always at 0.5 μm for all five cases.

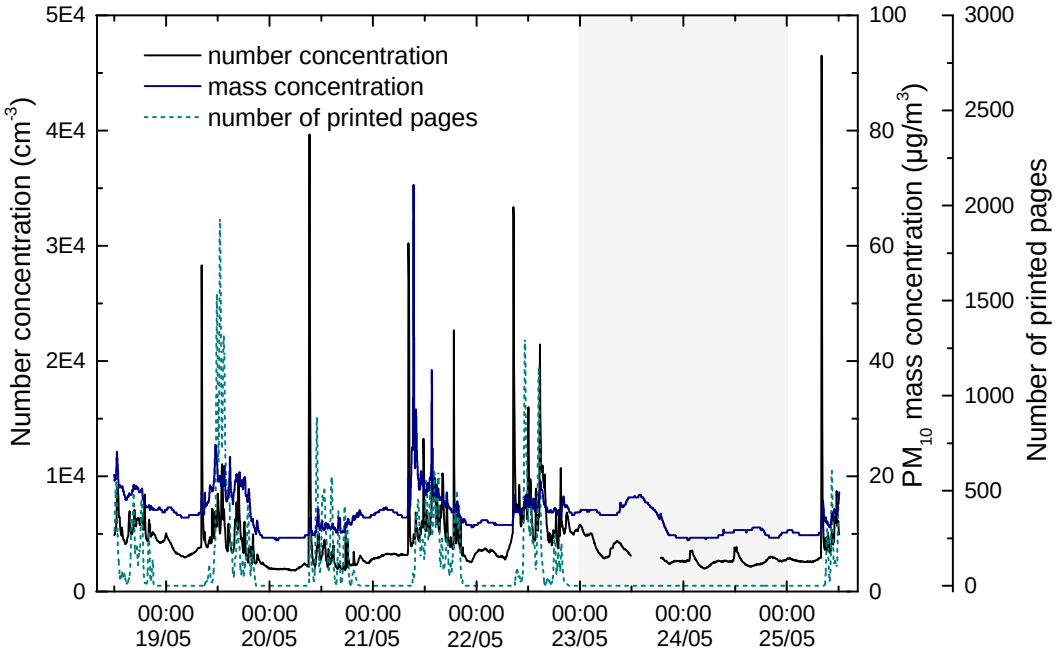

Figure 2.14: Particle number concentration $PN_{0.011-0.4}$ and PM_{10} concentration in the printer room (PR). Also shown the total number of printed pages during the campaign. The highlight area corresponds to weekend.

However, the most important contribution to sub-micron particles indoors in terms of long exposure originated from printer emissions. Although, daily variations of the number of printed pages was observed, more than 3,000 pages were printed in total during each workday. Printing periods, which correspond to

periods with printing activity, were identified usually between 09:00 and 21:00 on workdays. Figure 2.14 indicates that during these periods $PN_{0.011-0.4}$ concentration was considerably higher compared to no printing periods (night hours, weekend). Median concentration during printing periods was 4,933 cm^{-3}.
The impact from printer emissions in particle size is highlighted in Figure 2.16. Figure 2.16a demonstrates that ultrafine PN concentration varied temporarily with sharp increases leading to substantially higher indoor concentration during day time (printing period), compared night time (no printing period) where no activity took place (Figure 2.16c). On average, $PN_{0.01-0.1}$ concentration between 09:00 and 21:00 was 1.2 times higher compared to night time during the campaign. In addition, particles in the size range 0.1-0.4 μm presented higher concentration during daytime (Figure 2.16b), although the corresponding concentrations were significantly lower than that of $PN_{0.01-0.1}$.

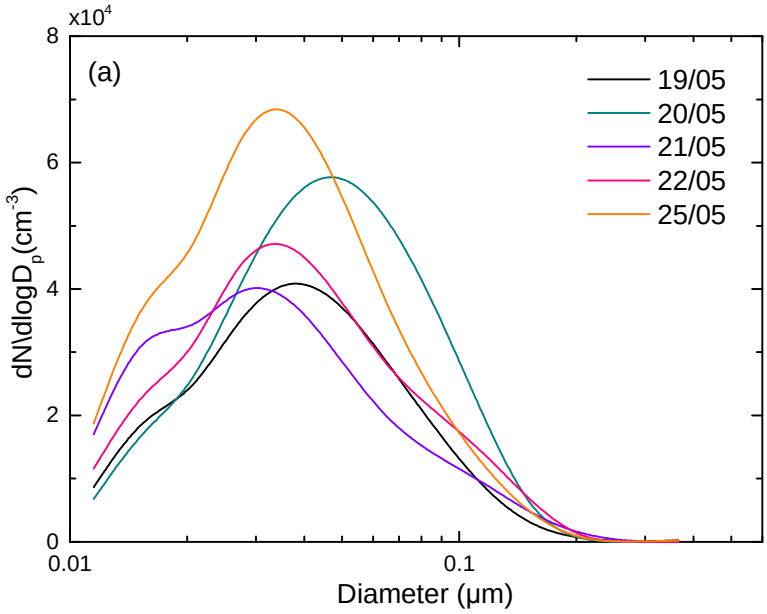

Figure 2.15: Particle number size distribution ($dN/dlogD_p$) of peak concentration in PR during cleaning of the corridor.

The sharp increases of indoor PN concentration for ultrafine particles during printing periods are associated with primary emissions from the printers. Hardcopy devises and printers are known for their effect on indoor PN concentration and especially in particle sizes < 0.1 μm (Schripp et al. 2008; Wensing et al. 2008; McGarry et al. 2011). Recent investigation on emissions characteristics from laser printers suggests that particles are of secondary nature and are formed in the air from VOCs, emitted by the printers. This effect leads to ultrafine particle generation indoors, either by homogenous nucleation or

secondary particle formation (Morawska et al. 2009). On the other hand, the increased concentration in higher size classes (0.1-0.4 μm) is attributed to coagulation of ultrafine particles. Thus, $PN_{0.1\text{-}0.4}$ concentration maintained lower levels than $PN_{0.01\text{-}0.1}$ concentration but still higher compared to no printing period (Figure 2.16d). However, indoor PN concentration for sub-micron particles during night time is likely influenced by outdoors. Therefore, sub-micron particle concentration in PR is substantially affected by printer emissions.

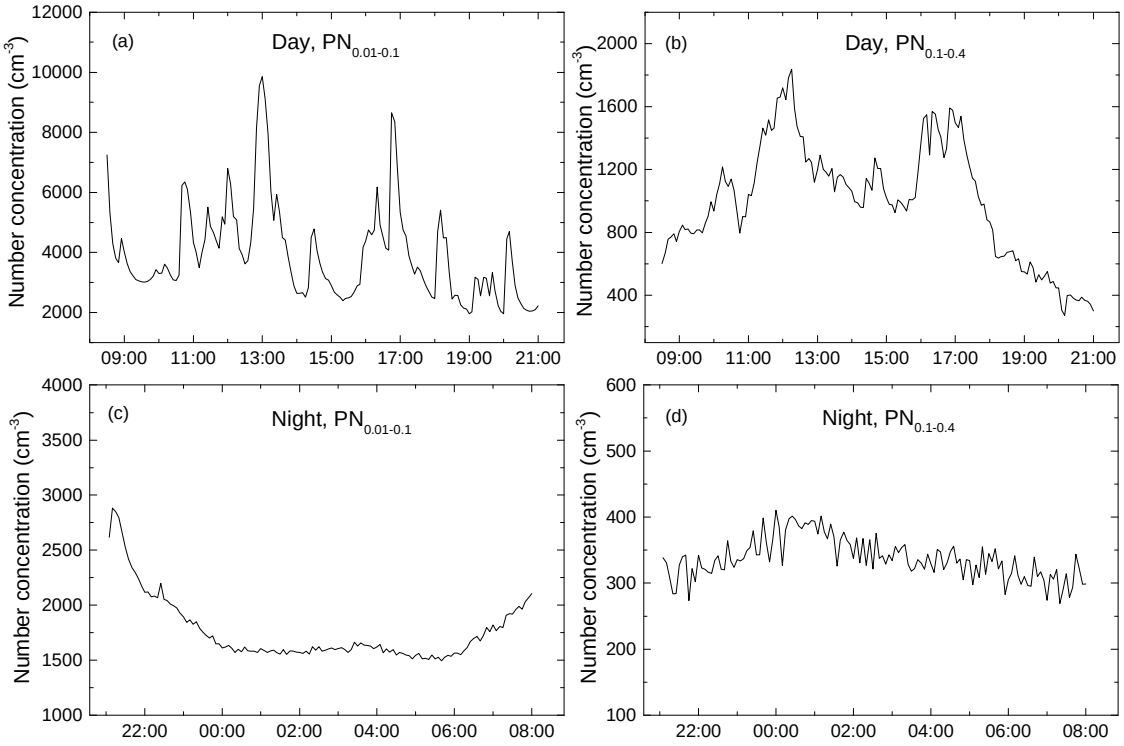

Figure 2.16: Particle number concentration at different size ranges in PR during day (printing period) and night (no printing period) hours. The data correspond to 19/05 and the following night.

2.3.4 PM concentrations in Printer Room

PM_{10} concentration in PR is presented in Figure 2.14 along with $PN_{0.011\text{-}0.4}$ concentration. It is observed that PM_{10} concentration is considerably influenced by printer emissions. Median concentration during printing periods was 15 μg/m^3, whereas, during no printing periods it was 12 μg/m^3 suggesting an increase of 25%. The impact from printer emissions in PM_{10} concentration is associated with particles < 1 μm. Figure 2.17a demonstrates that high correlation (R^2=0.87) was obtained between PM_1 concentration and $PN_{0.4\text{-}1}$. This

finding suggests that PM_1 concentration in PR is directly linked with fine particle number concentration, the particle size that is highly influenced by the use of printers.

Moreover, Figure 2.17b presents PM_x ratios in PR. Accordingly, both PM_1/PM_{10} and $PM_{2.5}/PM_{10}$ ratios preserved ratios higher than > 0.9 during periods where the building was not occupied (workdays 21:00-08:00, weekend) for both cases. In practice, a diurnal variation for both ratios was observed during working days, whereas, during the weekend no diurnal variation was present. $PM_{2.5}/PM_{10}$ reached a ratio almost equal to 1 during the closed hours (21:00-08:00) on weekdays suggesting that indoor PM during night inside PR is dominated by smaller micron-sized particles and that coarse particle concentration (> $PM_{2.5}$) is negligible, i.e. not suspended in the air. The same behaviour applies for PM_1/PM_{10} but with lower ratios since PM_1 are included in $PM_{2.5}$. Similar results were obtained for the weekend where the office was constantly unoccupied. Therefore, sub-micron particles most probably originate from outdoors during closed hours due to infiltration since the printers are not working, whereas, during day hours the contribution from coarse particles becomes important.

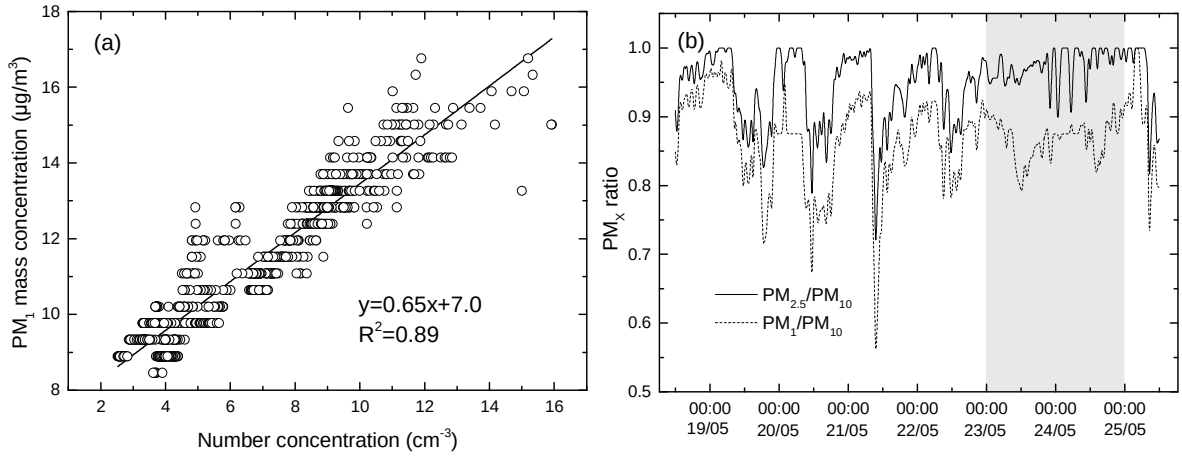

Figure 2.17: a) Correlation between PM_1 concentration and particle number concentration $PN_{0.4\text{-}1}$ in PR. The line corresponds to the linear fit between them, and b) PM_x ratios (PM_1/PM_{10} and $PM_{2.5}/PM_{10}$) inside PR. The highlighted area corresponds to weekend.

In more detail, ratios < 0.9 both for PM_1/PM_{10} and $PM_{2.5}/PM_{10}$ were obtained only during open hours (08:00-21:00), implying that coarse particles (> 2.5 µm) are significantly suspended during day time most notably due to particle resuspension. Particle size and resuspension are associated in many studies (Qian et al. 2008; Serfozo et al. 2014; Hussein et al. 2015). Note also that the PM_1/PM_{10} ratio reached its lowest value on 21/05 which coincides with a substantial increase of PM_{10} concentration in the same day (Figure

2.14), caused by cleaning activities inside PR. Sarwar et al. (2004) and Nørgaard et al. (2014) has shown that the use of cleaning products (general purpose cleaner, floor cleaner) causes an immediate increase in particle mass concentration along with particle number concentration due to fine particle formation/growth. Moreover, cleaning activities (dusting, vacuuming) can cause increased concentration of coarse particles due to resuspension (Ferro et al. 2004). However, in the rest of the workdays (no cleaning) resuspension of coarse particles is attributed to human walking or the physical presence of the occupants.

2.3.5 I\O ratio

The I\O ratios obtained from mass concentration data (Figure 2.18) were higher than 0.90 (10^{th} percentile) for all three offices (PR, A1, B2). This finding strongly suggests that the indoor PM_{10} concentrations preserved values considerably higher than the outdoor levels, therefore, implies the presence of indoor sources. PM I\O ratios higher than 1 in commercial buildings are also reported in Challoner et al. (2014).
Higher I\O ratios were obtained for B2, which is in agreement with the substantially higher indoor PM_{10} concentrations measured in B2 (Table 2.5). The I\O ratio varied between 1.42-2.10 with a mean value at 1.71. No indoor source was recorded in B2 (it was very rarely occupied) besides cleaning of the office on 21/05 (higher daily median PM_{10} concentration, 23 $\mu g/m^3$). Cleaning of B2 resulted in a sharp short-term increase of PM_{10} as seen in PR due to the use of cleaning agents. Nevertheless, it is believed that the higher I\O ratios obtained for B2 are due to particle transport from another internal area through gaps of the door or from the ventilation ducts. It is likely that indoor PM_{10} concentration in the office was influenced by that of other offices through ventilation ducts when mechanical ventilation was off. Accordingly, forced airflows inside the ventilation ducts prevent air mixing between the offices when mechanical ventilation is operating, whereas, the opposite behaviour is not ensured when mechanical ventilation is not operating. Thus, it is likely that the high concentrations are associated with an indoor source originating from another office which is connected with B2 with the same ventilation duct.
A comparison between offices PR and A1 (occupied offices) suggests that PR was characterized by slightly higher I\O ratios. Mean values were 1.24 and 1.18 for PR and A1 respectively. The difference between the two offices is associated with printer emissions and especially the fine particle fraction. Enrichment with particles < 1 μm in PR, caused by the use of printers during open hours, lead to higher PM_{10} concentrations compared to the PM_{10} concentrations measured in A1. It is well-established that the physical presence of people in indoor environments has impact on coarse particles (Fisk et al. 2000; Qian and Ferro 2008; Shaughnessy and Vu 2011; Chatoutsidou et al. 2015; Hussein et al. 2015) due to particle resuspension.

However, the present results demonstrate that printing emissions in PR had bigger impact on PM_{10} concentration than particle resuspension due to human occupation. Figure 2.17b shows that the PM_1 concentration -sub-micron particles- dominated the indoor air in PR with PM_1/PM_{10} being usually above 0.7, whilst the median $PM_{>2.5}$ concentration during the campaign was at 0.44 μg/m^3.

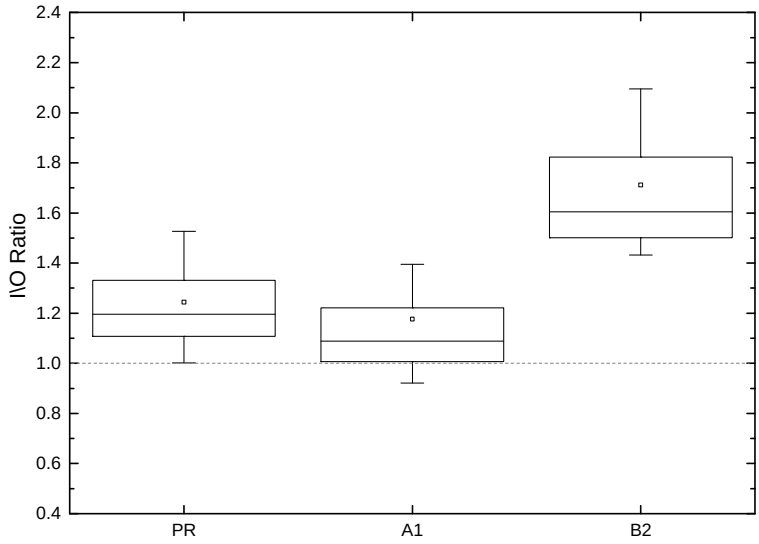

Figure 2.18: I\O ratio for offices PR, A1 and B2 obtained from mass concentration data. The box plots represent the 25th and the 75th percentile values, mean value and the horizontal line the median (50th percentile) value. The whiskers represents 10th and 90th percentile. Outliers are excluded.

Lastly, no operation of the mechanical ventilation in the under study offices is believed to contribute to the high I\O ratios reported in the present study. Studies that have investigated the impact of mechanical ventilation confirm that the operation of the HVAC system results in reduced I\O ratios indoors both for fine and coarse particles (Park et al. 2014; Quang et al. 2013).

Table 2.5: Indoor daily median PM_{10} mass concentration for offices PR, A1 and B2.

	18/05	19/05	20/05	21/05	22/05	23/05	24/05	25/05
PR	16	14	11	14	14	14	10	10
A1	17	13	10	13	13	13	9	9
B2	-	-	18	23	19	21	12	13

2.3.6 Impact of printer emissions in other offices

The use of printers influenced substantially both the PN and PM concentrations in PR. In turn, printer emission had significant impact in other offices due to particle transport. PM_{10} concentrations in A1 and B2 were found to correlate significantly with PM_{10} concentrations in PR. Figures 2.19 and 2.20 present the correlation of PM_{10} concentration in each office with the PM_{10} concentration in PR and with the outdoor concentration. All data correspond to printing hours, i.e. 09:00-21:00. It is observed that higher correlation was found between the PM_{10} concentrations in the under study offices and PR. Specifically, R^2 was 0.74 between the PM_{10} concentration in A1 and PR, whereas, R^2 was 0.47 between the PM_{10} concentration in A1 and the outdoor concentration. For B2 the same observation was found but with lower correlation for both cases. Thus, R^2 was 0.69 between the PM_{10} concentration in B2 and PR and 0.47 between B2 and outdoors. These findings demonstrate that PM_{10} concentrations in A1 and B2 are primarily affected by the PM_{10} concentration in PR due to particle transport through the internal areas of the building. Nevertheless, the outdoor environment is an important but weaker contribution to indoors during occupied hours.

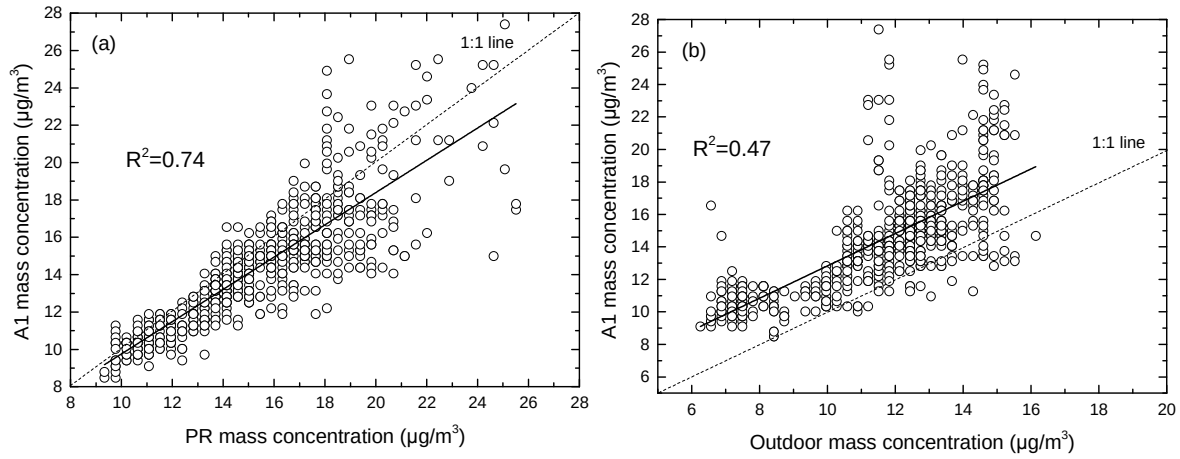

Figure 2.19: Correlation of PM_{10} concentrations between: a) A1 and printer room (PR), and b) A1 and the outdoor concentration.

In addition, Figures 2.21a and 2.21b present the correlation between A1 and B2 with PR using the number concentration data. Again, good agreement was found between $PN_{<1}$ concentrations for both cases with R^2 0.63 and 0.60 for A1 and B2 respectively. Although, parallel correlation with the outdoor data is missing in this case, the present results confirm the impact of sub-micron particles originated from PR but transported to other offices. Recall that A1 was occupied during open hours, hence human presence in A1

had negligible impact on indoor PN concentration for sub-micron particles. Fine particles are not effectively escaped as coarse particles due to their smaller inertia that allows them to be influenced by airflow patterns of the building, momentum jets and eddies indoors (Kao et al. 2009). Internal airflows, location and magnitude of the emissions influence substantially particle transport indoors (McGrath et al. 2014), thus variations may be observed from day to day. Therefore, smaller particles are easily transported to internal areas of the building compared to bigger particles.

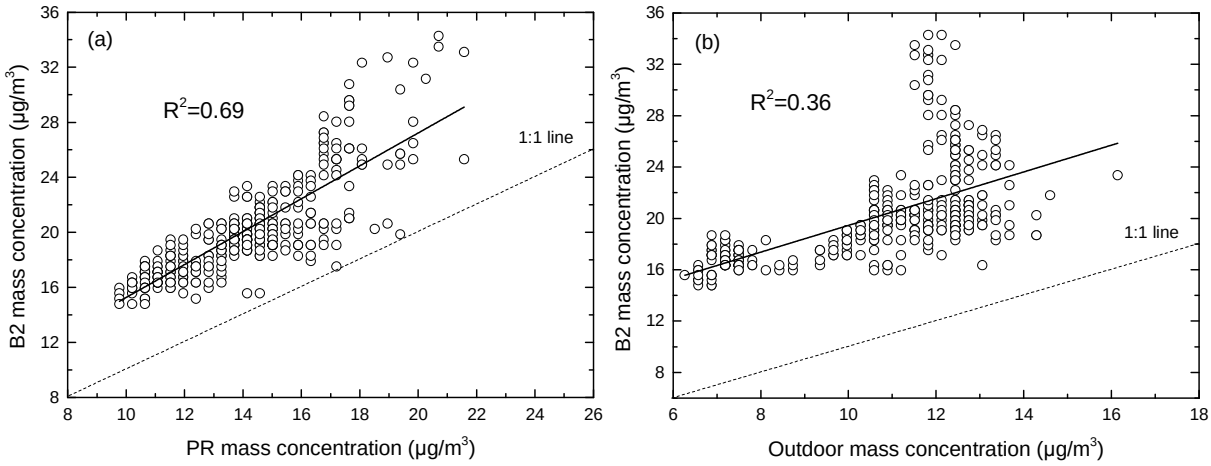

Figure 2.20: Correlation of PM_{10} concentrations between: a) B2 and printer room (PR), and b) B2 and the outdoor concentration.

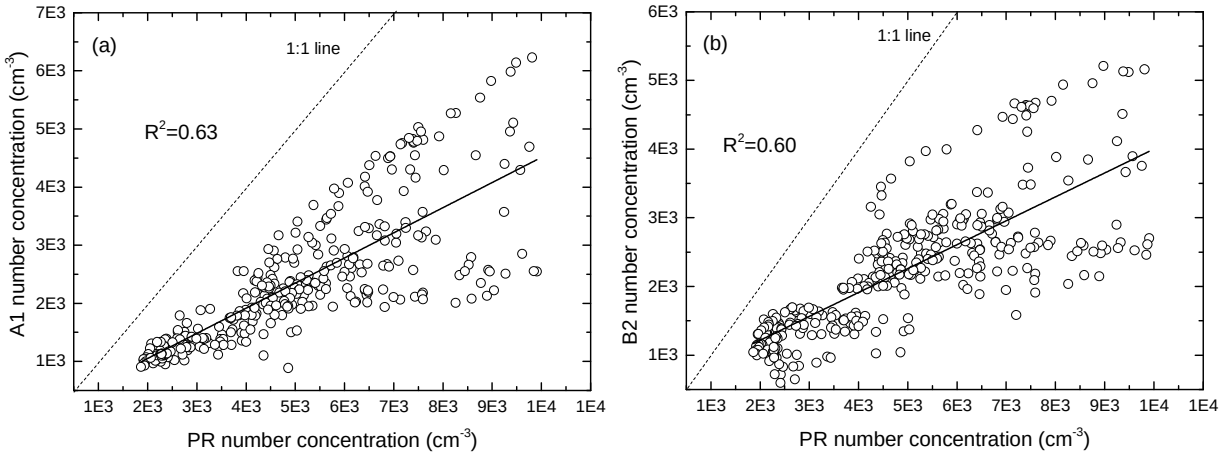

Figure 2.21: Correlation of $PN_{<1}$ concentrations in printer room (PR) with offices A1 (a) and B2 (b).

Moreover, the relative higher correlation obtained for A1 compared to B2 (both for PN and PM concentrations) is associated with the location of each office. It is likely that A1 is more effectively

influenced by printer emissions because the office is located closer to PR and at the same floor (ground floor). However, the present results imply that the impact from printer emissions is significant and that sub-micron particle transport indoors is important to other locations of the building.

Lastly, Figure 2.22a compares the $PN_{<1}$ concentration in B1 and PR, whilst, Figure 2.22b presents the correlation between $PN_{<1}$ concentration in the two offices only during the printing periods. Successful correlation was succeed using 30-min average values due to different time intervals used by the instruments. Sub-micron particles originated by cleaning of the corridor on the ground floor had major impact to PN concentrations in PR, but similar observation was not identified for B1 as shown in Figure 2.22a. $PN_{<1}$ concentration in B1 was not affected by the sharp short-term increase of ultrafine particles in PR during morning hours. However, number concentration of particles in both offices was nearly at the same levels, although the offices located at different floors and with the door of B1 being usually closed. Average $PN_{<1}$ during printing hours (09:00-21:00) was 4,354 cm^{-3} and 5,372 cm^{-3} in B1 and PR respectively. Higher average PN concentration in PR is attributed to printer emissions, which in turns highlights the importance of the location of the source in a multi-zone building.

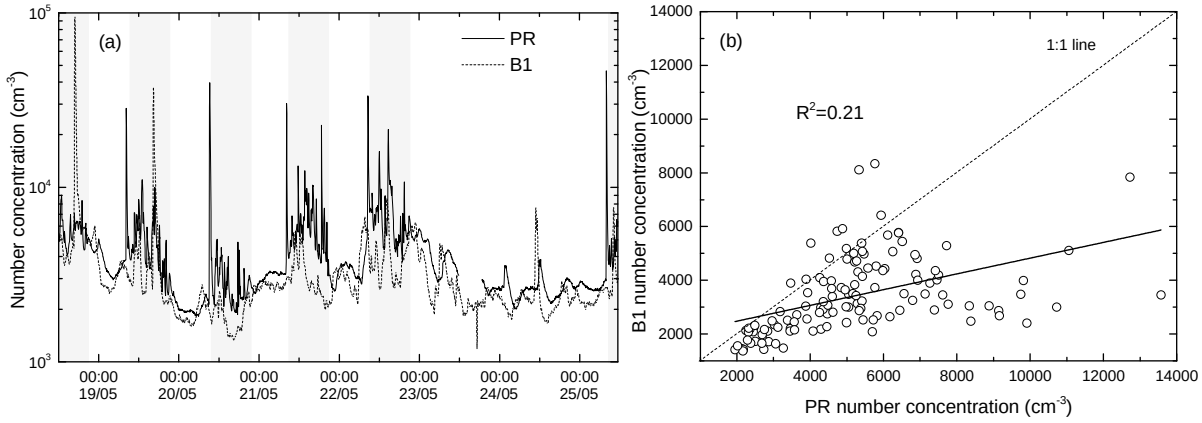

Figure 2.22: a) $PN_{<1}$ concentrations in B1 and PR. The highlight areas corresponds to printing periods (09:00-21:00), and b) correlation between $PN_{<1}$ concentrations in B1 and PR only for printing periods.

Figure 2.22b indicates a lower correlation (R^2=0.21) of $PN_{<1}$ concentrations between B1 and PR compared to the ones obtained for A1 and B2. A possible reason is the use of average values, which can affect the results. However, it is observed that on 18/05 and 19/05 the indoor $PN_{<1}$ concentration in B1 was affected by indoor concentration in PR and preserved similar temporal fluctuations, a finding that can be observed in the rest of the workdays but with lower extend. This conclusion is further confirmed since no indoor source associated with emission of fine particles was present inside B1 during the campaign except the

physical presence of the occupants. On the other hand, $PN_{<1}$ concentration of sub-micron particles during night and weekend in both offices is believed to be influenced by outdoors. In this case, the outdoor contribution becomes important since both offices were vacant and no indoor source was present. Average $PN_{<1}$ concentration during no indoor sources periods was 3,080 cm^{-3} and 2,813 cm^{-3} for PR and B1 respectively, indicating lower concentration in B1 but without any significant difference. Therefore, sub-micron particles were either originated from transport indoors or penetrated from outdoors depending on the occupation scheme.

2.3.7 Black carbon

Table 2.6a summarizes statistical indicators for black carbon in PR and B1, where, open hours (08:00-21:00) values are compared with the corresponding closed hours (21:00-08:00) values. In general, BC levels in both offices maintained low concentrations with no significant difference between OH and CH. Both averaged and mean BC concentration indoors was considerably lower compared to other studies where mean indoor BC concentration was usually above 1 $\mu g/m^3$ (Viana et al. 2011; Wang et al. 2013; Reche et al. 2015; Tunno et al. 2015). Averaged BC during OH and CH in PR was almost equal (0.24 and 0.25 $\mu g/m^3$ respectively), whereas, in B1 BC was slightly higher during OH (0.38 $\mu g/m^3$) compared to CH (0.32 $\mu g/m^3$). The values also indicate higher BC concentrations in B1 compared to PR during the sampling period.

Table 2.6: a) Statistical indicators for black carbon ($\mu g/m^3$) in PR and B1. Comparison between open hours (OH) and closed hours (CH). b) Correlation between black carbon and PM_1, $PM_{2.5}$ and PM_{10} for PR.

a)	PR		B1	
	OH	CH	OH	CH
mean ± SD	0.24 ±0.06	0.25 ± 0.03	0.38 ± 0.15	0.32 ± 0.09
min	0.08	0.13	0.14	0.19
max	0.38	0.34	0.87	0.67
median	0.25	0.25	0.30	0.30
b)	PM_1	$PM_{2.5}$		PM_{10}
R^2	0.52	0.48		0.38

The low indoor BC concentrations both for OH and CH strongly suggest the absence of a direct impact from indoor sources. Accordingly, the results demonstrate that black carbon was not directly influenced by emission from printers. Similar observation is reported in Betha et al. (2011), in measurements in a printing

centre. Instead, BC concentration in both offices is likely influenced by outdoor levels. Indoor/outdoor relation of black carbon is well noted in other studies (LaRosa et al. 2002; Viana et al. 2011; Reche et al. 2015). In the present case, daily variations in the two offices are believed to originate from outdoor fluctuations. Black carbon is a component of fine particles and is closely related with PM concentrations. Table 2.6b verifies that BC is a major component of fine particles with better correlation for PM_1 (R^2=0.56). Higher correlation for fine particles ($PM_{2.5}$) is also reported in Wang et al. (2013).

2.4 Conclusions

Particle number and mass concentrations were measured in several offices in two different countries (Norway, Greece). Both campaigns took place in buildings equipped with mechanical ventilation, however, different occupation scheme characterized each office. Indoor/outdoor concentrations were measured on-line in order to investigate the contribution from outdoors along with the impact from indoor sources. Accordingly, mechanical ventilation of the building in the Norway campaign prevented a considerable fraction of outdoor particles penetrate indoors through the successful capture from filters. Therefore, the I/O ratio maintained low values (< 0.5), indicating the absence of indoor sources as well. Two offices were selected, one permanently occupied during working hours and one unoccupied at all times. The results indicated that indoor particle number/mass concentrations in both offices were highly influenced by the outdoor environment outside working hours, where both offices were vacant. On the contrary, during working hours human presence played an essential role on particle concentrations especially for coarse particles. Elevated concentrations for larger particles were directly associated with resuspension activities during working hours.

On the other hand, mechanical ventilation of the building in the Greece campaign was turned off during measurements. In this case, four offices were selected one of them corresponding to a printer room. Indoor particle number concentration was highly influenced by cleaning activities, however, in terms of long exposure the main impact to the indoor environment originated from the operation of the printers. Ultrafine particles indoors were substantially affected by printer emissions and had considerable impact to indoor particle number and mass concentrations in all measured offices due to particle transport indoors. Mass concentrations were also influenced by the physical presence of the occupants (in the occupied offices) due to particle resuspension of coarse particles but at lower extend compared to the impact from printer emissions. Nevertheless, during the periods where the offices were unoccupied the outdoor environment became the main contribution to indoors through particle infiltration, which is in agreement with the Norway campaign.

In summary, the present results demonstrate that particle number and mass concentrations were influenced by both indoor and outdoor sources depending on occupation scheme, indoor conditions and building characteristics.

Chapter 3

Modeling of particle infiltration characteristics

3.1 Introduction

In naturally ventilated buildings, where no mechanical ventilation system is present, the outdoor air is infiltrated indoors and thus influences indoor air quality. Infiltration is induced by natural convection, whilst it is achieved through cracks or leaks in the building envelope (Tian et al. 2009; Lai et al. 2012). Accordingly, outdoor pollutants and particulate matter (PM) can be easily transported indoors although indoor conditions have strong impact on the fate of the transported pollutants and PM.

The present chapter models particle infiltration from outdoors, where particle dynamics determine penetration characteristics. The under study building corresponds to the Baroque Library Hall (BLH) in Prague, Czech Republic, whilst the measurements were conducted by the Institute of Chemical Process Fundamentals (ICPF). The BLH is a naturally ventilated building, which, along with the controlled access from the visitors, provided a sampling site appropriate for determining the infiltration of outdoor originated particles and investigation of the visitor's impact on indoor PM. The objective was to evaluate particulate matter characteristics indoors with respect to outdoors, to estimate penetration of outdoor particles and deposition rates indoors using a dynamic mass balance model, to determine the infiltration factor and its dependence on particle size and finally to investigate the contribution of the visitors to the indoor particle concentration.

3.2 Measurement site/Instrumentation

The Baroque Library Hall of the National Library is part of Clementinum Historical Complex and is located in the Vltava River valley, right in the historical center of Prague. Clementinum, built on an area of 2 hectares, is the second largest and the most historic complex of buildings in Prague. The Hall, situated in the center of the Clementinum on the second floor, holds approximately 20.000 theological books dating from the 16th century until recent times and stored in original wooden shelves.

Figure 3.1 presents the internal scheme of the library. It is 39 m long and 9.4 m wide with an arched ceiling in the lowest point at 8.3 m and in the highest point 9.5 m high. There are 8 double glass windows covered by curtains along the western and eastern side and 4 entrance doors, 2 on the north side and 2 on the south side. The doors on the north side lead from the hallway, which serves as a storage room and as entrance used by librarians and restorers. The doors on the south side lead from foyer of the Hall and serve as an entrance and exit for the visitors. The library is naturally ventilated with all windows closed, while, the doors open only for visiting purposes. The visitors enter the Hall in groups of maximum 25 people with the guide and run only along the south site of the Hall. Sightseeing tours took place every day from 10 am and started every half-hour during weekend and every hour during the rest of week. Any other activities (e.g. cleaning) in the indoor environment were very limited.

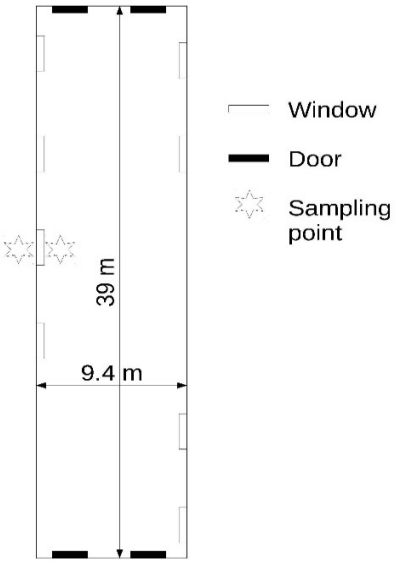

Figure 3.1: Scheme of the library and position of the instruments.

Three sampling campaigns were conducted during spring (10th - 17th March), summer (14th - 21th July) and winter (22th November - 2nd December) 2009. Indoor and outdoor particle number concentrations were measured by a Scanning Mobility Particle Sizer (SMPS, model 3934C, TSI, U.S.A.) consisted of a Differential Mobility Analyzer (DMA, model 3081), a Condensation Particle Counter (CPS, model 3775) and an Aerodynamic Particle Sizer (APS, model 3320, TSI, U.S.A.). Both instruments sampled from both inside and outside BLH simultaneously using its own sampling train provided with an electrically actuated three-way ball valve connected to a common programmable controller that used a CPC voltage (controlling the high voltage on the central rod of the DMA) as a signal for switching. The SMPS sampled with a flow rate at 0.3 l/min, measuring particle number concentration in the size range of 0.014-0.7 µm in 110 channels. The APS was operated with 5 l/min flow rate and measured particles in the effective size range 0.7-20 µm in 51 channels. The SMPS used 3 min upward scan, followed by one minute downward scan with

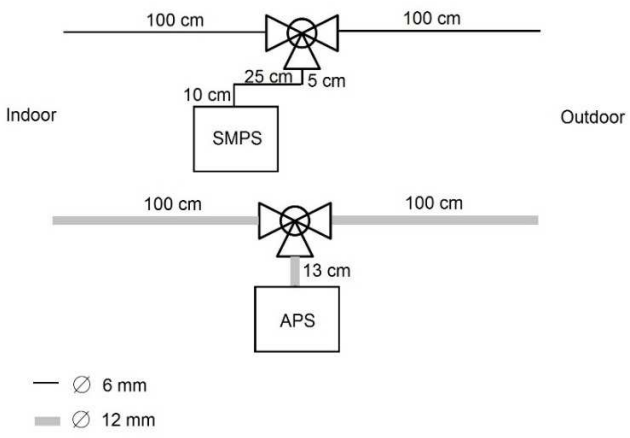

Figure 3.2: Experimental set up of the instruments.

one minute delay necessary to separate samples and wash sampling train after valve switching. Eventually two five-minute sampling cycles for indoor sampling followed by two five-minute cycles for outdoor sampling. The experimental set up of the instruments is shown in Figure 3.2. Data from both instruments were collected using Aerosol Instrument Manager software (AIM v.1.0, TSI, U.S.A.), where particle losses inside sampling trains were incorporated. In addition temperature, relative humidity and CO_2 concentration were measured by Indoor Air Quality Monitor PS32 (Sensotron, Poland).

3.3 Mass balance model

The indoor particle concentration for a well-mixed air volume can be described using a dynamic mass balance model:

$$\frac{dC_{in}}{dt} = PaC_{out} - aC_{in} - kC_{in} + \frac{S}{V} \quad (3.1)$$

where, C_{in} is the indoor particle concentration (cm^{-3}), C_{out} is the outdoor particle concentration (cm^{-3}), P is the penetration efficiency, a is the air exchange rate (h^{-1}), k is the deposition rate (h^{-1}), S is the emission rate of particles (h^{-1}), V is volume of the area under study (cm^{-3}), and t is the time (h). Equation (3.1) assumes that the indoor particle concentration is a result of particle penetration from outdoors, deposition on indoor surfaces, air exchange from indoors to outdoors and emissions from indoor sources. Condensation and coagulation of indoor particles were considered negligible. Spatial variability of the air inside the library was investigated and the results indicated that the well-mixed assumption was reasonable.

Indoor particle concentration can be determined using Equation (3.1) for a given time period. For each time step of the specified period, the indoor concentration was estimated using a numerical backward difference:

$$C_{in}(t) = \alpha PC_{out}(t-1)dt + [1-(a+k)dt]C_{in}(t-1) + \frac{S}{V}dt \quad (3.2)$$

Under the condition where no sources are present indoors the last term of the above equation can be neglected, and Equation (3.2) is transformed into:

$$C_{in}(t) = \alpha P C_{out}(t-1)dt + [1-(a+k)dt]C_{in}(t-1) \quad (3.3)$$

Hence, Equation (3.3) can be used to estimate indoor concentration by selecting the appropriate values for deposition and penetration, when the air exchange rate and the outdoor concentration are known. Both variables (k and P) depend substantially on particle size and characteristics of the building envelope. Moreover, considering steady state conditions inside the building and no presence of indoor sources Equation (3.1) yields the infiltration factor:

$$F_{inf} = \frac{C_{in}}{C_{out}} = \frac{aP}{a+k} \quad (3.4)$$

The infiltration factor, F_{inf}, is a function of air exchange rate $\boldsymbol{a}$, penetration efficiency $\boldsymbol{P}$, and deposition rate $\boldsymbol{k}$. Therefore, F_{inf} is dimensionless and represents the fraction of particles that penetrate from outdoors and remains suspended indoors. Equation (3.4) also demonstrates that the infiltration factor is equivalent with the I/O ratio under steady state conditions.

3.4 Estimation of air exchange rate

Measurements of CO_2 concentration inside the library revealed periodical increase and decrease of CO_2 levels indoors. The concentrations started to grow daily at the beginning of the visiting hours, reached maximum at the end of the visiting hours and followed by a gradual decrease to the original values. The increase resulted from carbon dioxide exhaled by visitors (Varas-Muriel et al. 2014) and the decrease from air exchange between indoors and outdoors.

Air exchange rate of the library was estimated from the decay in CO_2 concentration during night-time. CO_2 concentration followed an exponential decay with time by (Congrong et al. 2004):

$$a = \frac{1}{t-t_0}\ln\left(\frac{C-C_{out}}{C_0-C_{out}}\right) \quad (3.5)$$

where, a is the air exchange rate (h^{-1}), t and t_0 are the end and beginning of the decay curve (h^{-1}), respectively, C and C_0 are the CO_2 concentrations (ppm) measured at times t and t_0, respectively and C_{out}

(ppm) is the outdoor concentration at time t. The air exchange rates, estimated for all three campaigns are given in Table 3.1.

Seasonal variation in air exchange rate indicates different ventilation of the library through the building envelope for different seasons. In naturally ventilated buildings, the airflow is driven by temperature or pressure differences (D'Agostino and Congedo 2014). It is likely that the variation of the ventilation inside the Baroque Library Hall is driven by temperature differences (López-Aparicio et al. 2011). Table 3.1 also provides the average indoor/outdoor temperature during visiting and non-visiting hours. The numbers strongly suggest that the temperature inside the library depends on outdoor conditions.

Table 3.1: a) Estimated air exchange rates for each sampling period and b) average (± SD) temperature inside and outside the library for visiting and non-visiting hours for the three seasons.

a)		Spring	Summer	Winter
Air exchange rate (h^{-1})		0.13	0.11	0.15
b)	Temperature			
Indoor	Visiting hours	13.4 (± 0.6)	24.1 (± 0.3)	13.2 (± 1.6)
	Non-visiting hours	13.0 (± 0.5)	24.0 (± 0.3)	13.3 (± 0.5)
Outdoor	Visiting hours	8.4 (± 1.7)	23.9 (± 4.6)	9.2 (± 3.1)
	Non-visiting hours	6.7 (± 1.6)	19.5 (± 3.7)	8.2 (± 2.8)

3.5 Indoor and outdoor particle concentration

Table 3.2 compares the particle number concentration at different size fractions for all three seasons. The SMPS data were separated into two size fractions, where, the first one includes the particles between 0.014-0.1 μm (nucleation fraction) and the second one includes particles between 0.10-0.71 μm (accumulation fraction). On the other hand, the APS data were separated to the fine fraction corresponding to particles in the size range of 0.7-3 μm and to the coarse fraction corresponding to particles at the size range of 3-20 μm.

Higher outdoor concentration observed in all three seasons and for all size fractions. The numbers indicate higher outdoor concentration by one order of magnitude than the indoor number concentration. Table 3.2 also suggests that submicron particles (0.014-0.1 μm, 0.1-71 μm) present higher ambient concentration both indoors and outdoors, than particles at higher fractions (0.7-3 μm, 3-20 μm) with bigger contribution from nucleation fraction. Additionally, particle number concentration for sizes > 3 μm

was negligible both indoors and outdoors. Similar characteristic was found in a study at Plantin-Moretus museum in Antwerp, Belgium (Krupińska et al. 2013).

Table 3.2: Indoor and outdoor particle number concentration (cm^{-3}) for the three seasons. Comparison between the average (±SD) concentrations at different size fractions.

	0.014-0.1 µm	0.10-0.71 µm	0.7-3 µm	3-20 µm
a) Spring				
Indoor	1,616 ± 526	686 ± 253	3.5 ± 2.2	0.005 ± 0.004
Outdoor	3,950 ± 2,152	1,180 ± 774	12.4 ± 10.2	0.07 ± 0.06
b) Summer				
Indoor	1,565 ± 549	817 ± 333	0.8 ± 0.2	0.01 ± 0.009
Outdoor	5,079 ± 3,444	1,299 ± 940	2.2 ± 1.2	0.07 ± 0.05
c) Winter				
Indoor	1,653 ± 713	955 ± 534	4.0 ±3.1	0.009 ± 0.008
Outdoor	3,948 ± 2,431	1,541 ± 1,122	10.1 ± 9.3	0.08 ± 0.06

Moreover, it was found that during several periods the indoor particle concentration is highly affected by the outdoor one. Figure 3.3 presents such a period, where, the indoor and outdoor particle concentrations are plotted during a 4-days period in winter season.

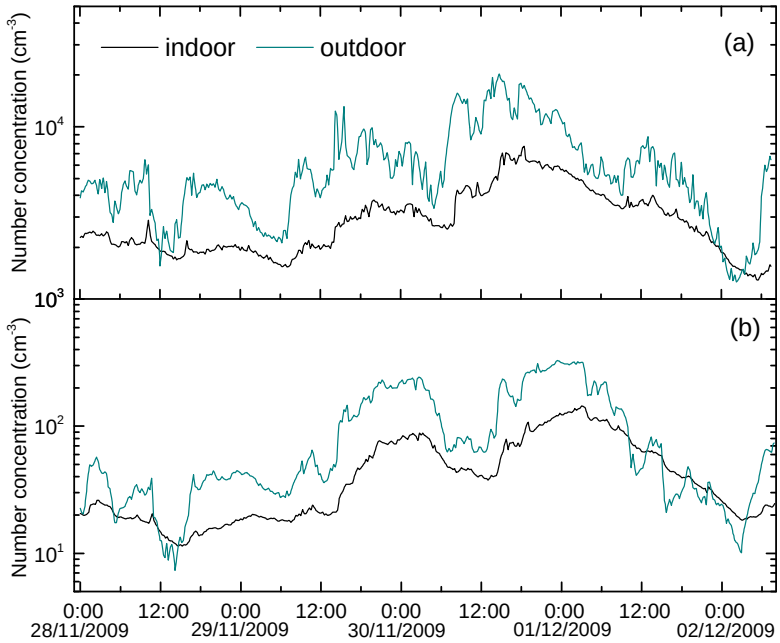

Figure 3.3: Total indoor and outdoor number concentration of particles in the size range: a) 0.014 - 0.71 µm and b) 0.7 - 20 µm during 28/11/2009-02/12/2009 in winter period.

Figure 3.3 demonstrates that the temporal fluctuations of outdoor concentration contribute significantly to the indoor ones resulting in a considerable increase of indoor particle concentration for both low (0.014-0.71 μm) and high (0.7-20 μm) particle sizes. Similar periods, where the temporal fluctuations of outdoor concentration affected the indoor concentration found in all three seasons, underlying that the particulate matter inside the library is strongly affected by outdoor conditions. Indoor-outdoor relationship of ambient PM is reported in several museum environments (Brimblecombe et al .1999; Camuffo et al. 2001; Gysels et al. 2004; Hu et al. 2009; Worobiec et al. 2010; Worobiec et al. 2010).

3.6 Indoor/Outdoor Ratio

In general, I/O ratio maintained values lower than 0.7, indicating that there was no significant indoor source (Figure 3.4). Although, Figure 3.3 suggests that the indoor concentration is considerably influenced by the outdoor, the relatively low I/O ratio (< 0.7) underlay that the building envelope obstructs a significant fraction of outdoor particles penetrate indoors.

Figure 3.4 also indicates that the I/O ratio depends strongly on particle size. Higher ratios (0.4-0.7) observed in the accumulation fraction (0.1-0.7 μm) for all three seasons suggest that particle infiltration is more effective at this size range. Lower ratios obtained mainly for ultrafine (0.014-0.1 μm) and coarse (1-20 μm) particles. Diffusion due to Brownian motion for ultrafine particles and gravitational settling for coarse particles can explain the lower ratios at these size fractions (Hinds 1999). Similar dependence of I/O ratio with particle size can be found in Long et al. (2001), Bennett and Koutrakis (2006) and Thornburg et al. (2001). Additionally, averaged higher ratio of ultrafine particles (0.38) compared to coarse particles (0.27) suggests that particles at the size range of 0.014-0.1 μm penetrate easier through cracks and leaks inside the library. On the other hand, coarse particles are more effectively removed due to their size (Nazaroff 2004).

No seasonal variation of I/O ratio observed, since Figure 3.4 indicates similar ratios through the different seasons. However, it is worth to note the decreased I/O ratio for ultrafine particles (0.014-0.1 μm) during summer and increased for coarse particles (1-20 μm) in respect to spring and winter season. It is possible that ultrafine particles present slightly higher values during spring and winter due to higher exchange rate, whereas, the effect from the presence of people in summer season contributes to higher I/O ratios for coarse particles in this season.

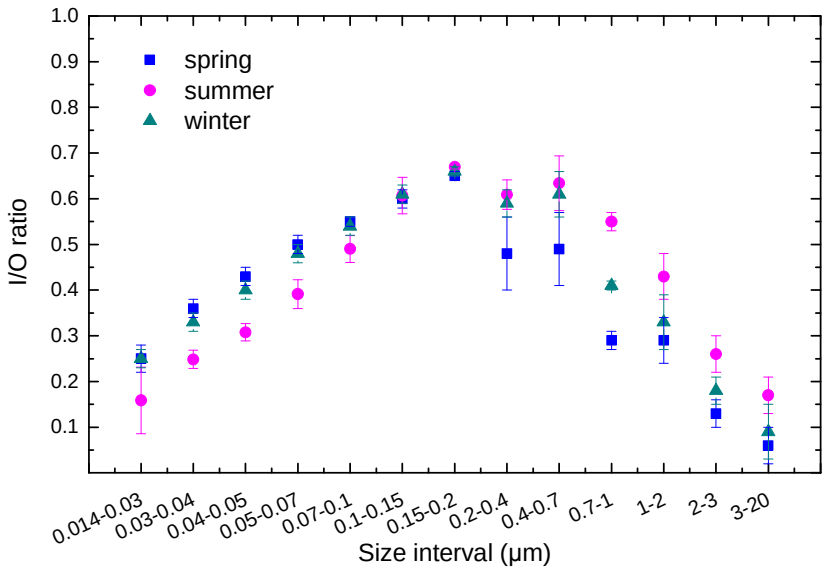

Figure 3.4: Averaged I/O ratio versus particle size for the three seasons. Error bars represent standard deviation.

3.7 Modeling of the indoor particle concentration

3.7.1 Methodology for estimating deposition rate and penetration efficiency

Indoor particle concentration was modelled for different size intervals using Equation (3.3). Since, the air exchange rate of the library was estimated by CO_2 measurements, the only requirements in Equation (3.3) is to find the appropriate values for deposition rate ***k*** and penetration efficiency ***P*** using the continuous outdoor particle concentration.

Particle number concentration in the range 0.014-0.7 µm was evaluated using 9 size intervals, whereas, particle number concentration between 0.7-20 µm was evaluated using 4 size intervals. Particle size distribution above 3 µm was not divided into smaller size intervals because indoor number concentration above 5 µm was usually close to zero. In total 13 discrete size intervals were used to cover the full size range of the measured size distribution. The deposition rate and penetration efficiency were evaluated in each size interval for all three seasons, thus, 3 possible values for each variable in order to obtain an independent result. Valid values for P were considered inside the range $0 < P < 1$, whereas, k was evaluated for positive values. In order to diminish the possible acceptable values for deposition, a lower limit was used based on the air exchange rate of each season. The lower limit was obtained considering an initial value, which, corresponds to the lowest positive number of the same order of magnitude for each air

exchange rate (e.g. for air exchange rate 0.0022 min^{-1} the initial value was selected at 0.0001 min^{-1}). The above method was used in Equation (3.3) in order to ensure that the deposition rate retains mathematically significant value. The time step used in Equation (3.3) was selected the same with the time interval used in the measurement, thus, 5 minutes. Hence, the deposition rate was originally obtained in units min^{-1} and the modelled values were exactly same in number as the measured data. The model was running each time for a selected value of k and for the full range of P. The time step for penetration was chosen 0.01, whereas, for deposition 0.0005 min^{-1} (or 0.03 hr^{-1}).

The aim was to find the best fit between the measured indoor concentration and the obtained modelled indoor concentration. This was succeeded by finding the pair of values (k, P) that generate the best fitted curve. For this purpose, coefficient of determination (R^2) was used as a criterion. Nevertheless, in many cases more than one pair of k and P resulted in nearly equal values of R^2. The same problem is reported in Bennett and Koutrakis 2006, Rim et al. 2010. The methodology followed to overcome this problem was to find one pair that generates a curve with the highest R^2 value. Then, the highest value of R^2 was selected, and only the R^2 values higher than the 95% of the best generated R^2 were considered valid. Any pair of k and P corresponding to a valid R^2 was selected to determine the averaged k and P for each size interval. Thus, the final deposition and penetration was obtained from several valid pairs of k and P.

The above method resulted in one unique value of R^2 with highest correlation for every tested deposition rate in the range of the penetration efficiency (0.01-0.99). Plotting every one of these R^2 values with deposition, we obtain a U-shaped curve similar to the one Bennett and Koutrakis (2006) found (Figure 3.5a). The U-shaped curve suggests that there was always one R^2 value, which gave the best correlation between the measured and the modelled concentration but also indicates the presence of other almost equal values. Thus, highlights the non-unique solution of k and P and reflects the variability of the results with all possibly acceptable values. Furthermore, using the P value that corresponds to the previously found R^2 we obtain a proportional relationship between k and P. Figure 3.5b plots the k and P pairs for two selected size intervals (0.014 - 0.03 μm, 0.03 - 0.04 μm) for the three seasons. The values of P in each case represent the best correlation (R^2) for each deposition rate in each size interval. It is demonstrated that k and P not only depend proportionally but are characterized by a linear relationship. The same characteristic found in all cases for all three seasons. Hence, it is highlighted that the two model parameters are not independent, rather than, when deposition increases (higher settling) model formulation requires an increased penetration efficiency (higher fraction of outdoor particles penetrate indoors) in order to find the best fit between the measured and the modelled concentration.

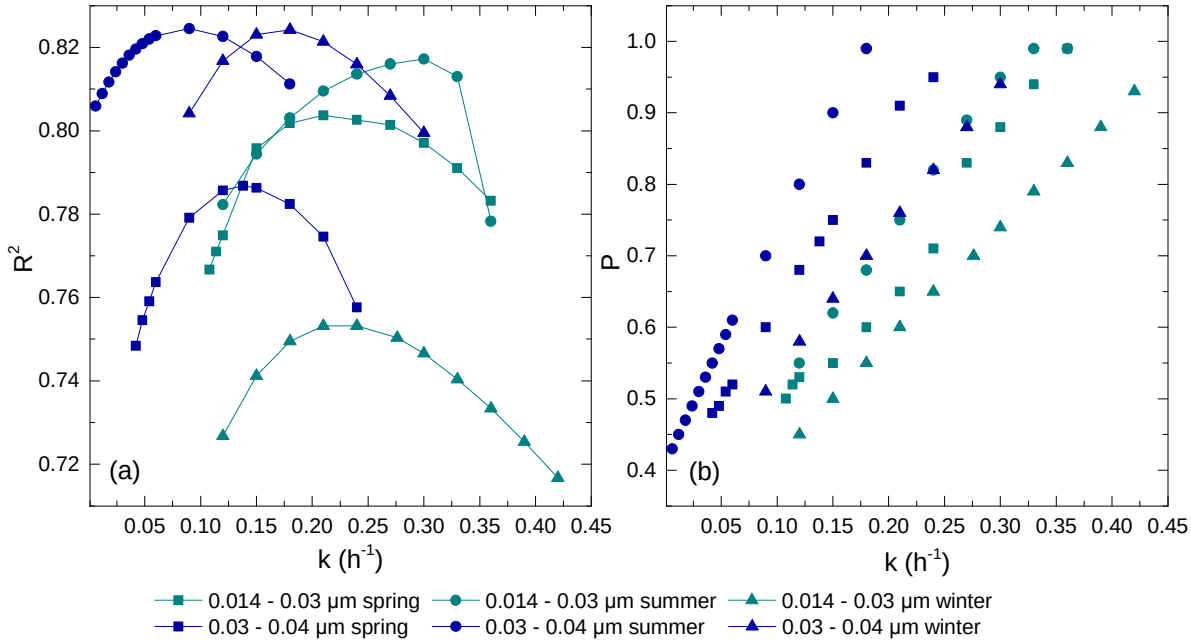

Figure 3.5: a) Highest generated R^2 for each deposition rate at two selected size intervals (0.014 - 0.03 μm, 0.03 - 0.04 μm), b) Penetration efficiency (that corresponds to highest R^2) versus deposition rate for the same selected size intervals.

Moreover, in order to avoid the influence of the starting point, any local maximum of the indoor concentration at the beginning of the dataset was neglected. Such a local maximum was found at the beginning of winter, where, the data from the first 20 hours were excluded from the calculations. Additionally, in summer season it was generally observed that the modelled values presented a significant underestimation of indoor concentration only at the end of the dataset. Hence, it was concluded that the starting point (which presented remarkably high indoor concentration compared to the rest of the data) influences the results and the data were modelled at different starting points. No underestimation of indoor concentration was obtained when the starting point was located at the middle of the data set (18/07/2009). All subsequent calculations were computed using the previously found starting point.

Measured data and modelled concentration were in general in good agreement. High R^2 values were usually found (> 0.7) with good correlation between the compared values. Figure 3.6 provides, as an example, a comparison between the measured indoor concentration and the modelled one for two size intervals in each season. It can be seen that a simple mass balance model accounting particle infiltration, exchange rate with the outdoor environment and deposition losses is suitable enough to reproduce the

observed concentration. High correlation (R^2) suggests good agreement between the measured data and the modelled values.

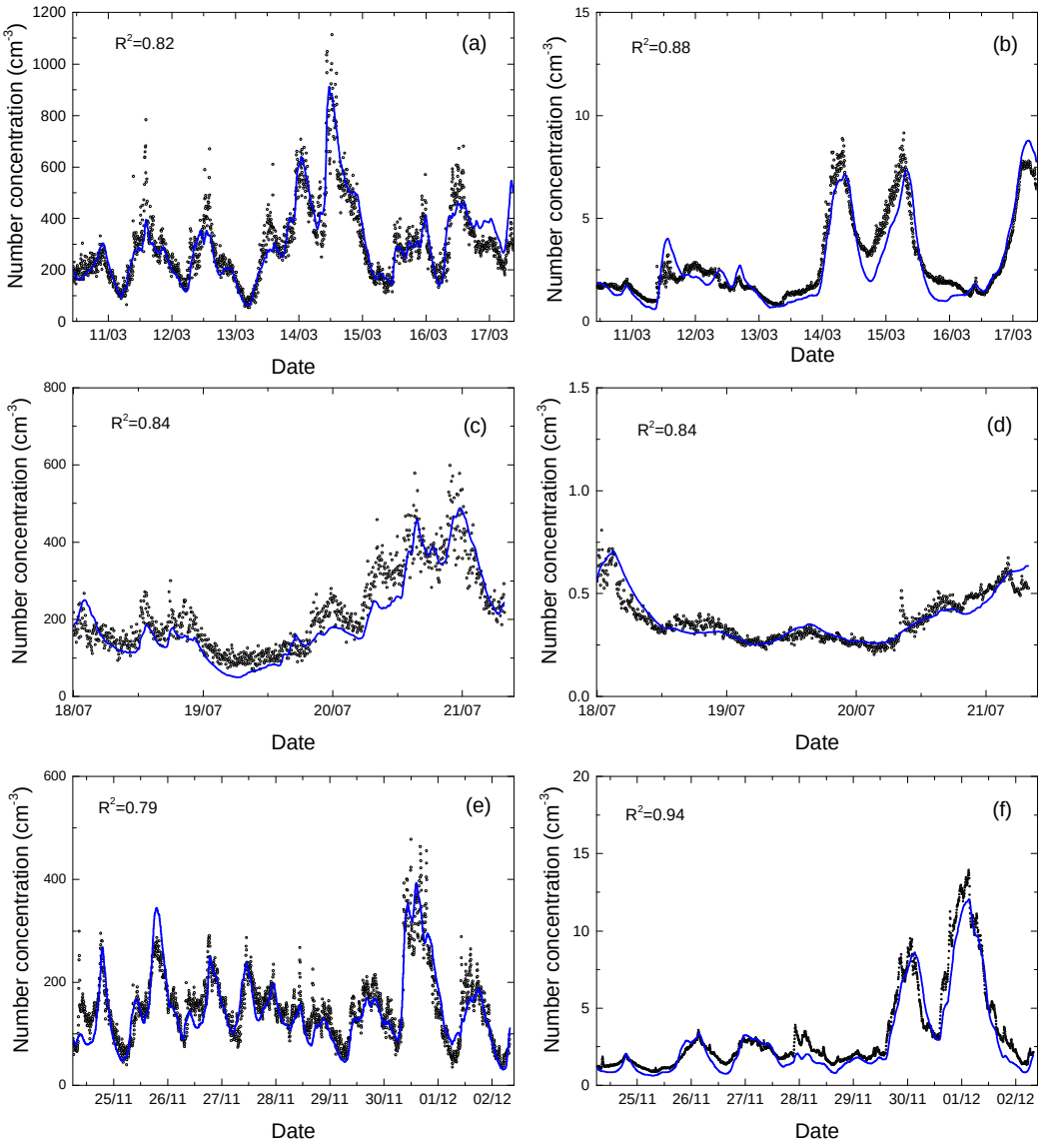

Figure 3.6: Comparison between measured indoor concentration (○) and modelled indoor concentration (–) using the best fitted values of k and P for two size intervals (0.014-0.1 µm, 0.7-1 µm) and all three season. Plots a, c and e correspond to particles at the size range 0.014-0.1 µm for spring, summer and winter respectively. Plots b, d and f correspond to particles at the size range 0.7-1 µm for spring, summer and winter respectively. The pairs of k and P are taken from Table 3.3. The correlation (R^2) between the measured data and modelled values is also presented.

In some cases, however, the model could not achieve high levels of confidence, although, the generated curve was similar to the profile of the indoor concentration. The low R^2 was mainly due to strong fluctuations of indoor and outdoor concentration and was observed mainly during summer season. However, the estimated k and P were not excluded in order to compare it with averaged I/O ratio.

Finally, in the size interval 3-20 μm the correlation between the measured data and the modelled values was substantially lower than the other tested size intervals. It was found that the model failed to generate several peaks of indoor particle concentration. Although, the indoor concentration of coarse particles at the size interval 3-20 μm was negligible in all three seasons, it was assumed that this fraction of particles is mostly affected by the presence of visitors inside the library. The influence of visitors on the indoor concentration at coarse particle fraction in museum environments can be found in literature (Worobiec et al. 2008; Worobiec et al. 2010; Ghedini et al. 2011; Godoi et al. 2013; Krupińska et al. 2013). Thus, in order to determine appropriate values of k and P for coarse particles, the indoor concentration was compared in parallel with the outdoor. Only time periods, where the indoor concentration followed similar temporal fluctuations as the outdoor, were investigated to obtain values for deposition and penetration. Originally, only the night data of each season were examined but no good correlation was found because the evaluation of only the night data resulted in shorter tested periods, which were not representative enough.

3.7.2 Averaged values of k and P

Table 3.3 lists the deposition rate k and penetration efficiency P in each size interval for the 3 seasons. The deposition rate varied substantially with particle size. The highest rates were obtained for particle size 3-20 μm (1.04, 0.70 and 1.09 h^{-1} for spring, summer and winter respectively). Higher particle size is associated with higher deposition rates due to strong gravitational settling that characterizes coarse particles. A similar trend but with lower rates was observed for ultrafine particles. High deposition rates (0.22-0.27 h^{-1}) were obtained for nucleation fraction 0.014-0.03 μm in all three seasons caused mainly by Brownian diffusion. On the other hand, deposition for particles at accumulation fraction (0.1-0.7 μm) preserved nearly the same values (0.02-0.03 h^{-1} in spring, 0.006-0.009 h^{-1} in summer and 0.04 h^{-1} in winter). The above findings are in agreement with studies (Thatcher and Layton 1995; Abt et al. 2000; Liu and Nazaroff 2001; Long et al. 2001; Crongrong et al. 2005; Bennett and Koutrakis 2006; Rim et al. 2010; Rim et al. 2013; El Orch et al. 2014) where deposition was found to depend considerably on particle size. The values also indicate nearly similar rates for the three seasons.

Table 3.3: Estimated values of deposition and penetration and area-averaged deposition velocity, $\overline{V_d}$. The values represent the average and standard deviation (mean ± SD) of k and P in each size interval.

Size interval (µm)	k (h^{-1})	P	$\overline{V_d}$ (m/s) ($\cdot 10^{-5}$)
		Spring	
0.014 - 0.03	0.22 ± 0.09	0.75 ± 0.15	6.04
0.03 - 0.04	0.12 ± 0.07	0.74 ± 0.15	3.29
0.04 - 0.05	0.05 ± 0.04	0.69 ± 0.15	1.37
0.05 - 0.07	0.03 ± 0.02	0.63 ± 0.08	0.82
0.07 - 0.1	0.03 ± 0.02	0.68 ± 0.08	0.82
0.1 - 0.15	0.02 ± 0.01	0.68 ± 0.06	0.55
0.15 - 0.2	0.02 ± 0.01	0.72 ± 0.05	0.55
0.2 - 0.4	0.03 ± 0.02	0.65 ± 0.07	0.82
0.4 - 0.7	0.03 ± 0.02	0.58 ± 0.08	0.82
0.7 - 1	0.15 ± 0.10	0.60 ± 0.17	4.12
1 - 2	0.11 ± 0.07	0.54 ± 0.14	3.02
2 - 3	0.35 ± 0.15	0.51 ± 0.15	9.61
3 - 20	1.04 ± 0.39	0.46 ± 0.13	28.58
		Summer	
0.014 - 0.03	0.24 ± 0.08	0.77 ± 0.13	6.60
0.03 - 0.04	0.06 ± 0.05	0.70 ± 0.17	1.65
0.04 - 0.05	0.04 ± 0.02	0.65 ± 0.11	1.10
0.05 - 0.07	0.03 ± 0.02	0.70 ± 0.09	0.82
0.07 - 0.1	0.03 ± 0.02	0.82 ± 0.09	0.82
0.1 - 0.15	0.009 ± 0.004	0.80 ± 0.03	0.02
0.15 - 0.2	0.009 ± 0.004	0.83 ± 0.02	0.02
0.2 - 0.4	0.006*	0.76 ± 0.02	0.02
0.4 - 0.7	0.006*	0.76 ± 0.03	0.02
0.7 - 1	0.03 ± 0.01	0.69 ± 0.07	0.82
1 - 2	0.06 ± 0.05	0.76 ± 0.15	1.65
2 - 3	0.08 ± 0.04	0.48 ± 0.07	2.20
3 - 20	0.70 ± 0.07	0.70 ± 0.06	19.24
		Winter	
0.014 - 0.03	0.27 ± 0.10	0.69 ± 0.15	7.42
0.03 - 0.04	0.20 ± 0.07	0.74 ± 0.15	5.50
0.04 - 0.05	0.11 ± 0.07	0.73 ± 0.15	3.02
0.05 - 0.07	0.05 ± 0.04	0.72 ± 0.15	1.37
0.07 - 0.1	0.05 ± 0.03	0.75 ± 0.14	1.37
0.1 - 0.15	0.04 ± 0.02	0.77 ± 0.13	1.10
0.15 - 0.2	0.04 ± 0.02	0.79 ± 0.11	1.10
0.2 - 0.4	0.04 ± 0.02	0.77 ± 0.13	1.10
0.4 - 0.7	0.04 ± 0.02	0.74 ± 0.13	1.10
0.7 - 1	0.15 ± 0.08	0.73 ± 0.16	4.12
1 - 2	0.17 ± 0.09	0.71 ± 0.17	4.67
2 - 3	0.41 ± 0.17	0.67 ± 0.19	11.27
3 - 20	1.09 ± 0.27	0.76 ± 0.14	29.95

* no standard deviation. Deposition determined only from one value of k.

Although, deposition was found to depend on particle size, penetration efficiency, on the other hand, was not clearly related with particle size. High penetration (0.6 - 0.8) was found in most size intervals. The numbers suggest that outdoor particles penetrate easily inside the library independent of the particle size. High penetration (0.8-0.9) in ultrafine particles is also reported in literature (Chen and Zhao 2011; Long et al. 2001) but coarse particles are usually characterized with lower penetration factors due to their size, which, prevents them from entering the building (Diapouli et al. 2013). Although, such a trend is observed in spring season, penetration during summer (0.70) and winter (0.76) seasons retained high estimates at coarse particles. Higher estimates of penetration efficiency than expected (in particle sizes > 1 μm) are reported in Thatcher and Layton (1995) and Vette et al. (2001). It is likely that high penetration is due to the building envelope. Experiments conducted in laboratories associated the increased values with higher pressure difference or larger crack height (Chen and Zhao 2011). Additionally, geometry of the cracks has been found to considerably affect penetration factors (Chen et al. 2012). A possible reason since the library corresponds to an old construction. Figure 3.7 presents a comparison of the averaged k and P with literature values from corresponding in real environments.

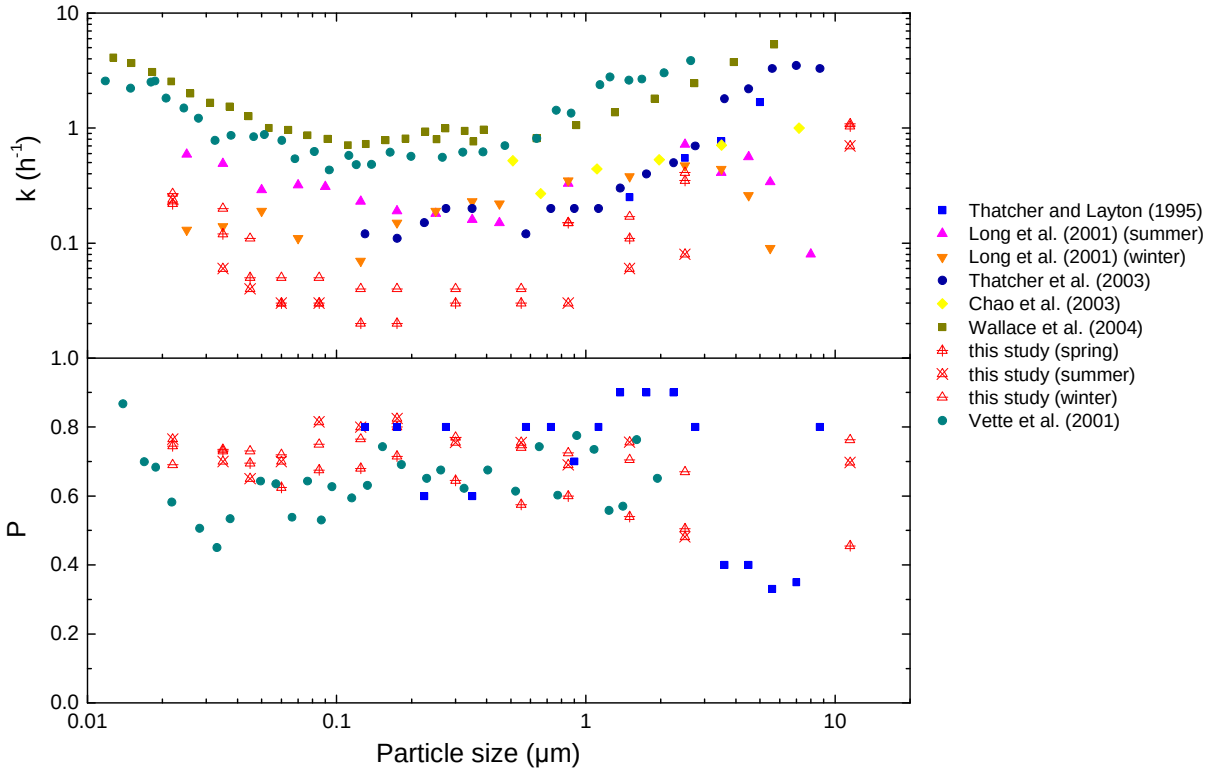

Figure 3.7: Comparison between averaged deposition rate and penetration efficiency with studies from literature conducted in real environments.

In general, the present estimates are comparable with literature values. However, it is observed that deposition for accumulation fraction (0.1-0.7 μm) presents the lowest rates than literature values. Different characteristics of the indoor environments (volume, airflow turbulence, surface texture roughness, mixing mechanisms) influence the results considerably (Lai 2002). An easy way to interpret and compare the results is to introduce the area-averaged deposition velocity (Table 3.3). Using the relation $\overline{V_d} = k(V/\Sigma S)$ (Lai 2002), where $\overline{V_d}$ is the area-averaged deposition velocity, V represents the volume of the library (m^3) and S the surface area (m^2). The surface area was determined including all books and shelves and surface to volume ratio was found at 1.01 m^{-1}. Thus, the deposition rate k was transformed into the area-averaged deposition velocity $\overline{V_d}$. Likewise higher velocities were obtained for ultrafine and coarse particles. Table 3.3 suggests that deposition velocity inside the library ranged between 10^{-6}-10^{-4} m/s, which is in full agreement with literature values (10^{-6}-10^{-3} m/s, Lai 2002).

3.8 Infiltration factor and comparison with I/O ratio

The infiltration factor for each size interval was calculated using deposition and penetration values provided in Table 3.3 and the corresponding air exchange rate for each season (Table 3.1). Evaluation of the estimated k and P was achieved comparing infiltration factor with I/O ratio. Figure 3.8 compares the infiltration factor with I/O ratio at each size interval for the three seasons. It should be noted that in the case of coarse fraction (3-20 μm) the I/O ratio presented in Figure 3.8 corresponds to the calculated I/O ratio from the number concentration data of the selected periods, used to determine k and P at this size range.

Infiltration factor was equal to I/O ratio in most cases. Figure 3.9 plots the infiltration factor versus I/O ratio for all size intervals and seasons. Good agreement with I/O ratio ensures that the averaged k and P represent at a high confidence level the particle deposition rate and penetration efficiency in each size interval. By extend it also confirms the selection of the starting point in summer data and the selected periods that were used in 3-20 μm size interval to determine k and P for coarse particles.

The infiltration factor ranged between 0.24-0.76 for particles in the size range 0.014-0.7 μm, whereas, in the size range 0.7-20 μm F_{inf} ranged between 0.05-0.56. Since, F_{inf} represents the fraction of particles that reaches the indoor environment from outdoors and remains suspended, it indicates that infiltration of ultrafine particles is higher compared to coarse particles and that enrichment of ultrafine particles inside the library was caused by penetration from outdoors. It also confirms that particle dynamics (deposition,

penetration) depend on particle size. Similar dependence of F_{inf} with particle size was found in Bennett and Koutrakis (2006), Rim et al. (2010), El Orch et al. (2014).

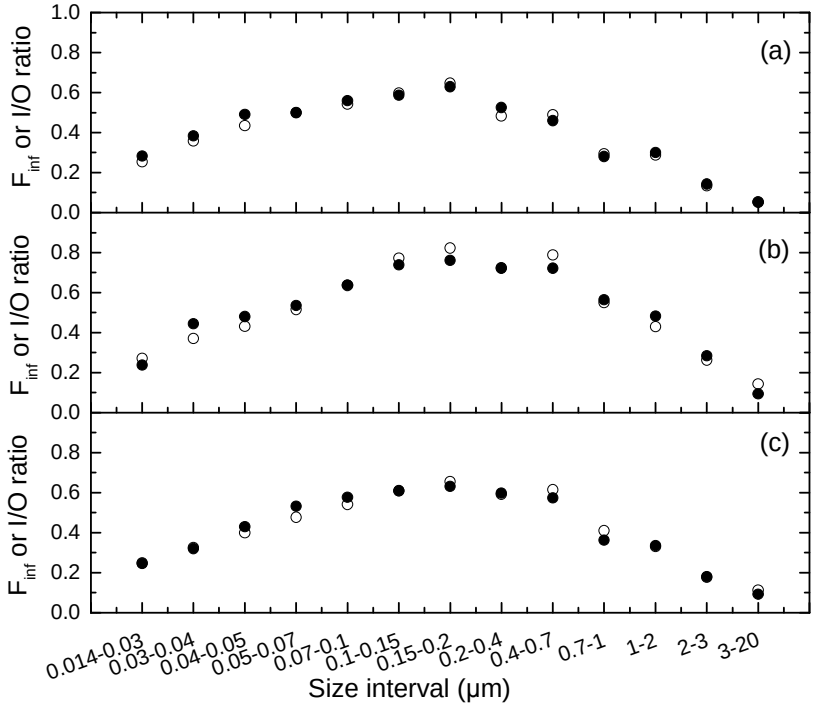

Figure 3.8: Comparison between infiltration factor (●) and I/O ratio (○) in each size interval for a) spring, b) summer and c) winter seasons.

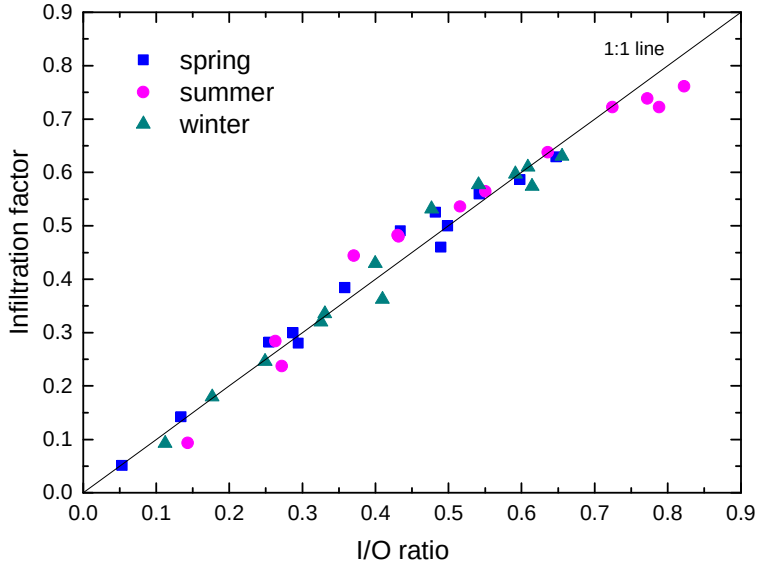

Figure 3.9: Infiltration factor versus I/O ratio for all size intervals for the three seasons.

3.9 Influence from indoor sources

Periodical increase and decrease of indoor particle concentration that could not be modelled, was found in the size range between 3-20 μm in all three seasons. Figure 3.10 presents the indoor number concentration of coarse particles for spring season. A comparison with modelled concentration is also shown. Although, modelled concentration successfully represents the indoor concentration at periods outside the visiting hours, there are several temporal indoor fluctuations that the model could not generate. These temporal fluctuations were associated with the presence of visitors inside the library, since all of them were located during visiting hours. Indoor concentration of coarse particles may be elevated for different reasons: transport of dust from outside, resuspension of the deposited particles on the floor, fabric fibers or material emissions. Studies that relate the increased indoor concentration at coarse fraction with human presence during the visiting hours can be found in literature (Camuffo et al. 1999; Camuffo et al. 2001; Hu et al. 2009; Krupińska et al. 2013).

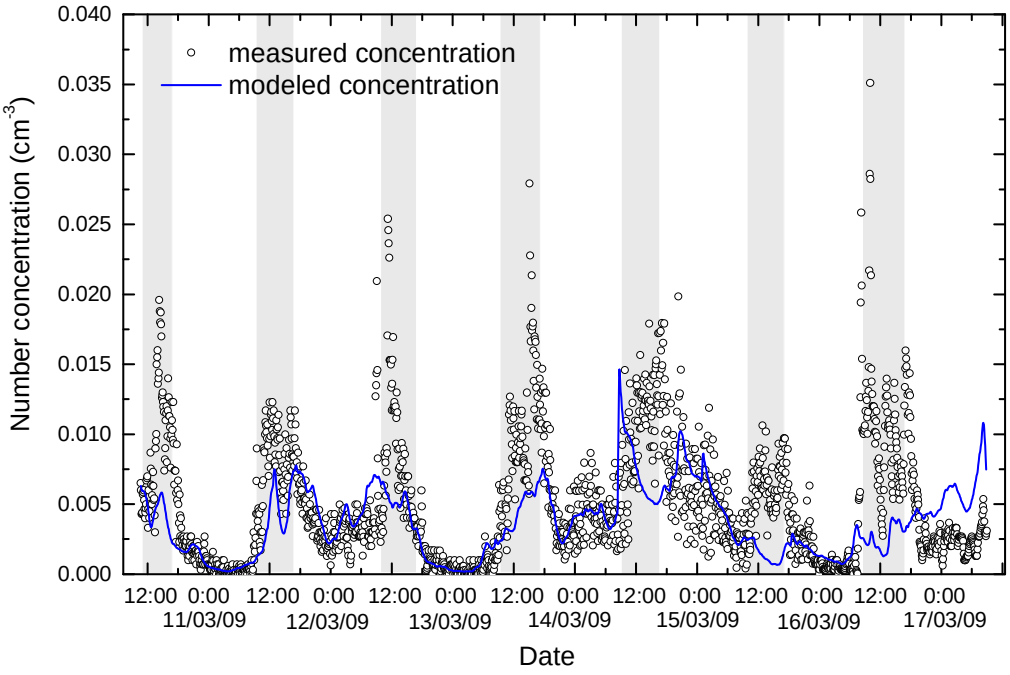

Figure 3.10: Comparison of indoor measured concentration with modelled concentration of coarse particles (3-20 μm) in spring season. Colored areas represent visiting hours (10:00-17:00).

However, a significant deviation of the modelled concentration from the measured data outside the visiting hours was observed at the end of the season (16/07/09 19:00 until the end). This deviation was

due to the averaged procedure that was used to derive the averaged values for k and P. In particular, evaluation of the model at this period (16/07/09 19:00 until the end) provided with lower values of P. Thus, modeling the indoor concentration of coarse particles during spring with the averaged P, resulted in higher modelled values than the measured at the end of season. A limitation due to the evaluation of the indoor number concentration of coarse particles in selected time periods.

Figure 3.11 presents a comparison of I/O ratios between visiting and non-visiting hours. It is demonstrated that I/O ratios maintain higher values during visiting hours for all three seasons. Moreover, it is observed that higher I/O characterizes summer, which is directly associated with more people visiting the library and longer visiting hours at this season. The 50th percentile in summer was 0.24, whereas, for spring and winter season the 50th percentile was 0.11 and 0.14 respectively.

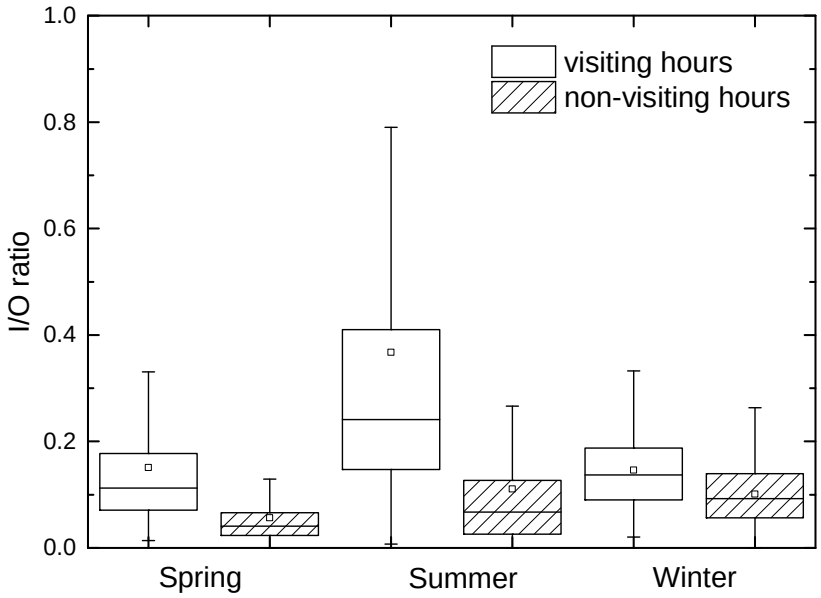

Figure 3.11: Comparison of I/O ratio of coarse particles (3-20 μm) for visiting and non-visiting hours. The box plots represent the 25th and the 75th percentile values, mean value and the horizontal line the median (50th percentile) value. Outliers are excluded.

In addition, the periods during visiting hours were isolated and compared with periods of non-visiting hours. Table 3.4 presents the concentration of coarse particles during visiting and non-visiting hours for all three seasons. Indeed, during visiting hours the indoor concentration of coarse particles increased by a factor of 3, 3.2 and 2 for spring, summer and winter respectively, suggesting that human presence influences substantially indoor concentration at this size range (3-20 μm).

Table 3.4: Averaged number concentration of indoor coarse particles (3-20 μm) during visiting and non-visiting hours.

	Number concentration (cm^{-3})		
	Visiting hours	Non-visiting hours	Increase factor
Spring (10:00-17:00)	0.009	0.003	3
Summer (10:00-20:00)	0.016	0.005	3.2
Winter (10:00-16:00)	0.014	0.007	2

3.10 Conclusions

Particle number concentration was measured inside a naturally ventilated building during different seasons (spring, summer, winter). It was found that indoor concentration was substantially influenced by outdoor fluctuations in all three periods. No seasonal variation of I/O ratio between the same particle size suggests similar behavior in terms of particle dynamics and building characteristics. A mass balance model was used to evaluate the contribution from outdoors assuming no indoor sources, were the deposition rate and penetration efficiency were evaluated at each size interval for the three seasons.

The present method provided several valid pairs of deposition and penetration at each size interval, suggesting that there is no unique solution and highlighting the variability of k and P. Each size interval was examined separately and averaged values of k and P were finally used to determine infiltration factor. The infiltration factor was in good agreement with I/O ratio ensuring the well-estimated values for deposition and penetration at each size interval. It was also evident that F_{inf} was size dependent with less effective removal at accumulation fraction. Therefore, indoor concentration was dominated by ultrafine particles, which were associated with penetration from outdoors due to higher infiltration factor. Coarse particles, on the other hand, were associated with human presence due to low confidence level between modelled and measured concentration. In addition, the contribution of the visitors was examined separately, where higher I/O ratio and indoor concentration during visiting hours confirmed the influence from indoor sources.

Chapter 4
Particle resuspension rate in the indoor environment induced by human walking

4.1 Introduction

Indoor sources usually involve human-associated activities that emit particles in the indoor environment. Common activities such as printing, painting, cooking, burning wood, burning candles and smoking generate new particles in the indoor environment (Hussein et al. 2006; Ott et al. 2006). However, particles in the indoor air are not only the result of newly formed particles, but arising also from the resuspension of the already existing particles, such as settled dust on indoor surfaces.

Particle resuspension is a physical process where particles are detached from a surface when an external force acts on them. Hence, any human activity indoors can cause particle resuspension (moving objects, walking, dusting) with the most common being vacuuming and walking (Corsi et al. 2008; Qian et al. 2008). The objective of this chapter is to evaluate particle resuspension induced by human walking. The experiments were conducted by the personnel of the Atmospheric Aerosols Laboratory of the School of Environmental Engineering. The impact from human walking is investigated under different dust loadings. Accordingly, the effect of different dust loadings on the floor to the indoor particle concentration and the resuspension rate is investigated along with the impact of different walking patterns.

4.2 Laboratory experiments

4.2.1 Layout and instrumentation

The resuspension experiments were performed in the Atmospheric Aerosols Laboratory in the School of Environmental Engineering in the Technical University of Crete. The laboratory is of rectangular shape of 18.5 m^2 area and 53.7 m^3 volume with one door and one window placed opposite of the door. The effective volume was estimated at 77 % of the total volume. In total 20 walking experiments were conducted in a period of 3 months using a “paper pool” (4.3 m × 1.4 m × 1.1 m). The paper pool was built inside the

laboratory and was made of plotter paper (0.94 m width, ρ = 80 g/m^2) and a masking paper tape. Both particle number and mass concentrations were measured during the resuspension experiments. Particle number concentration was measured in the size range of 0.02 – 1 µm using a P-Trak (Ultrafine Particle Counter, Model 8525, TSI), while, mass concentration was measured in the range 0.1 – 10 µm using a Dust Trak (Aerosol Monitor, Model 8520, TSI). P-Trak uses high-purity isopropyl alcohol to grow microscopic particles for easier detection and counting in the optical chamber. Its concentration range is between 0 – 5×10^5 particles/cm^3 with a sample air flow rate of 0.1 lpm. On the other hand, the measurement principle of the Dust Trak is based on a 90° light scattering at a flow rate 1.7 lpm with a concentration range 1 – 100,000 µg/m^3. The log interval was set up to 1 minute.

Indoor air temperature and relative humidity during the resuspension measurements were recorded by four Tiny Tag data loggers placed in the corners of the laboratory. The average air temperature in the laboratory during the measurement periods was 30 ± 1 °C and the relative humidity 45 ± 4 %. In addition, the IAQ instrument (Indoor Air Quality Meter, Model 8762, TSI) was used to measure CO_2 levels (ppm) in order to obtain the air exchange rate of the laboratory.

All instruments were placed around the paper pool with inlets 1.38 ± 0.03 m above the ground corresponding to the breathing zone of the person performing the walking activity. The internal layout and instrumentation is presented in Figure 4.1.

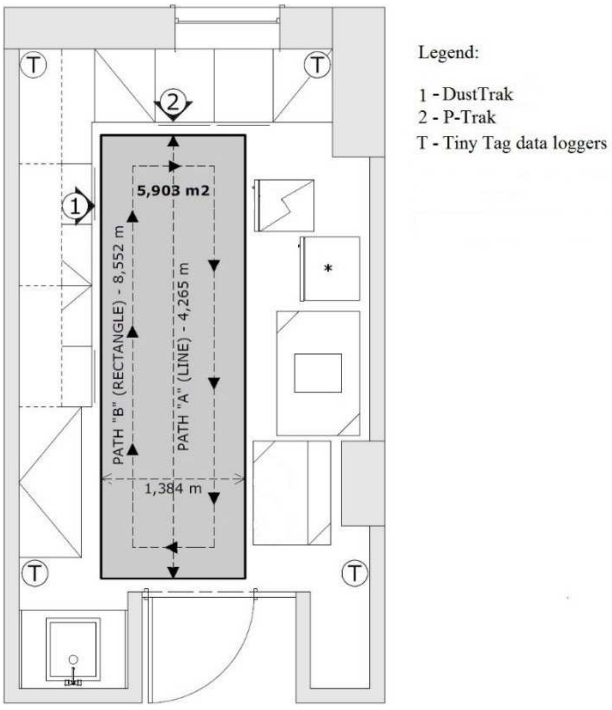

Figure 4.1: Internal layout of the laboratory and position of the instruments.

Finally, the PM_{10} mass concentration data obtained by Dust Trak were corrected according to Chalvatzaki et al. (2010), where comparative measurements of PM_{10} concentrations by the Beta attenuation monitor (FH 62 SEQ) and the Dust Trak were performed at an urban background site close to the laboratory for a period of 12 months. The correction equation is expressed as:

$$\text{Beta conc. } [\mu g/m^3] = 0.80 \times \text{Dust Trak conc. } [\mu g/m^3] + 10.4$$

4.2.2 Measurement protocol

The walking activity was performed in a line or in a rectangular path as it is seen in Figure 4.1. Path A corresponds to a line path, where the person walked for 4.3 m long in the middle of the paper pool and path B corresponds to a rectangle shaped path of 8.6 m long around the edge of the paper pool in a clockwise direction. Both the window and the door were closed during all experiments.

Four different dust loadings were tested during the experiments (1, 5, 15, 25 g/m^2). The dust loading was collected from the area around the laboratory. It is the same dust that could possible get inside the indoor environment during air exchange while opening the window or by penetration. The collected dust was then sieved on a laboratory sieve with an aperture of 53 μm and stored in an air-tight box at a room temperature in the laboratory. With the same sieve the dust was spread manually on the floor of the paper pool with extreme care in order to maintain a uniform layer. The dust was spread at 0.15 ± 0.05 m height above the ground at the most 4 - 5 hours before the measurements.

Each resuspension experiment (20 experiments in total) lasted 5 hours and 30 minutes and was completed in 3 stages:

Stage 1:	Empty laboratory:	0 - 60 min (background measurement)
Stage 2:	Walking period:	60 - 80 min (resuspension - emission period)
Stage 3:	Post walking period:	80 - 330 min (post-activity period - particle removal)

During stages 1 and 3 no person was present in the room, whereas, during stage 2 only one person was present in the room. The data obtained from stage 2 (emission period-20 minutes), were used to determine the resuspension rate since it was the only period of activity inside the laboratory room. However, only the last 10 minutes of background period and the first 210 minutes of the removal period used to evaluate the background and the removal period respectively. Hence, 4 hours in total for each experiment. The background period was evaluated only at the last 10 minutes, since, no significant temporal fluctuations of the indoor concentration observed during the pre-activity period. The removal period was evaluated only for the first 210 min because the indoor concentration maintained similar values after the chosen period.

Four resuspension experiments were conducted with increased/decreased walking speed in order to investigate the effect of walking speed on resuspension rate. Two experiments were performed with 20%

higher walking speed, whereas, two experiments were performed with 20% lower walking speed. All four experiments were conducted following a line path and only in the case of 5 g/m^2 and 1 g/m^2 dust loading.

4.3 Estimation of the resuspension rate

4.3.1 Resuspension rate model

The resuspension of indoor particles is usually defined by the resuspension rate *r (min^{-1})*, which is the fraction of particles removed from the surface per unit of time (Nicholson 1988):

$$r = \frac{R}{L} \tag{4.1}$$

where *R* is the resuspension flux *(μg/m^{2}min)* and *L (μg/m^2)* is the particle surface concentration. Considering a room of well-mixed air volume, particle concentration can be described by a dynamic mass balance model (Chen and Zhao 2011):

$$\frac{d(VC_{in})}{dt} = aPVC_{out} + S - aVC_{in} - kVC_{in} \tag{4.2}$$

where C_{in} is the particle concentration inside the laboratory *(μg/m^3)*, C_{out} is the particle concentration outside the laboratory *(μg/m^3)*, *V* is the effective volume of the laboratory *(m^3)*, *P* is the penetration efficiency, *a* is the air exchange rate *(min^{-1})*, *k* is the deposition rate *(min^{-1})*, *S* is the emission rate of the particles indoors *(μg/min)* and *t* is the time *(min^{-1})*. In particular, in respect to particle emissions by resuspension - *S*, the emission rate can be written as:

$$S = rA_rL \tag{4.3}$$

where *r* is the resuspension rate *(min^{-1})*, A_r is the floor surface area used for resuspension *(m^2)* and *L* is the floor loading *(μg/m^2)*. Thus, Equation (4.2) can be rewritten as follows:

$$V\frac{dC_{in}}{dt} = aPVC_{out} + rA_rL - (a+k)VC_{in} \tag{4.4}$$

Introducing a mass balance model on the surface, the change in particle mass concentration on the floor can be written as (Qian and Ferro 2008):

$$A\frac{dL}{dt} = -rA_rL + kVC_{in} \tag{4.5}$$

where *A* is the total surface area of the room *(m²)*. Thus, the change in particle concentration indoors is described by a set of two equations, namely Equations (4.4) and (4.5).
During the resuspension experiments, the total surface area of the laboratory was used. In this case, A_r can be substituted with *A*, and a simplified version of the system of Equations (4.4) and (4.5) yields:

$$V\frac{dC_{in}}{dt} = aPVC_{out} + rAL - (a+k)VC_{in} \tag{4.6}$$

$$A\frac{dL}{dt} = -rAL + kVC_{in} \tag{4.7}$$

The Equation (4.6) describes the change in mass concentration indoors and Equation (4.7) describes the change in particle mass concentration on the floor. The resuspension rate *r* is estimated by Equation (4.6) using a forward difference approximation, while, Equation (4.7) can be solved analytically. Thus, the resuspension rate and the particle surface loading for each time step are given by:

$$r(t+dt) = \frac{V}{AL(t)}\left[\frac{C_{in}(t+dt) - C_{in}(t)}{dt} + (k+a)C_{in}(t) - aPC_{out}(t)\right] \tag{4.8}$$

$$L(t) = \frac{kVC_{in}(t)}{rA}(1 - e^{-rt}) + L(0)e^{-rt} \tag{4.9}$$

The requirements for solving the above system are the initial values of mass loading *L(0)* and the change in concentration *C(t)* with time. Given the initial mass loading *L(0)* and the change of particle concentration, *r* can be estimated for time step one using Equation (4.8). Since *r* is known, Equation (4.9) is then used to estimate the surface loading at the first time step, *L(1)*. The same procedure is followed for every time step.
Moreover, the particle concentration in the indoor air can be predicted from Equation (4.6) (Qian et al. 2008):

$$C_{in}(t+dt) = r\frac{A}{V}L(t)dt + C_{in}(t)[1-(a+k)dt] + aPC_{out}(t)dt \quad (4.10)$$

The first term on the right side of the Equation (4.10) is the resuspension contribution to indoor air concentration, the second term refers to the reduction of indoor concentration by deposition and air exchange rate and finally the third term is the penetration of outdoor originated particles indoors.

4.3.2 Infiltration rate

The infiltration rate of outdoor originated particles can be estimated using Equation (4.6) for a period without any activity inside the laboratory. Thus, Equation (4.6) is written as:

$$V\frac{dC_{in}}{dt} = aPVC_{out} - (a+k)VC_{in} \quad (4.11)$$

The analytical solution of the above equation is:

$$C_{in}(t) = \frac{aPC_{out}}{a+k} + \left[C_{in}(0) - \frac{aPC_{out}}{a+k}\right]e^{-(a+k)t} \quad (4.12)$$

The right hand side of Equation (4.12) consists of two terms. The first term is the steady state concentration of the particles inside the laboratory which can be defined as the fraction of particles that penetrates from outdoors and remain suspended indoors. The second term represents the total losses of the indoor aerosol due to deposition and air exchange from indoors to outdoors.

The infiltration rate was calculated based on Equation (4.12) after the end of the activity, where, the particle concentration is exponentially decreasing with time. Due to lack of outdoor data, infiltration was estimated as the fraction of particles that remain suspended inside the laboratory (the steady state particle concentration or infiltration concentration C_{inf}):

$$C_{inf} = \frac{aPC_{out}}{a+k} \quad (4.13)$$

4.3.3 Air exchange rate

The air exchange rate was estimated based on the exponential decay of CO_2 inside the laboratory. The concentration of CO_2 after the emission period is described by the following equation:

$$\frac{dC_{CO_2}}{dt} = aC_{CO_2} \tag{4.14}$$

where *a* is air exchange rate *(hr^{-1})*. Thus, CO_2 concentration at any time inside the laboratory is given by:

$$C_{CO_2}(t) = C_{CO_2}(0)e^{-at} \tag{4.15}$$

The average air exchange of the laboratory was calculated at 0.16 hr^{-1} during the experiments.

4.4 Indoor particle number and mass concentrations

Indoor particle number and mass concentrations were measured simultaneously during the walking experiment. Particle number concentration was measured in the size range of 0.02 - 1 μm, whereas, the measured mass concentration corresponded to the size range of 0.1 - 10 μm.

Figure 4.2 presents the indoor mass and number concentration versus time during the experiment on 04/07/2013. The mass concentration was influenced from the beginning of the activity with an increase in the indoor concentration which is followed by a decreasing period after the end of the walking activity. The background average indoor mass concentration was 73 μg/m^3, while, during the walking activity the average mass concentration was 3,320 μg/m^3. On the other hand, the number concentration maintained similar concentration levels before and during the walking activity. Average background concentration was 2,037 particles/cm^3, whereas, average concentration during the activity was 2,110 particles/cm^3. The same characteristic found in all experiments. Thus, the three periods (background, walking period, post-walking period) were strongly correlated only with the indoor particle mass concentration.

Particle resuspension from indoor surfaces depends on particle size (Wang et al. 2012; Boor et al. 2013a). Larger particles detach more easily from the surface (Hinds 1999; Boor et al. 2013a). Previous studies verify that small particles (< 1 μm) are not easily resuspended or not resuspended at all (Thatcher and Layton 1995; Tian et al. 2014; Lazaridis et al. 1998). Moreover, studies on resuspension by human walking

concluded that resuspension rate increases with particle size (Qian and Ferro 2008; Qian et al. 2008; Shaughnessy and Vu 2012).

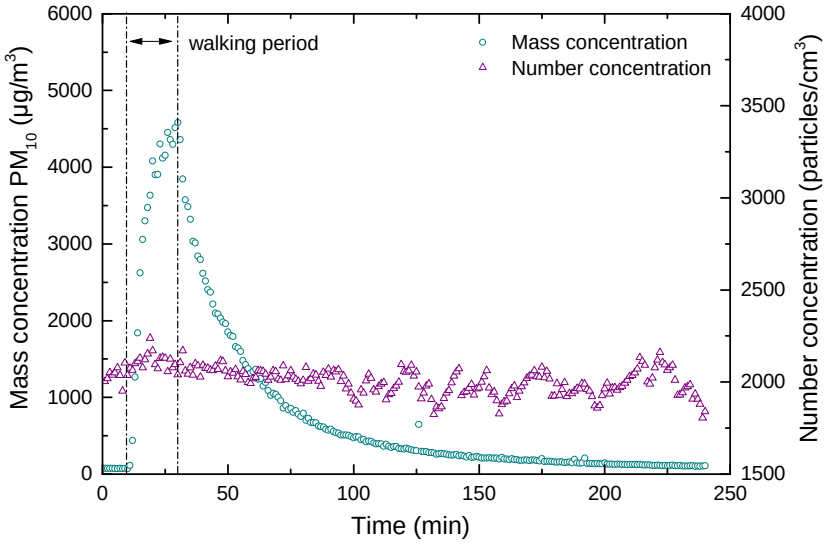

Figure 4.2: Mass and number concentration versus time during walking in rectangle shape inside the paper pool with dust loading 25 g/m^2 (R2 on 04/07/2013, Table 4.1).

The present results indicate that in terms of mass concentration the walking activity influences strongly the PM_{10} indoor particle concentration. On the other hand, in terms of number concentration indoor particles are not affected by the activity in the laboratory room inside the measured particle size range. Considering the different size range used for the mass and number concentration, the present results imply that the resuspension of indoor particles takes place at particle sizes higher than 1 µm. It is likely that particles at size that corresponds to the measured number concentration (0.02 - 1 µm) is not resuspend at all. Since, the measured size range of the mass concentration corresponds to higher particle sizes (0.1 - 10 µm), it is believed that the resuspended particulate matter lies in the size range of 1 - 10 µm. Table 4.1 summarizes the average PM_{10} concentration for background and activity periods during all experiments. The numbers indicate a considerable change in indoor mass concentration inside the laboratory. Indoor mass concentration was increased by one or two orders of magnitude in a period of few minutes (20 minutes). On the other hand, particle number concentration maintained values close to the background level in all experiments as indicated in Figure 4.2.

Table 4.1: Comparison between average background concentration and average walking concentration for different dust loadings (R-Rectangular, L-Line path). The average emission rate for each experiment is also shown.

Experiment-Walking profile	PM_{10} average background concentration, $\mu g/m^3$	PM_{10} average walking period concentration, $\mu g/m^3$	Average emission rate, mg/min
Dust Loading, 25 g/m^2			
04/07-R	73	3,320	17.3
10/07-L	58	3,205	14.6
26/07-R	39	3,839	17.6
30/07-L	32	3,463	19.4
Average	51	3,457	17.2
Dust Loading, 15 g/m^2			
21/06-R	47	1,433	6.5
26/06-L	36	1,579	7.1
08/08-R	42	1,690	7.8
10/08-L	35	1,716	9.2
Average	40	1,605	7.7
Dust Loading, 5 g/m^2			
02/07-R	38	462	2.0
28/06-L	42	573	2.4
12/08-R	41	556	3.5
13/08-L	49	642	2.9
10/09-L	34	680	2.8
11/09-L	39	573	4.1
Average	41	581	3.0
Dust Loading, 1 g/m^2			
12/07-R	47	215	0.9
24/07-L	27	325	2.2
15/08-R	52	259	1.2
14/08-L	50	240	1.4
12/09-L	35	381	2.6
13/09-L	24	156	1.0
Average	39	263	1.6

No dependence of indoor PM_{10} concentration found in respect to the two different walking profiles followed during the activity. Walking in a rectangular shape or in line inside the laboratory had no effect on indoor particle concentration and therefore on the resuspension rate. Qian and Ferro (2008) examined the effect of different walking paces and weight of the person while walking inside a chamber and found that the main contribution in resuspension rate is walking style. In the present study walking style, time of walking, dust type, foot wear and walking person were the same in all experiments and the only variable during the activity was the walking pattern which had no effect on the indoor particle concentration.

4.5 Indoor PM_{10} mass concentration at different dust loadings

Figure 4.3 presents the PM_{10} indoor mass concentration versus time for different dust loadings. One experiment from each dust loading (thus 4 in total) was chosen in order to compare the indoor mass concentration and examine the effect of the dust loading to the measured PM_{10} mass concentration. All chosen experiments corresponded to walking in a line path in order to isolate the impact of using different dust loadings on the floor.

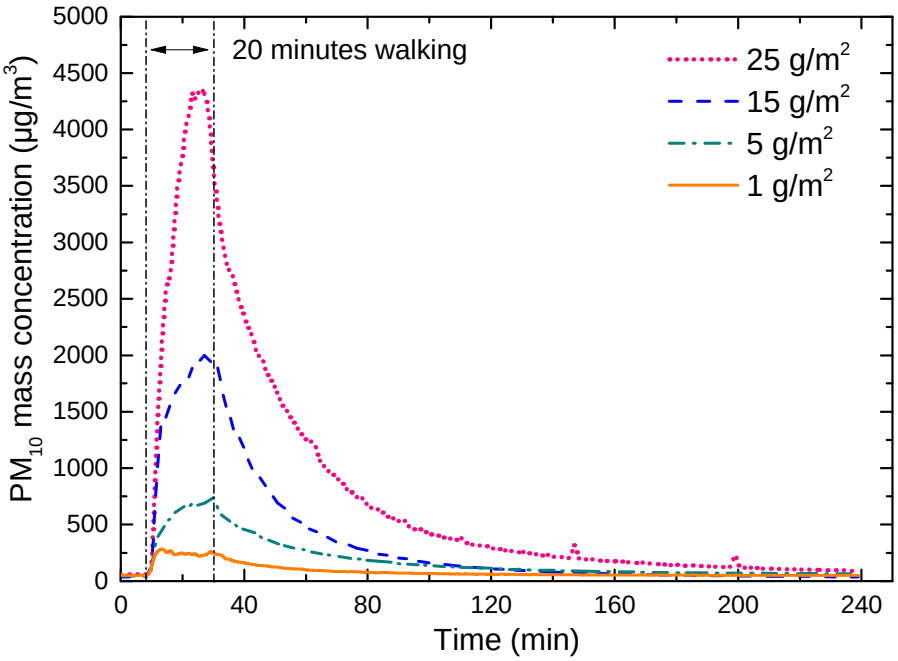

Figure 4.3: Mass concentration versus time for different dust loadings. Line path was used in all experiments (10/07, 26/06, 28/06, 14/08).

Higher surface loading leads to higher indoor mass concentration. Increased concentration on the floor corresponds to higher initial dust loading, which, can be potentially removed from the surface. In fact, calculating the emission rate *S* from Equation (4.3) for each surface loading reveals that the emission rate increases with increasing the initial dust loading on the floor (Table 4.1). The average emission rates for 25, 15, 5 and 1 gr/m^2 dust loading were 17.2, 7.7, 3.0 and 1.6 mg/min respectively. Gomes et al. (2007) also observed increased mass of resuspended particles at higher dust loadings and Tian et al. (2014) reported that higher dust emission rates were provoked by higher surface dust loadings. Moreover, Qian et al. (2014) reported that the emission rates of particle mass due to walking were in the range 10^{-2} - 10^{2} mg/min, which is in agreement with the present findings.

4.6 Estimation of infiltration rate

In the absence of indoor sources, the indoor particle concentration is the net result of particle penetration from outdoors, particle deposition on indoor surfaces and air exchange rate of the study room (Schneider et al. 1999; Thatcher et al. 2003; Rim et al. 2013). Thus, the total indoor particle losses include deposition by Brownian diffusion and gravitational settling (Nazaroff 2004) and the indoor/outdoor air exchange rate (Chen and Zhao 2011). Herein, the post-walking period was evaluated using the Equation (4.11), which reflects the indoor particle concentration inside the laboratory room in the case of no present indoor source. Applying Equation (4.12) to the experimental data after the end of the activity and using also Equation (4.13), the infiltration rate and total losses inside the laboratory were estimated. Table 4.2 lists the infiltration concentration C_{inf} and total losses for each experiment. In addition, Figure 4.4 presents a comparison between the measured PM_{10} mass concentration and the modelled one after the end of the walking period. The same pattern found in all experiments.

Table 4.2: Results of the modelled indoor concentrations after the end of the activity period.

Experiment	Dust loading, g/m^2	Initial concentration, C(0), $\mu g/m^3$	Steady state concentration, C_{inf}, $\mu g/m^3$	Total losses, a+k, hr^{-1}	R^2
04/07	25	4,582	95	2.60	0.97
10/07	25	4,026	63	2.35	0.97
21/06	15	2,024	48	2.39	0.99
26/06	15	3,932	48	2.91	0.97
02/07	5	658	39	2.25	0.98
28/06	5	757	59	2.36	0.94
12/07	1	255	46	1.91	0.98
24/07	1	286	25	2.90	0.95
26/07	25	4,226	48	3.46	0.98
30/07	25	3,920	44	3.04	0.97
08/08	15	1,997	38	3.24	0.98
10/08	15	1,884	43	3.00	0.98
12/08	5	621	36	2.78	0.97
13/08	5	736	46	3.27	0.94
15/08	1	274	62	3.00	0.99
14/08	1	272	48	2.91	0.95
10/09	5	802	31	2.65	0.98
11/09	5	747	33	4.20	0.91
12/09	1	444	27	2.69	0.98
13/09	1	186	26	3.13	0.97
		Average	46	2.85	0.98

The correlation between the modelled indoor concentration for the experiment R5 (Figure 4.4) and the observed one is high with R^2 = 0.98. It indicates that Equation (4.12) is well-describing the measured indoor particle concentration starting with the initial value of 255 μg/m^3 and ending at the steady state mass concentration of 46 μg/m^3 inside the laboratory. High correlation between the observed and the modelled indoor concentration found in all experiments with R^2 always above 0.9 (0.91-0.99).

C_{inf} was independent from the initial surface dust loading. According to Equation (4.13) the steady state indoor concentration is a function of penetration of outdoor particles and total losses inside the laboratory. Moreover, no correlation found between total losses *(a+k)* and the initial surface loading. On average, the total losses inside the laboratory were 2.85 ± 0.50 hr^{-1}.

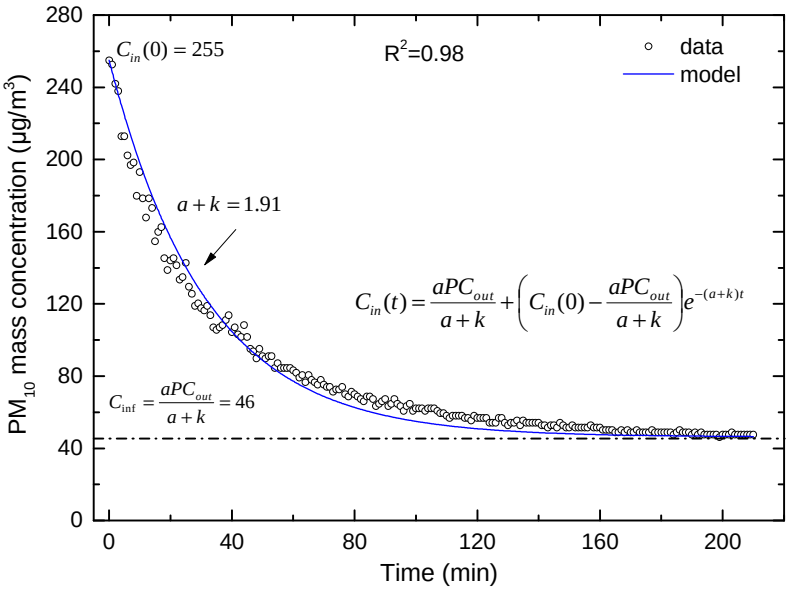

Figure 4.4: Observed mass concentration and modelled one after the end of the activity. Walking in rectangle shape inside the paper pool with dust loading 25 g/m^2 (R5 on 12/07/2013).

4.7 Dust loading

The resuspension rate and surface loading are irreversibly proportional (Equations (4.8) and (4.9)) and cannot be derived independently. An increase of indoor mass concentration increases the resuspension rate and reduces the dust loading on the floor. *L(t)* can be estimated only by knowing the resuspension rate at that specific moment. Giving the initial value *L(0)*, a repeated numerical procedure is followed by estimating at each time step the resuspension rate and then the instant dust loading on the floor.

A typical example of surface concentration variations during the activity period is shown in Figure 4.5. The initial dust loading on the floor was estimated at 24.57 g/m^2 and this value is compared with the calculated dust loading derived from Equation (4.9). The data points under the line -which shows the initial surface concentration- indicate an increase in indoor mass concentration, whereas, the data points above the line indicate a decrease in indoor mass concentration (various temporal fluctuations took place in most of the experiments). Numerically the first case is related with a positive number in the calculation of resuspension rate, while, the second case is related with a negative number. Moreover, the mass concentration on the floor shows small variations with modelled dust loading fluctuations varied between 24.5 – 24.6 g/m^2. Even though indoor PM_{10} concentration increases up to two orders of magnitude, the surface dust loading L(t) retains values close to the initial dust loading. The same behavior was observed in all experiments. The average variance of the relative fluctuations of the surface concentration was found 0.013%, confirming that a very small fraction of the deposited dust on the floor is actually resuspended. These findings are in agreement with Tian et al. (2014) where the authors also suggested that only a small fraction of particles is resuspended. Nevertheless, indoor PM_{10} concentration increases drastically with higher dust loading during the walking period resulting in higher mass concentration inside the laboratory. A reasonable explanation is that the higher the dust loading on the floor is, the higher is the potential fraction of the particles that can detach from the surface and consequently resuspend.

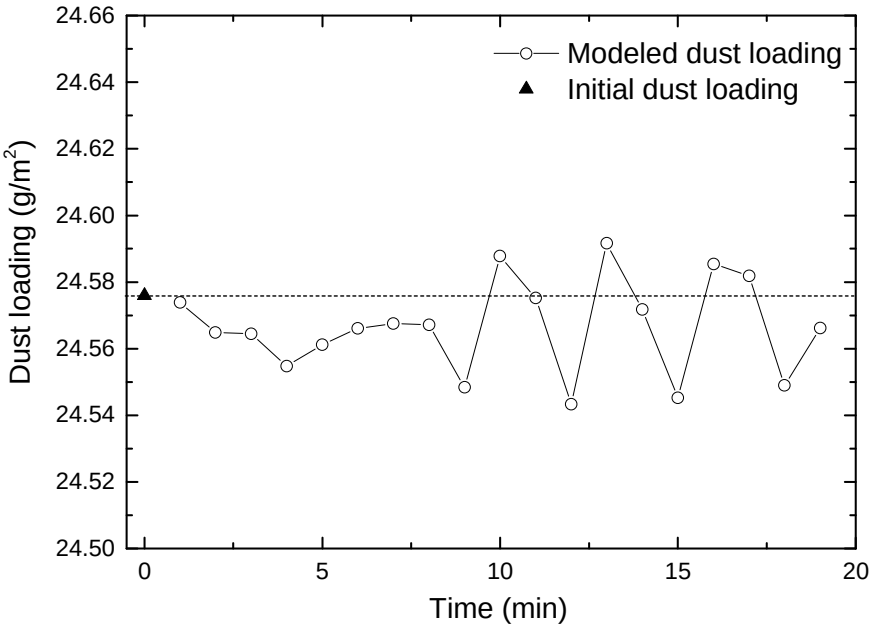

Figure 4.5: Initial dust loading on the floor and modelled dust loading versus time during the activity period, Lo= 24.57 g/m^2 (R2 on 04/07/2013).

Particle detachment is closely related with resuspension and it depends both on the adhesive and removal forces (Lazaridis et al. 1998; Ibrahim et al. 2003; Ibrahim et al. 2008; Zhang et al. 2008). Moreover, resuspension occurs easily for larger particles (Corsi et al. 2008; Qian and Ferro 2008; Rosati et al. 2008; Shaughnessy and Vu 2012; Boor et al. 2013a; Tian et al. 2014). In human induced particle resuspension, particle detachment is caused by mechanical forces, such as foot tapping (Kubota and Higuchi 2013) or displacement due to foot penetration (Oberoi et al. 2010). Moreover, Goldasteh et al. (2014) propose that the main mechanism for particle resuspension is the high speed airflow generated at the gap of the shoe sole during the upward and downward motion of the foot. Considering that the walking style was the same for all experiments, particle detachment happened under the same conditions. Removal forces that are connected with these conditions were likely in the same order of magnitude and responsible for the fraction of particles leaving the surface.

4.8 Resuspension rate

The resuspension rate was calculated using the coupled set of Equations (4.8) and (4.9). Table 4.3 summarizes the resuspension rate for all experiments. On average the resuspension rate for all the experiments was 6.61 10^{-3} hr^{-1}. In general, the range of the resuspension rate was between 10^{-2}-10^{-3} hr^{-1}. These results are in agreement with other studies for resuspension by walking in a chamber or in real environment which found values in the range 10^{-2}-10^{-6} hr^{-1} (Qian and Ferro 2008; Qian et al. 2008; Shaughnessy and Vu 2013; Tian et al. 2014).

Table 4.3 also suggests that the resuspension rate is independent from the initial dust loading on the floor. The different dust loadings influence indoor PM_{10} concentration but not the resuspension rate. Factors such as walking speed, weight of person, number of persons inside the room, shoes, type of floor, style of walking contribute different on the resuspension rate (Qian and Ferro 2008; Rosati et al. 2008; Shaughnessy and Vu 2012; Kubota and Higuchi 2013; Tian et al. 2014; Oberoi et al. 2010; Boor et al. 2013a; Qian et al. 2014). The different walking patterns used in the experiments had no effect on indoor concentration or on resuspension rate. Even though different walking speeds were examined in 4 experiments (10/09, 12/09 higher walking speed, 11/09, 13/09 lower walking speed) no correlation found between the walking speed and the resuspension rate. Probably, the effect of walking speed on particle resuspension should have an effect for a wider range of speeds. The average walking speed and resuspension rate for every dust loading is presented in Table 4.4.

Table 4.3: Resuspension rate for different dust loadings.

Experiment	Resuspension rate, r, hr^{-1}
Dust loading, 25 g/m^2	
04/07	$7.15\ 10^{-3}$
10/07	$6.64\ 10^{-3}$
26/07	$7.31\ 10^{-3}$
30/07	$8.60\ 10^{-3}$
Average	$7.43\ 10^{-3}$
Dust loading, 15 g/m^2	
21/06	$4.46\ 10^{-3}$
26/06	$5.05\ 10^{-3}$
08/08	$5.28\ 10^{-3}$
10/08	$6.19\ 10^{-3}$
Average	$5.25\ 10^{-3}$
Dust loading, 5 g/m^2	
02/07	$4.05\ 10^{-3}$
28/06	$4.63\ 10^{-3}$
12/08	$6.65\ 10^{-3}$
13/08	$6.48\ 10^{-3}$
10/09*	$5.56\ 10^{-3}$
11/09*	$8.38\ 10^{-3}$
Average	$5.96\ 10^{-3}$
Dust loading, 1 g/m^2	
12/07	$7.81\ 10^{-3}$
24/07	$2.06\ 10^{-2}$
15/08	$1.10\ 10^{-2}$
14/08	$1.35\ 10^{-2}$
12/09*	$2.39\ 10^{-2}$
13/09*	$9.60\ 10^{-3}$
Average	$1.44\ 10^{-2}$

*Different walking speed

Table 4.4: Average walking speed during walking period for different dust loadings.

Dust loading, g/m^2	Average walking speed, m/s	Average resuspension rate, hr^{-1}
25	0.85	$7.43\ 10^{-3}$
15	0.83	$5.25\ 10^{-3}$
5	0.84	$5.96\ 10^{-3}$
1	0.84	$1.44\ 10^{-2}$

4.8.1 Influence of environmental factors

The air temperature and relative humidity had no effect on resuspension rate for the range of the environmental conditions occurred in the laboratory. The average temperature inside the laboratory for all the experiments was 30 ± 1 °C and the average relative humidity was 45 ± 4 %. The relative humidity was found to affect the adhesion force between the particle and the substrate through capillary forces (Hinds 1999; Biggs et al. 2002; Rosati et al. 2008; Qian et al. 2014; Bateman et al. 2014). However, the influence of relative humidity on particle detachment becomes significant on wider ranges of 20% - 90% RH (Biggs et al. 2002; Bateman et al. 2014). Qian and Ferro (2008) also found no effect on resuspension rate for RH range 26.4 % - 51%, while, Tian et al. (2014) found a dependence on resuspension for two levels (40% and 70%) of relative humidity.

4.8.2 Resuspension rate time dependence

The time dependence of the resuspension rate was evaluated for two time-periods. In stage 1, which is the burst of particle emission, the first 4 minutes of the activity were chosen due to higher rates observed at this period, and in stage 2 the remaining time of the activity was chosen. Figure 4.6 presents the resuspension rate for the two stages for all the experiments.

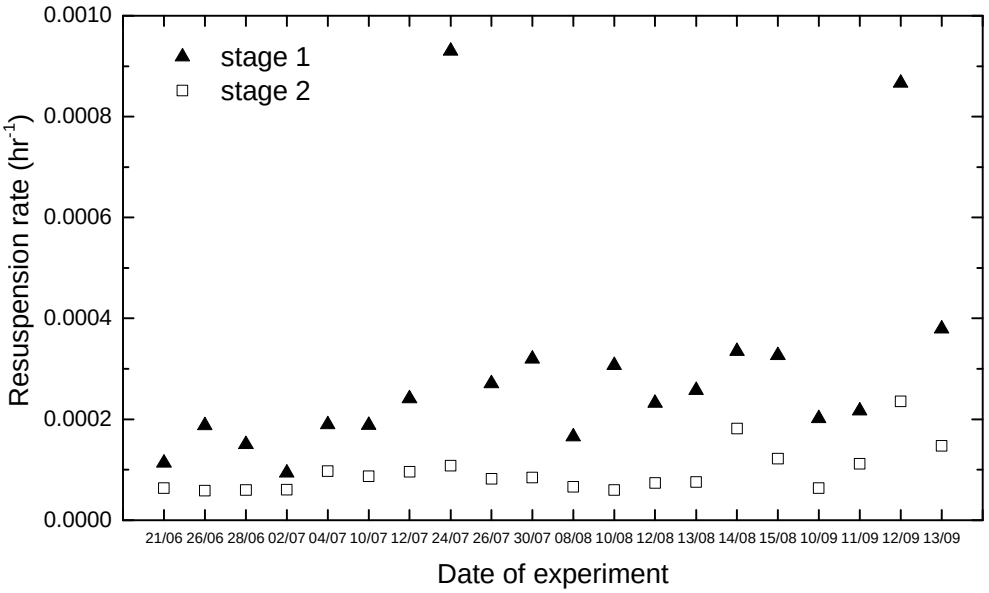

Figure 4.6: Comparison of resuspension rate for stage 1 and 2 for all the experiments.

Figure 4.6 demonstrates a strong dependence of resuspension rate versus time. The first minutes of the event are characterized by a higher resuspension rate than the remaining time. The resuspension rate at stage 1 is higher by 68% in comparison to stage 2. Strongly adhered particles are more difficult to detach from the surface. Thus, in the first minutes of the walking activity resuspension occurs for particles which are less adhered on the surface. As a result, the resuspension rate is higher on the first minutes of the activity and more particles detach from the surface. Similar results were found both in cases of human-induced particle resuspension (Qian et al. 2008) or in wind tunnel studies (Wu et al. 1992; Ibrahim et al. 2003; Wang et al. 2012). Turbulent airflow generated by human walking, adhesion forces and type of deposit (monolayer or multilayer) are responsible for the fluctuation on resuspension rate through exposure time (Boor et al. 2013a).

4.9 Indoor model performance

Using the Equation (4.10) indoor PM_{10} concentration can be predicted for each time step. The resuspension rate *r* and surface loading *L*, are already known from Equations (4.8) and (4.9), thus, indoor particle concentration is derived by setting the values for every time interval. The results are presented in Figure 4.7 for different surface dust loadings.

The physical processes that the model takes into account is penetration of particles from outdoors, exchange rate of the indoor air, deposition of particles onto surfaces and emission by resuspension. Coagulation and condensation are assumed to have no major effect on indoor particle dynamics. Accordingly, coagulation influences directly the particle number distribution and has minor effect in total mass concentration of particles (Nazaroff 2004). Moreover, it is important only in high number concentrations and therefore, can be neglected when total number concentration is lower than 10^4 cm^{-3} (Hussein et al. 2009). Indoor number concentration in all experiments was under that limit and independent of any walking activity, supporting the assumption of negligible coagulation during walking experiments inside the laboratory.

On the other hand, deposition found to be dominant in the calculations of the total losses rate inside the laboratory. Although, the air exchange rate was one order of magnitude lower than the deposition rate, nevertheless, it was significant enough not to neglect it. The net result from infiltration of outdoor particles, air exchange of indoor particles and deposition on the surfaces of the laboratory leaded to a steady state concentration C_{inf}, which, is directly associated with the background PM_{10} concentration

inside the laboratory. The indoor PM_{10} concentration decreases after the activity period tending to reach the background concentration approximately 3 hours after the end of the experiment (Figure 4.7).

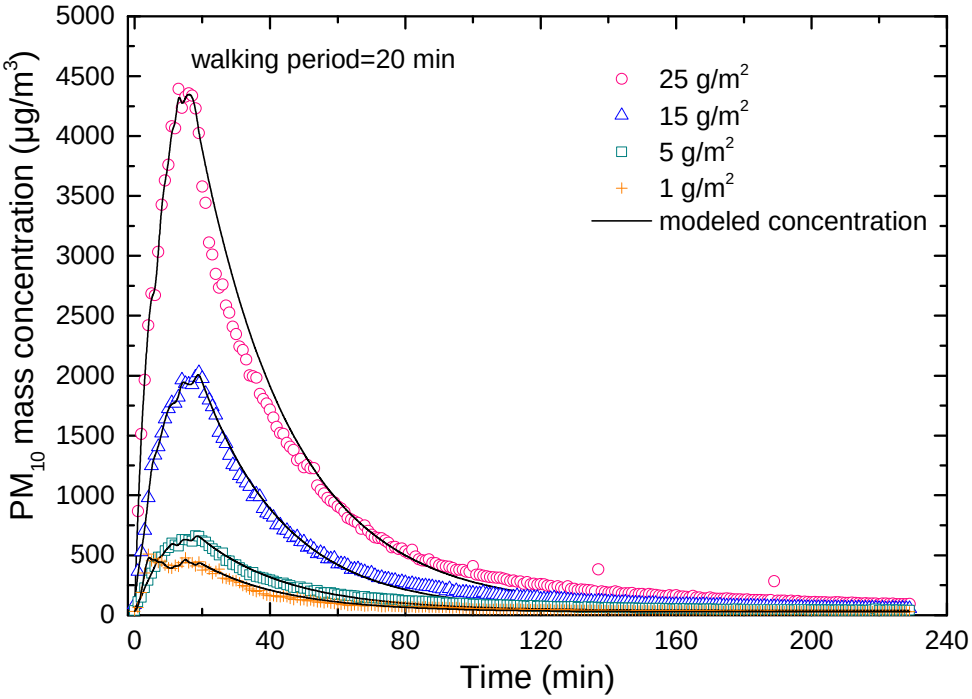

Figure 4.7: Mass concentration of indoor PM_{10} during walking experiment and comparison with model for dust loadings 25, 15, 5 and 1 g/m^2. Data from Figure 4.3.

4.10 Conclusions

The resuspension rate provoked by human walking was estimated inside a laboratory room. Different dust loadings used to cover the floor while the walking style was the same for all experiments. Particle number and mass concentrations were measured simultaneously. It was found that the walking activity had effect only on particle mass concentration. This behavior was attributed to particle size, where larger particles were easily resuspended (PM_{10}), whereas, smaller particles (<1 µm) were not easily detached.

The resuspension rate for PM_{10} estimated in the range of 10^{-2}-10^{-3} hr^{-1}. Different dust loadings on the floor contribute directly to the indoor mass concentration of particles but have no effect on the resuspension rate. Although, higher dust loading resulted in higher emission rates and is associated with higher potential of dust particles than can detach from the surface, the fraction of particles leaving the surface is related

to the magnitude of the removal forces. Accordingly, the resuspension rate depends mainly on walking speed rather on walking pattern or dust loading.

The indoor mass balance model well-predicted the indoor particle concentration in both activity and post-activity period. However, resuspension of indoor particles is a complicated physical process dealing with the adhesion forces of particles on the floor and the removal forces acting upon them, thus a simultaneous investigation on particle dynamics both on the floor and the ambient air is necessary.

Chapter 5

Modeling of particle resuspension from a turbulent airflow

5.1 Introduction

Particle removal from surfaces is a frequent phenomenon in nature, involving a number of physical processes as particle adhesion, particle-surface and particle-fluid interactions. Particle resuspension describes the physical processes that lead to particle detachment from the surface and its eventual suspension in the fluid (air). A particle is entrained into the ambient air under the influence of an external force, whilst resuspension is the result of the competition between the forces that bind the particle to the surface and the removal forces the particle is exposed to.

Intermolecular forces describe the attractive or repulsive forces between macroscopic bodies and are essentially of electromagnetic origin. These forces act between all atoms or molecules, independent of their molecular properties, and they are always present. They are known in general as van der Waals forces. Van der Waals forces determine, among others, the properties of gases, liquids and solids such as adhesion, surface tension, and physical adsorption (Israelachvili 1992). Adhesion phenomena are closely related to intermolecular forces and they usually involve purely physical interactions between the bodies. Adhesive forces may arise also from electrostatic forces (Walton 2008), depending on the particle or surface charges.

Consider a particle resting on a planar surface. Assuming no electrostatic forces (electric field or static-electric image forces), the only forces acting on it originate from its interactions with the planar surface, namely, the van der Waals forces (the gravitational force is neglected as the particles are considered to be small). In the presence of an external force (as, for example, that induced by a turbulent flow) the particle-surface interaction is influenced by the aerodynamic forces generated by the flow. Under some conditions, the particle may detach from the surface when the instantaneous external (aerodynamic) force exceeds the van der Waals forces that bind the particle to the surface.

Reeks, Reed and Hall (1988) proposed a kinetic approach whereby the resuspension rate was evaluated by an energy-balance model (RRH model). According to the RRH model the deposited particle, which is

bound to the surface by a potential well, could resuspend when it accumulates enough energy to escape from the particle-surface well. The authors used a harmonic oscillator to describe the oscillations of the bound particle in the potential well (the harmonic approximation may be relaxed). In the presence of a turbulent airflow, energy is transferred to the particle via turbulent eddies. When the frequency of the energy transferred is close to the natural frequency of vibration of the bound particle energy transfer becomes almost resonant and the particle accumulates enough energy to escape from the potential well, i.e., to resuspend.

Subsequent research led various authors to propose and improve the impact of aerodynamic forces on particle resuspension (Soltani and Ahmadi 1995; Ziskind et al. 1995; Vainshtein et al. 1997; Ziskind et al. 1997). Accordingly, particle resuspension is more likely driven by the drag force and specifically by the moment of the aerodynamic forces acting on the particle. Hence, it was suggested that the drag force breaks of the contact point between the particle and the surface asperity, whereas the lift entrains the particle into the air jet (Ziskind et al. 1997).

The present chapter investigates particle resuspension under the influence of a turbulent airflow for a monolayer and a multilayer deposit. Accordingly, a stochastic model is introduced which incorporates physical interactions between the bodies in touch, as well as the impact from the external airflow using the kinetic approach proposed originally by Reeks et al. (1988). The bound particle, which is considered to oscillate in the potential well, is subject to the airflow and is considered resuspended when the torque (created by the lift and drag forces of the airflow) exceeds the adhesive forces. A numerical procedure is followed where the resuspension rate is calculated by force-balance approximations acknowledging the stochasticity of the physical process itself by taking into account the variability in the magnitude of the adhesive forces due to surface roughness. The objective is to evaluate the impact of contact characteristics on particle resuspension, the role of particle size and the corresponding surface roughness and the influence from an electric particle charge for a monolayer deposit, whilst for a multilayer deposit the position of the layer in a thick deposit was investigated, the influence of fiction velocity and the time-dependency of particle resuspension to the exposure time in the flow.

5.2 Adhesion models

When two bodies are in contact at least one of them deforms. The first theory to describe the stresses between a sphere and a plane was derived as early as 1880 by Hertz, where the elastic character of the

contact between the two bodies was related to the elastic properties of the bodies. However, van der Waals interactions near contact or contact adhesive forces were neglected.

An improvement of the Hertzian theory was proposed by the JKR theory (Johnson, Kendall and Roberts 1971). Unlike the Hertzian contact profile, the JKR model is adhesive and is applicable to elastically deformable particles: it identifies the adhesive force only inside the expanded contact circle between the particle and the surface. A different approach was proposed by Derjaguin, Muller and Toporov (1975)-DMT theory-, where the interaction between the two bodies was considered to be Hertzian (non-adhesive, elastic contact) but with additional adhesive interactions outside the elastic contact zone. Consequently, the DMT model assumes a compressive contact zone and is valid for rigid spheres, whereas, the JKR model incorporates the tensile effect of the contact.

Both theories created a strong debate on which model is applicable to particle adhesion. It was later realized that the two theories represent opposite limits, with the *Tabor* number (Tabor 1977) being used to distinguish between them. Accordingly, for small or hard particles the DMT theory applies, whereas for large or soft particles the JKR theory is more appropriate. Muller et al. (1980) -MYD model- in an attempt to interpolate between these two theories used the Lennard-Jones potential to describe the adhesive force between the two bodies, while Maugis (1992), MD, used the Dugdale approximation to represent surface forces. Both studies found that a dimensionless parameter μ, referred to as the *Tabor* number, or λ in the MD model, specified whether the contact profile follows the JKR or DMT theory. Tsai et al. (1991) -TPL model- used the energy conservation principle to obtain analytic equations that describe the effect of particle deformation on van der Waals forces. The authors presented a modified version of the Lennard-Jones potential that includes the contribution of elastic flattening to the contact zone. The TPL model overcame some limitations of the JKR theory by introducing molecular interactions outside the contact area, thus, presented a more appropriate model for particle deformation due to elastic flattening.

The present model considers the physical interaction between the two bodies accounting for the van der Waals forces. The Lennard-Jones potential is an empirical equation that allows to estimate all physical interactions of the under study system. Unlike the JKR and DMT theory, the Lennard-Jones potential includes both short- and long-range forces acting inside and outside the contact area between macroscopic molecules. Just like the MYD model it includes all pairwise interactions and it is easily applicable than the MD model.

5.3 Lennard-Jones intermolecular potential

The usual expression for the Lennard-Jones potential for two interacting non-polar molecules is (Israelachvili 1992):

$$V_{LJ}(r) = 4\varepsilon\left[\left(\frac{\sigma}{r}\right)^{12} - \left(\frac{\sigma}{r}\right)^{6}\right] \tag{5.1}$$

where ε is the maximum attractive energy between two molecules, σ the distance at which the intermolecular potential is zero and r the distance between the two molecules. The first term represents the (Pauli) repulsive part due to overlapping of electron orbitals (short-range interaction) and the second the long-range attractive contribution (London dispersion interaction).

The Lennard-Jones potential was applied to incorporate physical interactions between the under study bodies in the case of a monolayer and a multilayer deposit. A monolayer deposit consists of one layer of particles adhered on top of a surface, whereas, a multilayer deposit includes several layers of particles sit on top of other particles. In the first case (monolayer), both opposite extremes were considered, therefore particle-surface interactions were modelled for a hard system where the sphere is not deformed when in contact with the surface (Lazaridis et al. 1998) and for a soft system where the sphere in contact with the surface is flattened due to elastic deformation (Tsai et al. 1991). In the second case (multilayer), which includes also interactions between particles, intermolecular interactions were modelled without any deformation (rigid bodies) for both particle-particle and particle-surface interactions.

5.3.1 Particle-surface interaction with deformation

The total interaction energy between a sphere of (initial) radius R_p in contact with a surface in the limit $r \ll R_p$, where r is the distance between the surface of the particle and the substrate surface estimated by the integrated Lennard-Jones potential admitting particle deformation due to elastic flattening is given by (Tsai et al. 1991):

$$V_{sp}(r) = -A\frac{R_p}{6r}\left(1 + \frac{\alpha}{2r}\right) + B\frac{R_p}{28r^7}\left(1 + \frac{7\alpha}{2r}\right) \tag{5.2}$$

with,

$$A = \pi^2 C n_1 n_2, \qquad B = \frac{A}{45}\sigma_{12}^6, \qquad C = 4\varepsilon_{12}\sigma_{12}^6 \tag{5.3}$$

where *A* is the Hamaker constant, α is the relative approach between the particle and the surface that represents the amount of deformation and n_i is the number density of molecules in the solid i. The Lennard-Jones parameters ε_{12} and σ_{12} for a mixture of two species were estimated by the geometric, $\varepsilon_{12} = (\varepsilon_1\varepsilon_2)^{1/2}$, and the arithmetic mean, $\sigma_{12} = (\sigma_1 + \sigma_2)/2$, of the single-species parameters.
When the particle is in static equilibrium with the surface, zero applied load (equilibrium conditions are denoted by a subscript 0), the contact radius a_0 between the sphere and the surface is:

$$a_0 = \sqrt{R_p \alpha_0} \tag{5.4}$$

For a soft system it evaluates to (Tsai et al. 1991):

$$a_0 = 1.81\left(\frac{\Delta\gamma}{K}\right)^{1/3} R_p^{2/3} \tag{5.5}$$

where *K* is the composite Young modulus:

$$K = \frac{4}{3}\left[\frac{(1-\nu_1^2)}{E_1} + \frac{(1-\nu_2^2)}{E_2}\right]^{-1} \tag{5.6}$$

where E_1, E_2 are the material Young's moduli and ν_1, ν_2 are Poisson's ratios for the particle and the surface, respectively. Note the constant 1.81 in Equation (5.5) is approximately 2.66 in the JKR model.
The total interaction force is determined by the first derivate of the total intermolecular energy:

$$F(r) = -\frac{dV(r)}{dr} \tag{5.7}$$

5.3.2 Particle-surface interaction without deformation

The interaction potential of a smooth sphere of radius R_p in contact with a perfectly smooth planar surface, without particle deformation (contact radius is zero,$a = 0$), is obtained by integrating the

Lennard-Jones molecule-molecule interaction potential over the whole sphere interacting with the surface. The total interaction energy V_{sp} is given (Lazaridis et al. 1998):

$$V_{sp}(r) = -\frac{A}{6}C_a + BC_b \tag{5.8}$$

with

$$C_a = \frac{2R_p(R_p + r)}{r(2R_p + r)} + \ln\left(\frac{r}{2R_p + r}\right)$$

$$C_b = \frac{1}{168}\left[\frac{1}{(r + 2R_p)^6} - \frac{1}{r^6}\right] + \frac{R_p}{28}\left[\frac{1}{(r + 2R_p)^7} - \frac{1}{7}\right]$$

where the constants A and B are defined as previously. Equation (5.8) suggests that in the case of no particle deformation ($\alpha = 0$), the Lennard-Jones potential is a function of the particle radius and distance from the surface besides the physical characteristics of the molecules expressed by *ε*, *σ* and *n.* The spherically-symmetric interaction force is given by the negative first derivate of Equation (5.8), while the adhesive force is obtained by the first (attractive) term.

$$F_{adh} = -\frac{dV_{sp}(r)_{attr}}{dr} = -\frac{AR_p}{6r^2} \tag{5.9}$$

Use of the relation between the Hamaker constant and the work of adhesion $\Delta\gamma$($\Delta\gamma = \mathrm{A}/12\pi\sigma^2$, Israelachvili 1992) in Equation (5.9) transforms the absolute value of the attractive force into:

$$|F_{adh}| = \frac{AR_p}{6\sigma^2} = 2\pi\Delta\gamma R_p \tag{5.10}$$

Equation (5.10) is the adhesive force according to the DMT theory. Consequently, the use of the integrated Lennard-Jones intermolecular potential without particle deformation is equivalent to estimating the adhesive force of a rigid particle as predicted by the DMT theory.

5.3.3 Particle-particle interaction without deformation

The interaction energy between two identical spheres of radius R_p in contact is given (Lazaridis and Drossinos, 1998):

$$V_{pp}(r) = -\frac{A}{6}C_c + \frac{9B}{C_1}C_d \tag{5.11}$$

with,

$$C_1 = 2R_p + r$$

$$C_c = \frac{2R_p^2}{C_1^2} + \frac{2R_p^2}{C_1^2 - 4R_p^2} + \ln\frac{C_1^2 - 4R_p^2}{C_1^2}$$

$$C_d = \frac{C_7}{3528} + \frac{C_8}{72} + \frac{C_6}{1296} + \frac{C_5}{360}$$

$$C_7 = \frac{224R_p^2 - 14C_1^2}{C_1^7} + \frac{7C_1^2 - 112R_p^2 - 98C_1R_p}{\left(C_1 + 2R_p\right)^7} + \frac{7C_1^2 - 112R_p^2 + 98C_1R_p}{\left(C_1 - 2R_p\right)^7}$$

$$C_8 = \frac{2C_1R_p^2 - R_pC_1^2}{\left(C_1 - 2R_p\right)^8} + \frac{2C_1R_p^2 + R_pC_1^2}{\left(C_1 + 2R_p\right)^8} - \frac{4R_p^2}{C_1^7}$$

$$C_6 = \frac{12}{C_1^5} - \frac{6C_1 + 18R_p}{\left(C_1 - 2R_p\right)^6}$$

$$C_5 = -\frac{2}{C_1^5} + \frac{1}{\left(C_1 + 2R_p\right)^5} + \frac{1}{\left(C_1 - 2R_p\right)^5}$$

where, A and B represent the same properties as in Equations (5.3) and r is the distance between the two spheres. Likewise, the total interaction force between the two particles is given by Equation (5.7), but using the interaction energy of the two particles in contact (Equation 5.11).

5.4 Model for particle resuspension

5.4.1 Resuspension rate constant

The resuspension rate was calculated via the RRH model (Reeks et al. 1988) and its variants. In the RRH model, the bound particle resuspends under the influence of the aerodynamic lift force induced by the turbulent airflow: both mean and fluctuating parts contribute. The expression for the resuspension rate is similar to the expression for the desorption rate of an absorbed (bound) molecule to a surface, in that it is expressed in the Arrhenius form. Herein, the same formula was used but the exponential factor was obtained as the rate of potential differences whilst resonant energy transfer was considered negligible (Reeks and Hall 2001; Lazaridis et al. 1998). Accordingly, the resuspension rate is given by:

$$J = \omega_0 exp\left(-\frac{Q}{2U}\right) \tag{5.12}$$

where, ω_0 is the typical forcing frequency of the particle in the potential well, *Q* is the height of the potential well at particle detachment with respect to the particle equilibrium position, and *U* is the average potential energy of the particle in the well.

Evaluating particle resuspension without resonant energy transfer, ω_0 can be approximated using the formula (Reeks and Hall 2001):

$$\omega_0 = \frac{1}{2\pi}\left[\frac{\langle \dot{f}^2 \rangle}{\langle f^2 \rangle}\right]^{1/2} = \frac{0.1642}{2\pi}\left(\frac{u_*^2}{\nu_f}\right) \tag{5.13}$$

where, $\langle f^2 \rangle$ is the mean square of the fluctuating removal force, $\langle \dot{f}^2 \rangle$ its time derivative, u_* is the friction velocity and ν_f the kinematic viscosity of the fluid. The numerical prefactor was obtained from the recent work of Zhang et al. (2013) who used Direct Numerical Simulations (DNS).

The potential barrier Q is estimated numerically from the difference of the potential energy at the equilibrium point (minimum energy) and the energy at the detachment point. The detachment point is determined by finding the location where the total force acting on the particle is zero. Thus, the potential barrier is given:

$$Q = V_{sp}(r_{det}) - V_{sp}(r_{eq}) \tag{5.14}$$

where r_{det} is the position of particle detachment, and r_{eq} the particle position at equilibrium.
The average potential energy *U* , in the harmonic oscillator approximation, is written as:

$$U = \frac{1}{2} m\omega_p^2 \langle y^2 \rangle \tag{5.15}$$

where m is the particle mass, ω_p is the natural frequency of vibration of the bound particle and $\langle y^2 \rangle$ is the mean square displacement. For a harmonic potential in the absence of resonance the mean square displacement is written as (Reeks et al. 1988):

$$\langle y^2 \rangle = \frac{\langle f^2 \rangle}{m^2 \omega_p^4} \tag{5.16}$$

whilst, ω_p is estimated by the interaction potential as (Lazaridis et al. 1998):

$$\omega_p = \left[\frac{1}{m} \frac{d^2 V_{sp}(r)}{dr^2} \right]_{eq}^{1/2} \tag{5.17}$$

Equation (5.17) is evaluated at equilibrium, at the distance of the closest approach where the interaction energy is at a minimum. The distance of closest approach is determined from the zero of the first derivate of the total potential, $dV_{sp}(r)/dr = 0$.
The number of particles remaining on the surface *N(t)* is described by a first order kinetic equation (Reeks et al. 1988; Lazaridis et al. 1998). Hence, the fraction of particles remaining on the surface is obtained as:

$$\frac{N(t)}{N(0)} \equiv f_R(t) = exp(-Jt) \tag{5.18}$$

where t is the time the particles are exposed to flow.

5.4.2 Adhesive force distribution

The previous discussion assumed that a smooth particle interacted with a smooth surface. However, both particles and surfaces are rough. Surface roughness results in a significant reduction of the adhesive forces

with a variable spread. The stochastic nature of surface roughness, with the associated distribution of asperity heights and their peak-to-peak distances, is represented by an adhesive-force probability distribution in the RRH model. The usual choice is the log-normal probability density function (Reeks et al. 1988; Lazaridis et al. 1998). Specifically, the effect of surface roughness is incorporated via the effective (renormalized) particle radius R_{eff}. The reduced effective particle radius leads to a reduced adhesive force, the origin of the force decrease being surface roughness. The adhesive force reduction is accompanied by a spread in the adhesive force distribution. Defining the dimensionless particle radius $R' = R_{eff}/R_p$ the probability density function is:

$$\phi(R')dR' = \frac{1}{(2\pi)^{1/2}\ln\sigma_a} exp\left\{-\frac{1}{2(\ln\sigma_a)^2}\left[\ln\frac{R'}{\overline{R'}}\right]^2\right\} d(\ln R') \tag{5.19}$$

where $\overline{R'}$ is the geometric mean of R', a measure of the reduction in adhesive forces (and consequently referred to as adhesive-force reduction) and σ_a is the standard deviation of the probability function representing the spread in adhesive forces. In the absence of additional information, $\overline{R'}$ was chosen to be the physical particle radius reduced by a factor that best fits the experimental data (Lazaridis et al. 1998). On the other hand, σ_a was chosen according to the experimental data under investigation.

The description of adhesive forces in terms of the probability distribution of the effective radius is an approximate attempt to model the effect of surface roughness on the adhesive forces. No attempt is made to model surface roughness in terms of single asperity contact (usually taken to be semi spheres) or multiple asperity contacts (Prokopovich et al. 2011). It is noteworthy that recent work on asperity modeling of surface roughness has identified small-scale and large-scale asperities, thereby introducing different length scales associated with surface roughness (Guigno and Minier 2014).

The fraction of particles remaining on the surface was obtained by averaging over the log-normal distribution. Specifically, the fraction remaining after exposure to flow for time t is:

$$f_R(t) = \int_0^\infty exp[-J(R')t]\phi(R')dR' \tag{5.20}$$

The fractional resuspension rate Λ(t), is estimated by the fraction of remaining particles as (Reeks et al. 1988; Lazaridis et al. 1998):

$$\Lambda(t) = -\frac{df_R(t)}{dt} \tag{5.21}$$

5.5 Aerodynamic removal forces

Particles in boundary layers are usually characterized by the dimensionless particle diameter expressed in wall units $d^+ = d_p u_*/\nu_f$, with u_* the friction velocity and ν_f the fluid kinematic viscosity. Turbulence characteristics play an important role on the particle resuspension mechanism (van Hout 2013). If a particle is small enough to be submerged into the viscous sub-layer of the boundary layer, viscous forces predominate the coherent structures (ejections, sweeps, vortical structures), known as 'bursts' of the flow and the influence of ejections and sweeps of the turbulent flow are expressed via shear stress (Ziskind et al. 2005). On the other hand, if the particle is large enough to protrude from the viscous sub-layer, large-scale motions and eddies become dominant. A particle is considered to be fully submerged into the viscous sub-layer when its diameter is smaller than the viscous sub-layer thickness, i.e. when $d^+ < 5 - 10$ (Guigno and Minier 2014). However, the distinction between the two mechanisms is not always clear as the particle size may be of the same order as the viscous sub-layer thickness.

Particles in the experimental data (Reeks and Hall 2001; Ibrahim et al. 2003) used in the present study fulfilled the above condition and were fully submerged into the viscous sub-layer. The aerodynamic forces acting on a particle due to the turbulent airflow were considered to be the lift, F_l, and the drag, F_d, forces. A recent study on the effect of the lift, drag and moments of the aerodynamic forces identified that at high Reynolds number (high turbulence) normal forces (lift) contribute significantly to particle movement because the magnitude of lift and drag forces become comparable. On the other hand, at low Reynolds numbers (laminar flow) sliding and most probably rolling is responsible for particle detachment (Martinez et al. 2009). Appropriate expressions for the aerodynamic removal forces (lift and drag) depend on the characteristics of the turbulent boundary layer.

5.5.1 Moments of aerodynamic forces

Several authors have investigated particle detachment under a turbulent airflow and have concluded that, for a particle resting on a surface, detachment occurs as a result of the action of the moments of the aerodynamic forces, lift and drag (Soltani and Ahmadi 1995; Ziskind et al. 1995; Vainhstein et al. 1997; Ziskind et al. 1997; Ibrahim et al. 2003). Moreover, it has been suggested that a particle resuspends either by sliding or by rolling about an asperity in the contact zone (Soltani and Ahmadi 1995; Ibrahim et al. 2003;

Guingo and Minier 2008). The present model also considers the contribution of the moments of the aerodynamic forces on particle resuspension. However, two different scenarios were considered depending on whether elastic flattening was modelled or not.

For a hard particle resting on a rough surface between two asperities (Figure 5.1a), the total couple acting on the particle arises from the torque generated by the lift, F_l and the drag, F_d force (Reeks and Hall 2001):

$$\Gamma = \frac{\delta}{2} F_l + R_p F_d \tag{5.22}$$

where δ is the distance between the two asperities. The corresponding effective force is obtained:

$$F = \frac{1}{2} F_l + \frac{R_p}{\delta} F_d \tag{5.23}$$

The authors suggested a value of 100 for the geometric factor R_p/δ, a quantity that corresponds to the measured ratio of the tangential force to the normal force. Thus, Equation (5.23) can be rewritten:

$$F = 0.5 F_l + 100 F_d \tag{5.24}$$

Equation (5.24) implies that the dominant part of the removal forces originates from the drag rather than the lift force. This conclusion is a direct consequence of the (experimentally determined) value of the geometric factor (100). Clearly, the geometric factor depends on surface-roughness parameters, i.e., the distance between the (large-scale) asperities and the particle radius. Nevertheless, the lift force will not be neglected, since it is the force that elevates the particles into the flow after the particle-surface contact has been broken (Ziskind et al. 1997).

On the other hand, for a soft system, where elastic flattening is significant, deformation of the particle occurs. According to Tsai et al. (1991) a common contact area is created (between the deformed particle and the surface). Figure 5.1b corresponds to a geometry where a deformed particle is in contact with the surface. Accordingly, the moment of the aerodynamic forces is:

$$\Gamma = 1.4 R_p F_d + a_0 F_l \tag{5.25}$$

where 1.4 is a correction factor due to the non-uniformity of the flow field (O'Neill 1968).

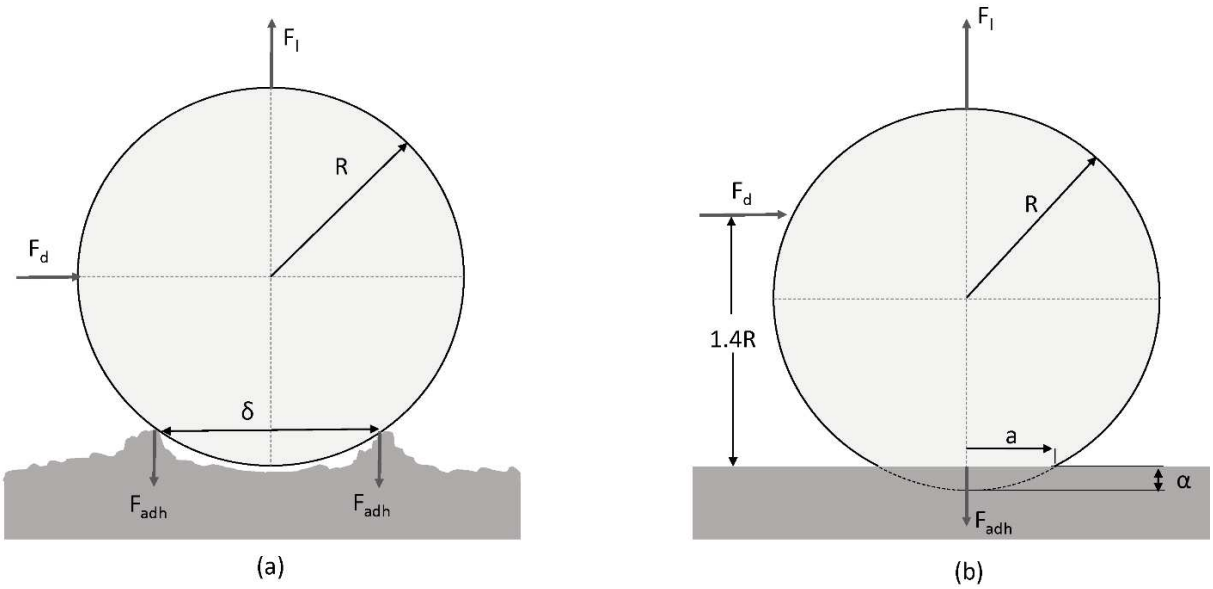

Figure 5.1: Particle-surface geometry: a) Particle resting on top of two asperities, b) Particle in contact with an effectively smooth surface.

5.5.2 Mean and fluctuating components of the aerodynamic forces

The aerodynamic forces induced by the turbulent flow may be decomposed into two components: the mean and the fluctuating parts. For a sphere set on a surface in a wall-bounded shear flow (fully immersed in the boundary layer), the mean lift force given by Leighton and Acrivos (1985) is:

$$F_l = 9.22\rho_f \nu_f^2 (R^+)^4 \tag{5.26}$$

where ρ_f is the fluid density and R^+ is the dimensionless particle radius ($R^+ = R_p u_*/\nu_f$). The fluid properties are given in Table 5.1. Near wall effects, as shown by O'Neill (1968), modify the drag force acting on a particle in the viscous sub-layer by multiplying the Stokes drag by 1.7:

$$F_d = 1.7 \times 6\pi\rho_f u_*^2 R_p^2 \tag{5.27}$$

The above expressions are valid for the mean lift and drag forces acting on the particle and were used in Equations (5.24) and (5.25). However, the fluctuating part of the aerodynamic forces is also needed to obtain the mean square displacement $\langle y^2 \rangle$. Recently, Zhang et al. (2013) used a value of 0.366 for the fluctuating removal force (f_{RMS}) obtained from DNS (Direct Numerical Simulation) data, a value that was

also used herein to obtain the contribution from the fluctuating part of the aerodynamic (lift and drag) forces to their mean value.

Table 5.1: Fluid properties (Hinds 1999).

Temperature, K	Air density, kg/m^3	Dynamic viscosity, kg/s m	Kinematic viscosity, m^2/s
293	1.2	1.81 10^{-5}	1.51 10^{-5}

5.6 Lennard-Jones parameters

The parameters ε and σ in the Lennard-Jones potential were either found in the literature or estimated from empirical expressions. In general, they are not easy to find: in particular, they are not easily available for most metallic elements and are usually published for gases or liquids. A common way to estimate them is from viscosity data (Poling, Prausnitz and O'Connell 2001). Most authors relate ε and σ to the critical constants of the compound with empirical expressions via the so-called Chung method (Chung et al. 1984). Accordingly, gas kinetic theory is used to obtain correlations for the viscosity and thermal conductivity of polar and nonpolar gases. These correlations lead to expressions for ε and σ in terms of macroscopic parameters such as the critical constants. The parameters expressed in terms of the critical temperature and volume are:

$$\frac{\varepsilon}{k} = \frac{T_c}{1.2593}, \sigma = 0.809 V_c^{1/3} \tag{5.28}$$

where T_c is the critical temperature in K and V_c is the critical volume in cm^3/mol. The above equations are suitable for the calculation of the Lennard-Jones parameters when the viscosity is empirically estimated. Due to the absence of data for metallic compounds, we consider that Equations (5.28) are suitable enough to estimate ε and σ. To support this assumption, the two equations were tested for compounds with already known parameters (CH_4, HF, Ar, SO_2): the results from Equations (5.28) were in good agreement with the experimentally estimated ε and σ.

Moreover, the availability of critical constants for metallic elements is also limited. Based on the work by Aniya (1997), the critical temperature and volume of metallic elements are related to the boiling temperature T_b and atomic radius R_0 by:

$$T_c = 14\frac{T_b}{4}, V_c = 1.65\frac{8\pi N_A R_0^3}{3} \tag{5.29}$$

where N_A is Avogadro's number. If no information on ε and σ is found in the literature Equations (5.28, 5.29) were used. The Lennard-Jones parameters used in this study are listed in Table 5.2.

Table 5.2: Lennard-Jones parameters.

Element/Compound	ε /k, K	σ, Å
Alumina	4444.8	3.61
Stainless steel	3264	2.44
Graphite	71.4	3.29
Glass	4199	2.69

5.7 Electrostatic forces

The electrostatic forces between a particle and a surface arise from the presence of a net charge on the particle or the presence of an external electric field. The most common source of particle charge, when no external electrical field is applied, is triboelectric charge transfer (Walton 2008).

When a particle with a uniformly distribution of charge Q on its surface is near a surface, an image charge –Q is induced in the surface. The resulting electrostatic force is modelled by a single point charge Q at the particle center. Hence, the Coulomb force is:

$$F_e = -\frac{Q^2}{16\pi\varepsilon_0\left(R_p + r\right)^2} \tag{5.30}$$

where ε_0 is the permittivity of the medium surrounding the particle, and *r* is the distance of the particle surface from the planar substrate, as previously defined. Equation (5.30) is also known as the electrostatic image force, due to the redistribution of the particle charge on the substrate (Feng and Hays 2003; Walton 2008). The electrostatic force increases with increasing particle charge and decreases with increasing particle size.

However, the electrostatic image force is underestimated for a point charge at the center of the particle because the strong contribution of the charge in the vicinity of the contact area is not considered (Zhou et al. 2003). At very close distance of the particle to the surface, the electrostatic image force corresponds to

a distribution of charge points on the particle surface rather than a single charge point in the center of the particle. It has been proposed that the image force is higher by a factor of $1 + 4/\pi$ and that it depends on the distribution of the point charges near the contact point (Czarnecki and Schein 2004). Although the electrostatic force calculated by Equation (5.30) might not reflect its actual magnitude at very short distances of the particle to the surface, we assumed a single point charge at the center of the particle since the purpose of the present study is to emphasize the effect of particle charge in resuspension.

Since, $R_p + r$ corresponds to the distance between the particle center and the surface, it was assumed that this distance can be modelled using the renormalized particle radius (R') to represent surface roughness and the reduction of the adhesive forces. The contribution of electrostatic forces was introduced in the model by adding the electrostatic force to the total intermolecular force at the evaluation of the detachment point.

5.8 Monolayer resuspension

5.8.1 *Tabor* number

Tabor (1977) found that the DMT and JKR theories represent two opposite extremes and proposed the Tabor number to determine which theory is applicable based on material properties. Accordingly, the Tabor number is given:

$$\mu = \left(\frac{\Delta\gamma^2 R_p}{K^2 z_0^3}\right)^{1/3} \tag{5.31}$$

where, z_0 is the equilibrium or minimum separation in the Lennard-Jones potential. Herein, z_0 is equitable with σ (Equation (5.1)), therefore, for a system of a particle and a surface z_0 in Equation (5.31) can be replaced by σ_{12}. Table 5.3 provides the material properties required in the model for the compounds studied in this chapter.

The Tabor number expresses the ratio of the elastic deformation at the point of separation to the effective range of surface forces (z_0). If $\mu < 0.1$ then the DMT theory applies (hard material), whereas, for $\mu < 5$ the JKR theory is valid (soft material) (Johnson and Greenwood 1997).

Generally, physical interactions between two bodies usually involve an elastic, or even a plastic, deformation (Tsai et al. 1991). Although, the JKR theory is generally accepted to model the elastic contact

between the two bodies (Johnson and Greenwood 1997), each under study system was checked explicitly in order to examine which regime (DMT-Lennard-Jones potential without deformation or TPL-Lennard-Jones potential with deformation) corresponds to each system. Elastic deformation was addressed via the Tabor number, Equation (5.31), whilst Table 5.4 presents the calculated Tabor number for the interactions considered in this chapter.

Table 5.3: Material properties (Reeks and Hall 2001; Ibrahim et al 2003; Goldasteh et al 2013).

Material properties	Alumina	Graphite	Glass	Stainless steel
Work of adhesion for stainless steel surface, J/m^2	0.56	0.15	-	-
Work of adhesion for glass surface, J/m^2	-	-	0.4	0.15
Young's modulus, 10^{10} N/m^2	35	2	8.01	21
Poisson's ratio	0.3	0.3	0.27	0.29
Density, kg/m^3	1600	2300	2420	7830/8000*
Number density, 10^{28} #/m^{-3}	0.94	11.5	2.43	8.44/8.63

* Applied to Reeks and Hall (2001)/ Ibrahim et al. (2003) experimental data, respectively.

Table 5.4: Tabor number μ for different particle-surface systems.

Particle-surface system	Tabor number μ
10 μm alumina particles/stainless steel surface	1.16
20 μm alumina particles/stainless steel surface	1.46
10 μm graphite particles/ stainless steel surface	1.88
70 μm stainless steel particles/glass surface	1.87
72 μm glass particles/glass surface	4.45
32 μm glass particles/glass surface	3.40

The Tabor number in all cases was calculated in the range $0.1 < \mu < 0.5$. Using the map presented in Johnson and Greenwood (1997), the results indicate that the under study systems are located between the two regimes-DMT and JKR theory. As noted by the authors, the best way to investigate surface forces in the transition regime is to determine the force of interaction through the Lennard-Jones potential. In the following sections, both cases were considered (no flattening, $a = 0$/elastic flattening,$a \neq 0$) for each set of experiments since the predicted particle deformation is slight (Tabor number in the transition

regime). Hence, the integrated Lennard-Jones potential without particle (Lazaridis et al. 1998) or with deformation (Tsai et al. 1991) will be used to investigate which adhesion model, used in the resuspension rate expression, reproduces best the experimental results.

5.8.2 Reeks and Hall (2001) experiments

Reeks and Hall (2001) performed resuspension experiments using 10 and 20 μm (diameter) alumina particles and graphite particles on a stainless steel surface. The spread of the adhesive force distribution used in our simulations was taken from their experiments on tangential and normal forces, whereas the reduction factor was based on Lazaridis et al. (1998). Table 5.5 lists the parameters of the adhesive force distribution for each experiment. Both parameters have significant influence on the calculated resuspension rate by their effective modeling of surface roughness. The Reeks and Hall (2001) experiments were characterized by a relative broad distribution with substantially reduced adhesive forces. We note a significant difference in the reduction factor used in our simulations and those based on the JRK adhesion model since the adhesion models differ.

Table 5.5: Reduction and spread of the adhesive force distribution used to model the experiments of Reeks and Hall (2001).

Particle/Surface	Reduction factor, $\overline{R'}$	Spread, σ_a
Alumina/Stainless steel	1000	10.4
Graphite/Stainless steel	1000	19

Model predictions and experimental results for 10 μm alumina particles are compared in terms of the fraction of particles remaining on the surface (after an 1 s exposure to the flow) versus friction velocity in Figure 5.2. Model predictions considered only the lift force (dotted line) or the moments of the aerodynamic forces (lift and drag, solid line). The adhesion model without elastic deformation was used in both cases. The model with only the aerodynamic lift force results in a substantial underestimation of the resuspension rate. When the moment of the aerodynamic forces, Equation (5.24), was used predictions were in good agreement with experimental data for friction velocities higher than 1 m/s. Thus, the lift force is insufficient to cause particle detachment; instead, the moment of the two aerodynamic forces is responsible for particle detachment, rolling being the dominant detachment mechanism. Similar findings have been reported in previous studies (Ibrahim et al. 2003; Reeks and Hall 2001; Guingo and Minier 2008;

Goldasteh et al. 2013). Since, Equation (5.24) suggests that the dominant contribution to the total moment arises from the drag force (a direct consequence of the choice of the geometric factor), its contribution to particle detachment cannot be neglected. In all subsequent calculations the moments of the aerodynamic forces were used into the resuspension model, the moments providing the effective mechanism for particle resuspension due to a turbulent airflow.

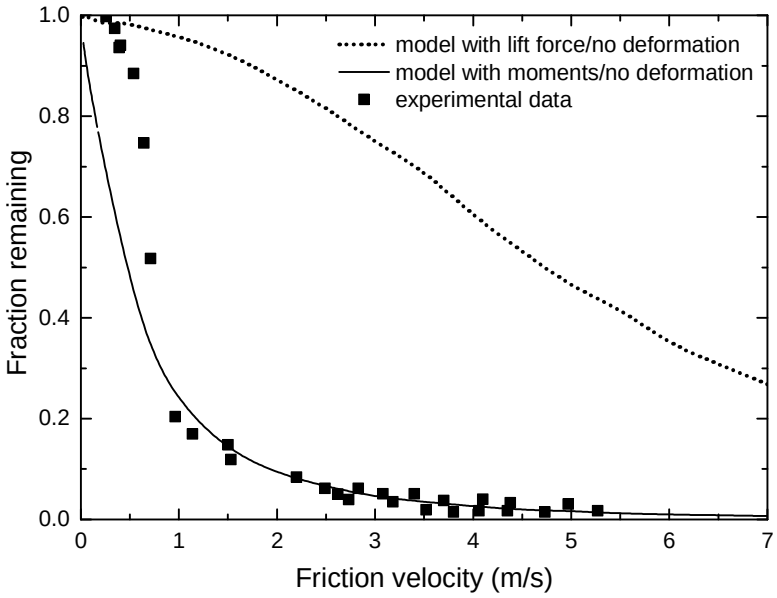

Figure 5.2: Comparison of model predictions (lines) with experimental data (filled squares) for 10 μm alumina particles (Reeks and Hall 2001). Effect of the moments of the (lift and drag) aerodynamic forces. Particle-surface interactions modelled without particle deformation.

Figures 5.3a and 5.3b present model results for 10 and 20 μm alumina particles, respectively, where the particle-surface interactions were modelled for the two limiting cases: no particle deformation ($a = 0$) and particle elastic deformation ($a \neq 0$). Good agreement with experimental data is found for both cases but at different regimes, one at low friction velocity and the other at higher friction velocity. Use of the model that incorporates elastic deformation reproduces well the experimentally observed resuspension rate at low friction velocities < 1 m/s (10 μm particles) and < 0.5 m/s (20 μm particles), i.e., weakly bound particles: at higher friction velocities the resuspension rate is considerably underestimated. Neglect of particle deformation in the particle-surface interaction results in good agreement with the experimental data at higher friction velocities > 1 m/s (10 μm particles) or > 0.5 m/s (20 μm particles), i.e., for particles strongly bound to the surface (high adhesive forces).

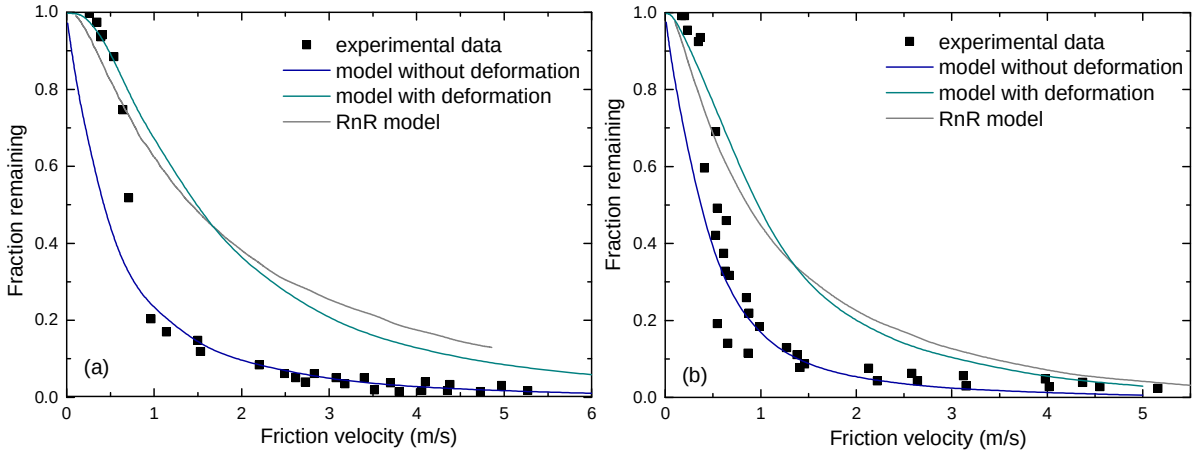

Figure 5.3: Comparison of model predictions (lines) with experimental data (filled squares) for alumina particles (Reeks and Hall 2001). Effect of elastic deformation and comparison with RnR model for: a) 10 μm alumina particles, b) 20 μm alumina particles.

The comparison of predictions of the RnR and the present model in Figure 5.3 suggests that the model with elastic deformation predicts resuspension rates similar to the predictions of RnR i.e., good agreement with experimental data is found at low friction velocity. Recall that the two models use the same kinetic approach to estimate the resuspension rate J, and they both use adhesion models for deformable particles in contact with a rough surface. Herein, the integrated Lennard-Jones potential with elastic deformation (flattening) was used, whereas the RnR model is based on the JKR adhesion theory for the elastic character of contact area. It is highly probable that the RnR model predicts more accurately the resuspension rate of rather large particles (and hence more deformable). The large distribution of particle sizes (12 ± 6 μm for 10 μm alumina particles, 23 ± 7 μm for 20 μm alumina particles) used in these experiments, in conjunction with the RnR predictions, suggests that large particles (and weakly adhered) resuspend first. On the other hand, model predictions imply that smaller particles, which are not elastically deformed, bind strongly to the surface and resuspend at higher friction velocities (> 0.5 or 1 m/s, depending of particle size). A similar observation was made by Henry and Minier (2014) in that the RRH model seems to predict accurately the resuspension rate of large particles and not as accurately as of smaller particles.

The results also indicate that, for these experiments and more importantly for the surface characteristics of the substrate, bigger particles experience limited surface roughness due to their size and due to a relatively broad distribution of adhesive forces ($\sigma_a = 10.4$). In a sense, the larger particles rest on numerous small-scale asperities feeling a relatively smooth surface (they experience limited surface roughness) because the average asperity height is negligible compared to the particle diameter. Hence, a

common contact area is created (Figure 5.1b), the large particles deform and the elastic flattening contribution to the particle-surface interaction potential becomes important. Indeed, the bigger the particle and bigger the contact radius is, as suggested by Equation (5.5). Smaller particles, however, feel the surface roughness more effectively by interacting strongly with a small number of asperities. The asperity height becomes significant for these smaller particles, and the contact profile alters: they rest on top of a few asperities, they remain less deformed, and elastic deformation becomes insignificant. These observations highlight the complicated nature of the adhesion of rough particles to rough surfaces, the nature of single or multi-asperity interactions, and the necessity for more detailed (microscopic) modeling of surface roughness and its relation to observed particle deformation, as for example in Henry et al. (2012) and Prokopovich and Starov (2011).

Figure 5.4 presents model results for 10 μm graphite particles. As before, at low friction velocities the particle-surface interaction may be represented by the elastic character of the contact: the model with elastic deformation predicts resuspension rates that reproduce the experimental data. At higher friction velocity the particle-surface interaction approach that of a rigid contact, and the model without the elastic deformation successfully reproduces the experimental data. Contrary to the case of the alumina particles, for the graphite particles the transition between the two regimes occurs at higher friction velocities (1.5 - 2 m/s). A possible reason is that graphite particles had larger diameter dispersion (18 ± 12 μm) than the alumina particles (23 ± 7 μm), thus a swift between the two regimes would be expected at higher friction velocities, corresponding to a larger number of small strongly bound particles.

A significant difference between RnR model and the model with elastic flattening is observed in the graphite data. Figure 5.4 shows that the two adhesion models with elastic deformation predict different resuspension rates with considerably lower rates (higher adhesion) predicted by the RnR model. Graphite particles on the stainless steel surface have the highest value of the Tabor number μ (1.88), corresponding to the softest system for Reeks and Hall (2001) experiments. The JKR theory predicts a contact radius that is proportional to the numerical constant 2.66, whereas, in the present model the constant is 1.81, Equation (5.5). Tsai et al. (1991), contrary to the JKR theory, considered the interaction (attractive and repulsive) over the whole volume of the particle-surface interaction. This leads to a smaller contact radius between the particle and the surface, and hence weaker adhesive force and higher resuspension rates. The numerical results imply that for a softer system the differences between the two theories may become substantial. Further support to this conclusion is provided by noting that the results obtained by the RnR and the present model for alumina particles on stainless steel surface, along with the lower value of μ (Table 5.4), are similar.

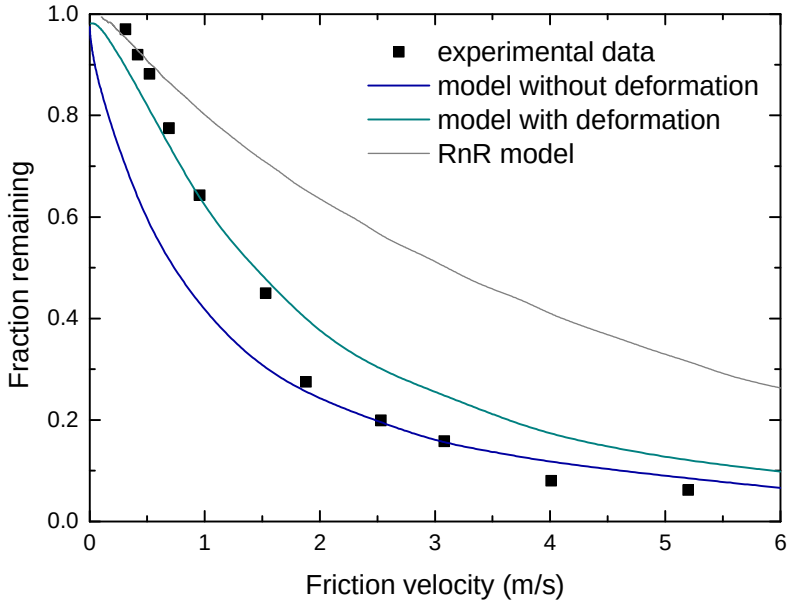

Figure 5.4: Comparison of model predictions (lines) with experimental data (filled squares) for 10 µm graphite particles (Reeks and Hall 2001). Effect of elastic deformation and comparison with RnR model.

As mentioned, the parameters of the adhesive force distribution have a significant effect on the calculated resuspension rate. The results of a limited sensitivity analysis are presented in Figure 5.5: solid lines refer to a reduction factor of 1000, whereas dashed lines to a factor of 100 (higher effective adhesive forces). A higher value of the reduction factor corresponds to substantially reduced adhesive forces due to higher surface roughness (i.e., interaction with a limited number of asperities). Thus, a higher reduction factor leads to particle resuspension at lower friction velocities, as shown in the two subfigures of Figure 5.5. Figure 5.5a shows model predictions obtained with an adhesion model without deformation, whereas Figure 5.5b shows results calculated with an adhesion model that incorporates elastic deformation. The calculations also shows that a higher adhesive-force spread leads to a wider range of friction velocities that give a non-zero particle fraction remaining on the surface. A higher spread implies a broader distribution of the adhesive forces, i.e., the surface exhibits significant variability of concavities. Even though the effect of the two parameters on the calculated resuspension rates (for the chosen parameters) is substantial, the conclusion that two resuspension regimes may be identified, one reproduced by an adhesion model with elastic deformation (weakly bound large particle resuspended at low friction velocities) and the other by a model without (strongly bound small particles resuspended at high friction velocities) remains valid.

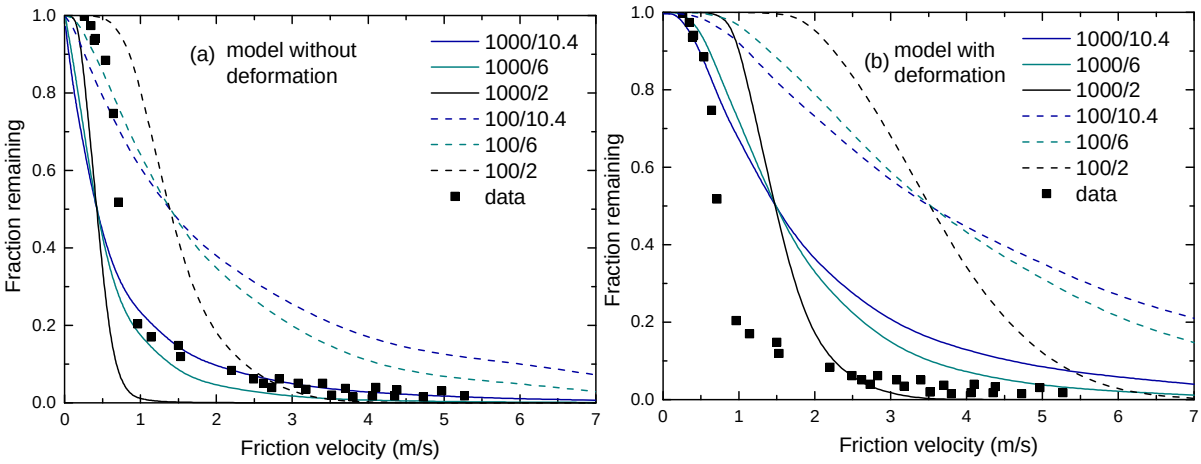

Figure 5.5: Sensitivity calculations for 10 µm alumina particles (Reeks and Hall 2001): a) Model simulations without elastic deformation for different parameters of the adhesive force distribution: spread (2, 6, 10.4) and reduction factor (100,1000), b) Model simulations with elastic deformation for different spread (2,6,10.4) and reduction factor (100,1000) in the adhesive force distribution.

The analyses of these experiments shows that even for slightly elastically deformed particles (transition regime according to the Tabor number), particle size in relation to roughness characteristics plays a dominant role on contact characteristics and, thus, on particle resuspension. At high friction velocities, where smaller particles resuspend, the adhesion contact approaches that of rigid bodies (DMT theory). At low friction velocities, where larger particles resuspend, elastic deformation becomes important in the description of the contact characteristics, just like the JKR theory predicts for large or soft particles.

5.8.3 Ibrahim et al. (2003) experiments

Ibrahim et al. (2003) conducted experiments to characterize particle detachment using stainless steel and glass particles on a glass substrate. The particles in these experiments resuspend completely at considerably lower friction velocities (< 1 m/s) than the particles in Reeks and Hall (2001) experiments (< 5.5 m/s). Consequently, the adhesive forces between the particles and the glass substrate in Ibrahim et al. (2001) were substantially smaller. A possible reason for resuspension at lower friction may be the size of the particles used, in conjunction with different surface properties and characteristics: the diameter range was 70 ± 6, 72 ± 4 and 32 ± 2 µm, which corresponds to substantially bigger particles with small diameter variation than the particles in from Reeks and Hall (2001) experiments. The aerodynamic force a particle experiences increases with particle size more rapidly than the adhesive force (different algebraic

dependencies on the particle radius). In addition, an increase in surface roughness (contact with few asperities) reduces significantly the adhesive force.

In the absence of data for the adhesive force distribution for these experiments we modelled them initially with the reduction and spread used in the Reeks and Hall (2001) data, Table 5.5 (1000, 10.4). However, the experimental data indicate a much narrowest adhesive force distribution; thus, they were modelled using a smaller value of the spread reflecting the limited variability in surface concavities due to the larger and more monodisperse particles.

Figures 5.6 and 5.7 present model results for 70 μm stainless steel particles, 72 and 32 μm glass particles respectively. It was found that a geometric standard deviation of 2 reproduces quite well the experimental data in agreement with Zhang et al. (2013) who used 1.7 for experimental data of lycopodium spores on a glass substrate (Ibrahim et al. (2001)). Good correlation was found for the stainless steel particles on a glass substrate (SS70 particles). For the glass particles (GL72 and GL32) the experimental data were in good agreement with modelled values when the reduction factor was also reduced (smaller reduction factor implies stronger adhesive force). Table 5.6 presents the values of reduction and spread used in the adhesive force distribution. The results confirm the importance of surface roughness in particle resuspension, and the necessity to choose judiciously the parameters in the adhesive force distribution to describe better the impact of surface roughness on adhesive forces.

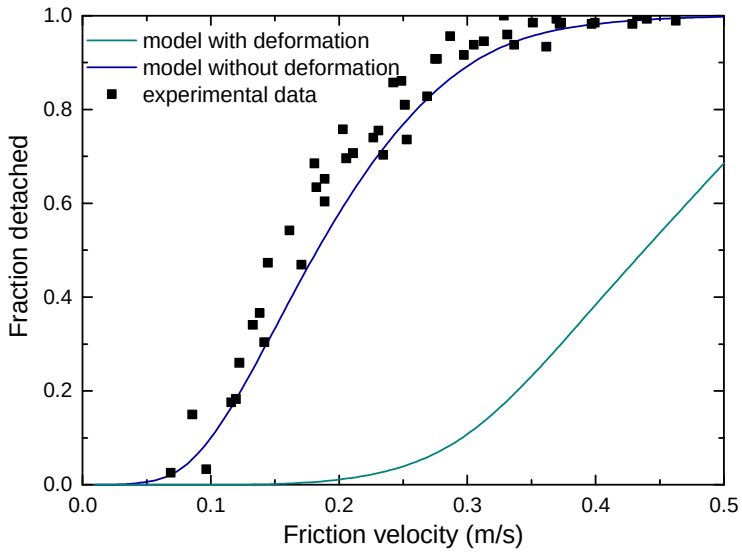

Figure 5.6: Comparison of model predictions with experimental data (filled squares) for 70 μm stainless steel particles (SS70) on a glass substrate (Ibrahim et al. 2003). Predictions using the adhesion model with elastic deformation are compared to predictions without elastic deformation.

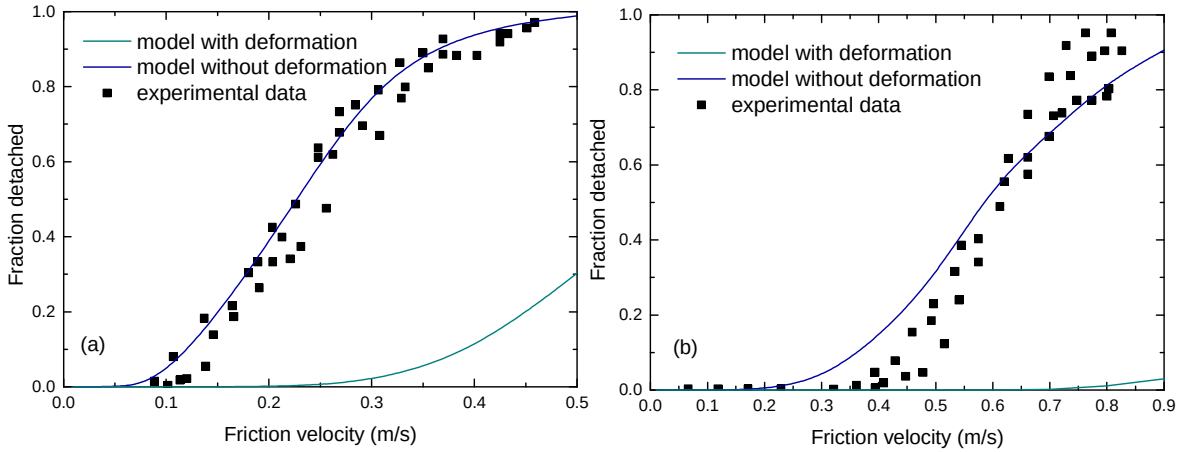

Figure 5.7: Comparison of model predictions with experimental data (filled squares): a) 72 μm glass particles (GL72), b) 32 μm glass particles (GL32) on a glass substrate (Ibrahim et al. 2003). Predictions using the adhesion model with elastic deformation are compared to predictions without elastic deformation.

Table 5.6: Reduction factor and spread of the adhesive force distribution used to model the experiments of Ibrahim et al. (2001) experiments.

Particles	Reduction, $\overline{R'}$	Spread, σ_a
SS70	1000	2
GL72	250	2
GL32	80	2

The results indicate that the model with the elastic deformation contribution underestimates significantly the resuspension rate for the whole range of friction velocities and for all cases. Unlike Reeks and Hall (2001) experiments only one regimes was identified depending on friction velocity. Model predictions were in good agreement in all three cases using only the model without particle deformation.

Inclusion of elastic flattening into the adhesion model leads to higher adhesion between the particle and the surface, thus, a reduced resuspension rate is calculated (smaller fraction of particles detached). The difference between the two models is substantial indicating that the model with elastic deformation does not reproduce the experimental data at all, even though the Tabor number is closer to the upper limit ($\mu = 5$), namely softer material, in all cases. Especially, for the 32 μm glass particles (GL32) the resuspension rate predicted with the model with elastic deformation is negligible (Figure 5.7b).

The deviation of the model predictions with elastic deformation (flattening) from the experimental data and the good agreement of the model without elastic deformation (for this set of data) renders manifest the importance of an appropriate modeling of the interaction of a particle with roughness of the surface.

Particle size together with the surface roughness the particle feels due to its size has significant impact on the choice of the adhesion model to be used (deformation or no deformation). Jiang et al. (2008) in measurements of particle entrainment, found that the effect of surface roughness depends significantly on particle size. In the present case, particle size and the effect of surface roughness on adhesion was considered in an effective way by modifying the particle-surface geometry. Whereas results were partially interpreted by referring to surface roughness and properties (height) of surface asperities, surface roughness was not explicitly modelled to deduce the contribution of surface asperities (small or large) to the total adhesive force. The results presented in Figures 5.6 and 5.7 imply that the relative monodisperse-in-size particles in the Ibrahim et al. (2001) experiments are big enough to rest on top of asperities (as depicted in Figure 5.1a), and be in contact with a surface characterized by a narrower distribution of adhesive forces ($\sigma_a = 2$). Such modeling of the geometry between the particle and the surface is in agreement with the experimental data when the particles sit on top of two asperities. On the other hand, the particle-surface geometry shown in Figure 5.1b considers that a common contact area is created between the particle and the surface, the surface seen by the particle appearing flat. This does not imply that surface roughness is ignored, only that the interaction may be effectively modelled by a smooth, elastic deformation, an effective interaction that does not reproduce the Ibrahim et al. (2001) experimental data. Therefore, particle size in relation to surface roughness characteristics is an important factor that determines which particle-surface geometry (and consequently adhesion model) is appropriate and whether the elastic deformation (flattening) is important in modeling contact characteristics during particle resuspension.

5.8.4 The effect of electrostatic forces

Typical particle charges corresponding to electrostatic forces found in nature are in the order of ~10^{-15} C (Feng and Hays 2003). Charges of the order of a few fC were chosen as input to the model, and Equation (31) was used to calculate the Coulomb force. The adhesion model was chosen to be without particle deformation (integrated Lennard-Jones potential without elastic flattening), since in the previously analyses we found good agreement with experimental data in most cases. Inclusion of particle deformation is expected to increase the adhesive force. Different particle sizes and charges were considered. The resuspension model was applied, as an example, to alumina particles on a stainless steel surface, as an example. A uniform charge on the particle surface was assumed. Figure 5.8a presents model results for 10 μm alumina particles on a stainless steel surface for different particle charges.

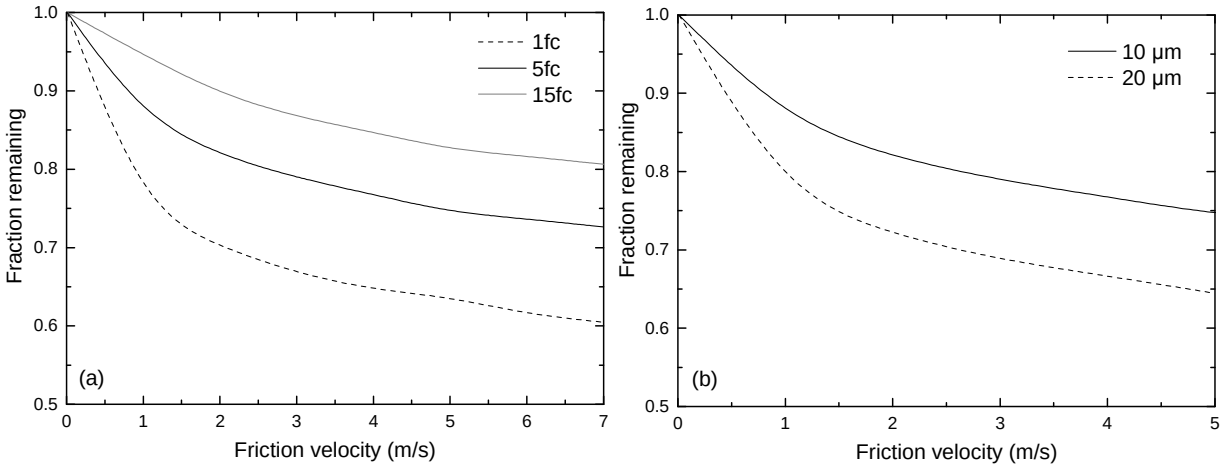

Figure 5.8: Fraction remaining of alumina particles on a stainless steel surface. a) Effect of particle charge for 10 µm particles and b) effect of particle size for a uniform particle charge of 5fC. The exposure time to flow is 1 s.

Figure 5.8a presents model results for 10 µm alumina particles on a stainless steel surface for different particle charges. It shows that as particle charge increases the fraction of particles that leave the surface decreases. The Coulomb force enhances the adhesive force, thus the particles are bound on the surface with higher attractive forces. The results are in agreement with other studies on the effect of charge on the adhesive forces (Zhou et al. 2003; Takeuchi 2006; Walton 2008). Increased removal forces are required to detach the particles from the surface. As a result, at friction velocity 7 m/s the fraction of alumina particles remaining on the surface is 0.60, 0.73 and 0.81 for 1, 5 and 15 fC respectively. Even for 1fC particle charge the fraction remaining on the surface is still high (0.6) implying that the electrostatic force provides a very strong force to the total adhesive force. Electrostatic forces contribute significantly to the adhesive forces (van der Waals forces) due to their longer range; thus, they have great impact on particle resuspension from a surface (Israechlavili 1992; Zhou et al. 2003; Walton 2008). Nevertheless, resuspension still predicted to occur, but at lower rates. The main reason is the reduction of adhesive and electrostatic forces by surface roughness. Experiments indicate that as surface roughness increases the enhanced adhesive force by the electrostatic force decreases (Takeuchi 2006).

To investigate the effect of surface roughness, a comparison of the adhesive and aerodynamic forces is presented. The Coulomb force for a smooth contact between a particle and the surface is given in Table 5.7. The total aerodynamic force that generates the lift and drag moments as generated by the turbulent flow (Equation 5.24) is listed in Table 5.8 for different friction velocities.

Table 5.7: Coulomb force for smooth contact and particle diameter 10 µm, Equation (5.30).

	1 fC	5 fC	15 fC
Coulomb force, C	$8.98\ 10^{-11}$	$2.24\ 10^{-9}$	$2.02\ 10^{-8}$

Table 5.8: Total effective aerodynamic force, Equation (5.24), corresponding to the moments of the lift and drag forces for a 10 µm particle.

Friction velocity, m/s	Total removal force, N
1	$9.61\ 10^{-8}$
2	$3.85\ 10^{-7}$
3	$8.66\ 10^{-7}$
4	$1.55\ 10^{-6}$

A simple force balance suggests that particle detachment occurs when the aerodynamic forces exceed the attractive forces (adhesive and electrostatic forces). Thus, in the values shown in Table 5.7 the adhesive force should be added. At the detachment point, where resuspension occurs, the balance of the forces was evaluated. For the 10 µm alumina particle on a stainless steel surface, the total intermolecular force, according to the van der Waal potential, was found to be 10^{-8} - 10^{-9} N. Similar values for van der Waals forces are also reported in other studies (Feng and Hays 2003; Takeuchi 2006). Considering that the attractive forces are stronger than the removal forces, it would be reasonable to think that particle detachment cannot occur for low friction velocities. However, the results in Figure 5.8a suggest that resuspension takes place. Accounting for surface roughness results in the reduction of all attractive forces by several orders of magnitude. Thus, the observed particle resuspension at lower friction velocities and higher electrostatic forces is a consequence of the stochastic nature of resuspension: for example, by the modification of the adhesive forces due to surface roughness and of the aerodynamic forces due to the turbulent bursts (e.g. ejections or sweeps of the fluid). However, higher particle charges corresponding to stronger electrostatic forces (> 15fC) are not easy to overcome and particle detachment is much slower.

The effect of particle size is shown in Figure 5.8b where a comparison between 10 and 20 µm alumina particles is presented. It can be seen that a 20 µm alumina particle resuspends more easily than a 10 µm alumina particle. The reasons are two-fold: larger particle size corresponds to higher removal forces (Equations (5.26, 27), R_p in the power of 4 and 2, respectively) and the electrostatic force is reduced (Equation (5.30), R_p at the denominator). Thus, for a given particle charge the resuspension rate increases with particle size.

Finally, a comparison between the model with and without the electrostatic force is presented in Figure 5.9. The particle charge was chosen to be 5 fC and the model was applied to 20 μm alumina particles. The predictions suggest that at 5 m/s all particles resuspend in the absence of electrostatic forces (as it was found in the experiments, Figure 5.3b), but a fraction of 0.64 remains when the electrostatic force is added. Resuspension is possible even in the presence of particle charge, but the rate is considerably reduced due to the strong adhering of particles on the surface by the electrostatic image force.

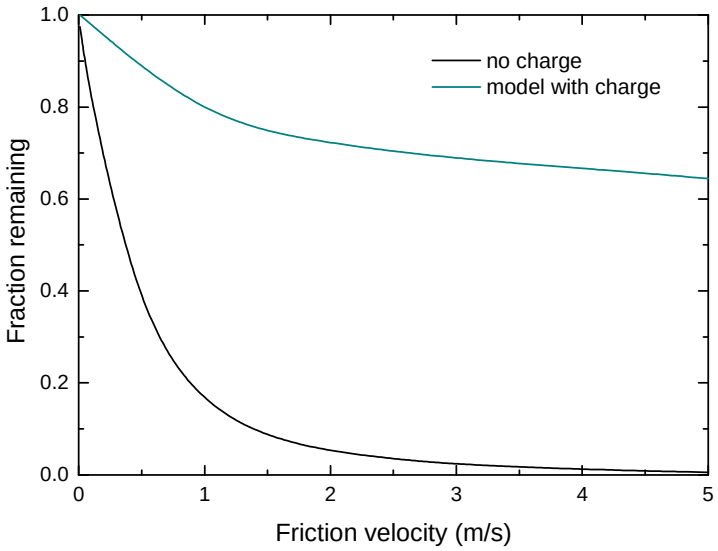

Figure 5.9: Comparison of model predictions without electrostatic force (as in Figure 5.3b) and with electrostatic force for 20 μm alumina particles on a stainless steel surface. Particle charge is 5 fC.

5.9 Multilayer resuspension

5.9.1 Kinetics of a multilayer deposit

An idealized description of the deposit is assumed, where k layers of the same identical particles are stacked on top of others. The total number of particles is assumed the same in each discrete layer and only the physical interaction between particles at different layers is considered. Figure 5.10a presents an example of the generalized deposit. The resuspension rate is calculated by the single-layer resuspension rates as shown in Section 5.4, where, each layer is described by a first-order kinetic equation.

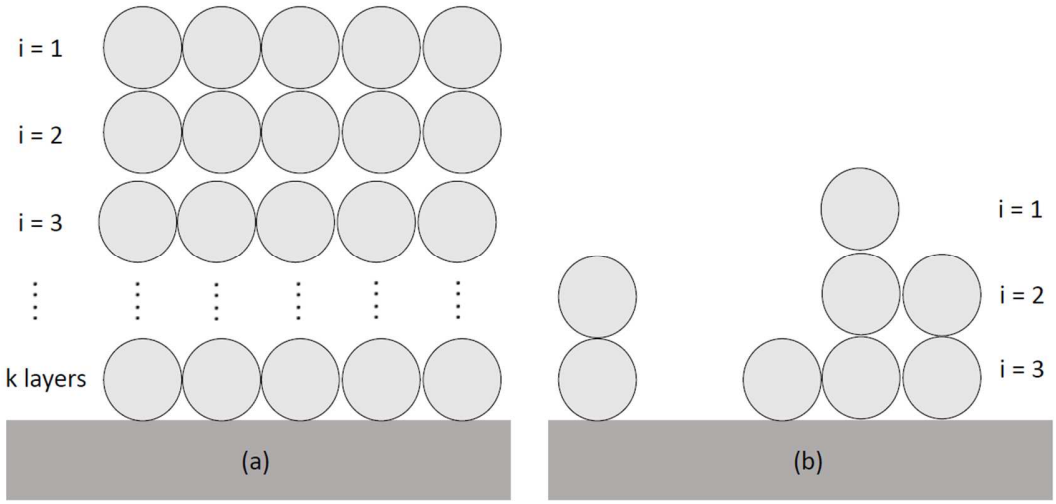

Figure 5.10: Geometry of particles in a multilayer deposit. a) Generalized deposit with k layers and b) a three-layer deposit with randomly resuspended particles.

Currently, two models exist for a multilayer deposit, the model proposed by Lazaridis and Drossinos (1998), LD and the model proposed by Friess and Yadigaroglu (2001), FY. Both models describe the time evolution of multilayer resuspension using a set of kinetic equations.

For a multilayer deposit of k layers with N_i particles in each layer, where, i represents the number of the layer and $i = 1$ corresponds to the top layer (exposed to the flow), the fraction of remaining particles p_i ($p_i = N_i(t)/N_i(0)$) at i th layer (for $i \geq 2$) at time t in each (i) layer is expressed for each model as:

$$\frac{dp_i}{dt} = -Jp_i\left[1 - \frac{p_{i-1}(t)}{p_{i-1}(0)}\right], (\mathrm{LD}) \tag{5.32}$$

$$\frac{dp_i}{dt} = -Jp_i\left[1 - \frac{p_{i-1}(t)}{p_i(t)}\right], (\mathrm{FY}) \tag{5.33}$$

whilst, the fraction of remaining particles for the top layer ($i = 1$, exposed to the flow) is described by a simple kinetic equation (Lazaridis and Drossinos, 1998):

$$\frac{dp_1}{dt} = -Jp_1 \tag{5.34}$$

where, J is the resuspension rate constant calculated by Equations (5.12). Equations (5.32) and (5.33) indicate that the only difference between the two models lies in the expression of the fraction of particles that are exposed to the flow (expression in the brackets). The LD model determines the fraction of exposed particles at i th layer as the fraction of particles that was removed from the above $(i-1)$ layer at time t. Thus, it implies that if a particle at i th layer is exposed, it is immediately resuspended. On the other hand, the FY model determines the fraction of exposed particles as the ratio of the particles in $(i-1)$th layer to the particles at i th layer at time t. Hence, the FY model represents the exposed particles at i th layer in relation to the layer above, $(i-1)$th.

Table 5.9 presents the fraction of exposed particles as it was calculated for both models based on the geometry presented in Figure 5.10b. It is demonstrated that the LD model calculates significantly higher fraction of exposed particles in both layers. The higher fractions found with LD model are associated with more particles detached at the same exposure time to the flow. Since, all fractions were derived from the same geometry, it is concluded that the LD model calculates the maximum resuspension rate.

Table 5.9: Fraction of exposed particles for layer 2 and 3 using the geometry in Figure 5.10b. Comparison between Lazaridis and Drossinos (1998) and Friess and Yadigaroglu (2001) expression for exposed particles.

Model	Layer 2	Layer 3
Lazaridis and Drossinos	$1-\frac{1/5}{5/5}=0.8$	$1-\frac{3/5}{5/5}=0.4$
Friess and Yadigaroglu	$1-\frac{1/5}{3/5}=0.67$	$1-\frac{3/5}{4/5}=0.25$

5.9.2 Analytical solutions of the differential equations

The fraction of remaining particles at time t for the first (top) layer is given:

$$p_1 = exp(-J_1) \tag{5.35}$$

where, J_1 corresponds to the resuspension rate constant at layer 1. Note that the resuspension rate constant J depends explicitly on the interaction system. Accordingly, the resuspension rate for a particle-surface interaction is different from a particle-particle interaction and the resuspension rate J between a particle-particle interaction is the same independently of the position of the layer. However, the fraction

of the remaining particles in each layer depends substantially on the kinetics, therefore, on the position of the layer in the deposit.

Consider a two-layer deposit on the surface (k = 2), the fraction of particles remaining on the first (top) layer is given by Equation (5.35), whereas, the fraction of particles remaining on the second layer is obtained from Equations (5.32) and (5.33) for LD and FY model respectively. Therefore, substituting the Equation (5.35) into Equations (5.32) and (5.33), the analytical solution for the second (bottom) layer is obtained:

$$p_2(t) = exp\left[-J_2 t - \frac{J_2}{J_1}(e^{-J_1 t} - 1)\right], (LD) \tag{5.36}$$

$$p_2(t) = e^{-J_1 t}\left(\frac{J_2}{J_2 - J_1}\right) + e^{-J_2 t}\left(1 - \frac{J_2}{J_2 - J_1}\right), (FY) \tag{5.37}$$

where, J_2 represents the resuspension rate for the second layer (particle-surface interaction).

In the case of a three-layer deposit (k = 3), the fraction of remaining particles is provided by Equations (5.32) and (5.33) for both second and third layer. However, in this case the resuspension rate J_2 at the second layer is equal to the resuspension rate J_1 at the first layer, since the interaction between layer 1/layer 2 and layer 2/layer 3 include only particle-particle interactions. Hence, J_2=J_1 and the analytical solutions for the LD and FY model, for the second layer are given:

$$p_2(t) = exp[-J_2 t - (e^{-J_2 t} + 1)], (LD) \tag{5.38}$$

$$p_2(t) = e^{-J_2 t}(1 + J_2 t), (FY) \tag{5.39}$$

The fundamental difference between Equations (5.36) and (5.37) and Equations (5.38) and (5.39) is that the latter depend only in one variable (J_2) because it includes interactions only between particles. Finally, the fraction of remaining particles for the bottom (third) layer for the two models is given:

$$p_3(t) = exp\left[-J_3 t - \frac{J_3}{J_2} e\gamma(1, e^{-J_2 t})\right], (LD) \tag{5.40}$$

$$p_3(t) = e^{-J_3 t}\left[1 - \frac{J_3}{J_3 - J_2} + \frac{J_3 J_2}{(J_3 - J_2)^2}\right] + e^{-J_2 t}\left[\frac{J_3}{J_3 - J_2}(1 + J_2 t) - \frac{J_3 J_2}{(J_3 - J_2)^2}\right], (FY) \tag{5.41}$$

where, J_3 represents the resuspension rate for the third layer and it includes the interaction between the particles and the surface.

The above equations (5.36-5.41) highlight the difference between the two models in respect to single-layer kinetics. The FY model is linear, whereas, the LD model is not. The linearity of FY model makes it easy to derive analytical solutions for more layers. On the contrary, the LD model is provided only for the first three layers (Lazaridis and Drossinos, 1998).

Additionally, for a four-layer deposit the first three layers are modelled using interactions only between particles. Hence, the resuspension rate J is the same for the first three layers and equal to J_3 (J_1=J_2=J_3). Using the FY model the get the expression for the third layer we obtain:

$$p_3(t) = e^{-J_3 t}\left(1 + J_3 t + \frac{J_3^2 t^2}{2}\right), (FY) \tag{5.42}$$

Equation (5.42) suggests that for any additional layer an additional term is also added in the analytic expression for the remaining fraction of particles (Equations 5.35, 5.39, 5.42), when the FY model is used. In fact, the analytic solution of FY model for more layers follows the expression:

$$p_n(t) = e^{-Jt}\sum_{i=0}^{n-1}\frac{(Jt)^i}{i!} \tag{5.43}$$

which, reflects a Poisson process for n layers. Note that n in Equation (5.43) represents only the layers with particle-particle interactions, thus, it is not valid for bottom layer where the interaction is modelled by a particle which is in contact with a surface. Therefore, it is demonstrated that multilayer resuspension is a random process both in time and space and that for infinitely thick deposits particles from n layers are resuspended with a constant rate J.

5.9.3 Characteristics of a two-layer deposit

Figure 5.11 presents the results of the model applied for a two-layer deposit of 70 μm stainless steel particles on a stainless steel surface using the LD kinetics. The first layer corresponds to the layer exposed to the flow (top layer), thus, the particle-particle interaction was modelled and Equation (5.35) was used for calculating the fraction of remaining particles on the surface. On the other hand, the second layer

corresponds to the bottom layer, thus, the interaction potential was modelled using the particle-surface interaction and the fraction of remaining particles was given by Equation (5.36).

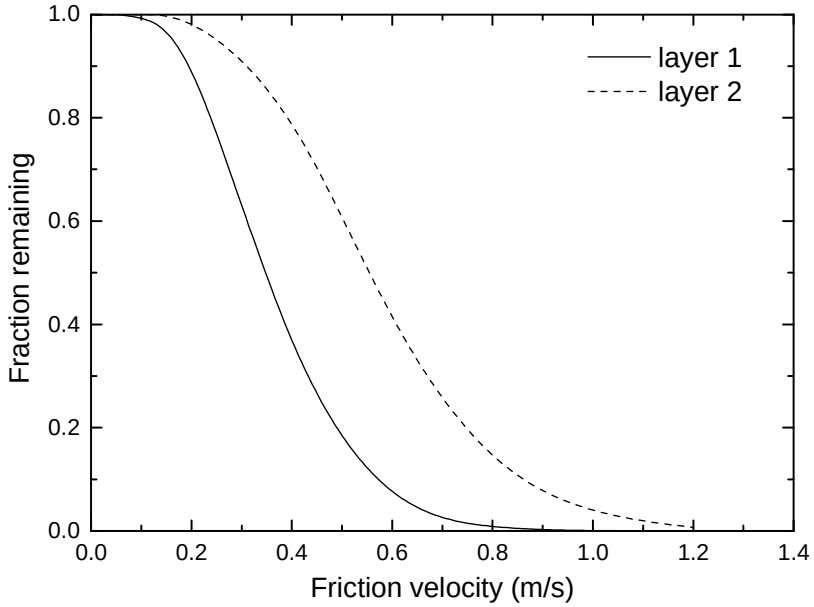

Figure 5.11: Fraction remaining of 70 μm stainless steel particles on a stainless steel surface versus friction velocity for a two-layer deposit. Model predictions using the LD kinetics. Standard deviation was equal to 2 and exposure time was equal to 1s.

The results suggest that the top layer (layer 1) resuspends first, followed by the resuspension of the bottom layer (layer 2). In reality, the conditions for detachment require the direct contact of the particle with the external force, herein the fluid flow. In other words, the particle in judgment is considered as possible for resuspension when the top of the particle is unobstructed e.g. is exposed to the flow. This hypothesis was adopted into the model by considering a particle from the bottom layer capable for resuspension only under the condition of an unoccupied position above it. The same methodology was adopted in Friess and Yadigaroglou (2002) and Lecrivain et al. (2014). Therefore, top layers are resuspended prior to bottom layers.

Multilayer resuspension depends strongly on particle position and by extend to the morphology of the deposit. However, particle resuspension is determined by the balance of forces that are required to entrain the particle to the ambient air and those that adhere the particles on the surface. Figure 5.12 presents a comparison between two different interactions: a particle-particle and a particle-surface interaction. The comparison is presented in the aspect of particle (stainless steel) resuspension, which is deposited either

on a layer of the same particles or on a stainless steel surface. The substrate and the particles were chosen of the same compound for comparable results. Moreover, both interactions involve a top layer kinetics but using the different approximations due to the different interaction potential.

Figure 5.12 demonstrates that stainless steel particles are detached with higher rates when the layer below corresponds to the same particles, whereas, higher friction is required to detach the same amount of particles when the layer below corresponds to a stainless steel surface. This finding is directly associated with the adhesion force. In fact, Figure 5.12 suggests that top layer resuspends easier than the bottom layer. Since, the only difference lies in the incorporation of the interaction potential, it is concluded that the adhesion force for a particle-surface interaction is stronger than the adhesion force between two layers of the same particles. The present finding is in agreement with Lazaridis and Drossinos (1998), where the authors simulated the interaction potential between two identical particles and between a particle and a surface and proposed that higher energy is required to overcome the threshold energy at equilibrium of a particle-surface interaction.

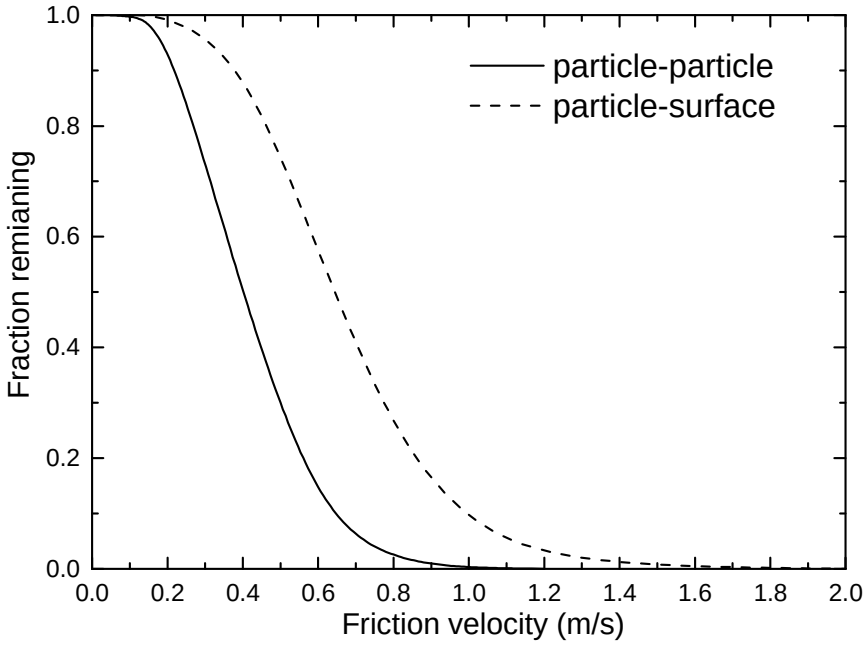

Figure 5.12: Fraction remaining of 50 μm stainless steel particles versus friction velocity. The bottom layer corresponds either to the same stainless steel particles (particle-particle interaction) or to a stainless steel surface (particle-surface interaction). Standard deviation was equal to 2 and exposure time was equal to 1s.

5.9.4 Comparison of different kinetics

A comparison of model predictions between the LD and the FY kinetics is shown in Figure 5.13. The results correspond to the second layer (particle-particle interaction) of a three-layer deposit, where, the fraction of remaining particles is plotted versus time. Equations (5.38) and (5.39) were used for LD and FY kinetics respectively.

Figure 5.13 indicates that the two models result in similar resuspension rates. In fact, the difference between the two models is minimal. In the short-term regime (10^{-3} – 1 s) the LD model presents slightly higher resuspension rate, however, in the long-term regime (1 – 10^{8} s) the two curves become identical. Although, the LD model reflects the maximum resuspension rate, our numerical results propose that in terms of a resuspension event the overall result remains the same.

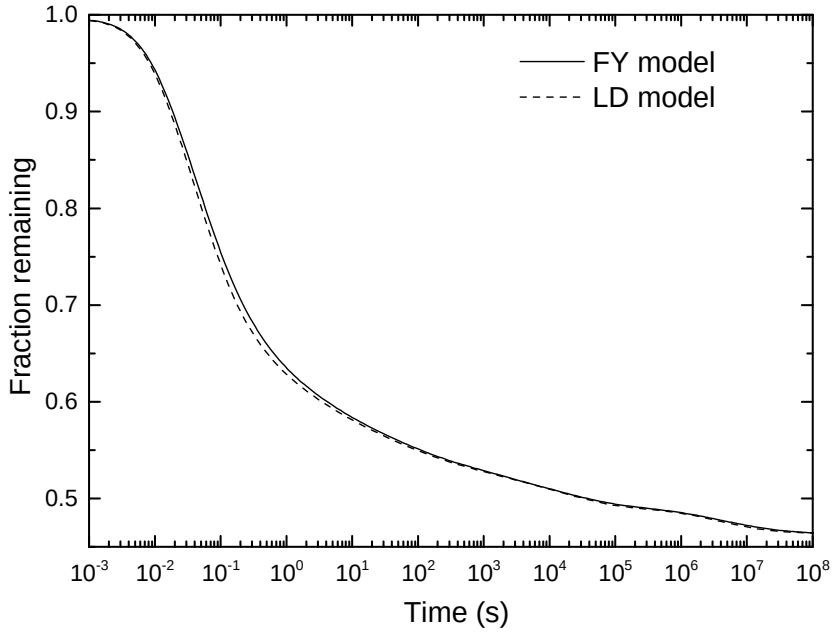

Figure 5.13: Comparison between LD and FY kinetics for the second layer (particle-particle) in a three-layer deposit of 20 μm alumina particles on a stainless steel surface for friction velocity 0.3 m/s. Standard deviation was chosen equal to 10.4.

In further investigation of the results, the two kinetics were examined in terms of mathematical solution using either Equation (5.38) or Equation (5.39). We found that the results for both kinetics depend strongly on the boundary conditions of the resuspension rate J. Let us consider two boundary conditions for the three-layer deposit presented here: a) $J_2 >> 0$ and b) $J_2 = 0$. Equations (5.38) and (5.39) are respectively:

$$p_2(t) = exp[-J_2 t - e^{-J_2 t} + 1], (LD)$$

$$p_2(t) = e^{-J_2 t}(1 + J_2 t), (FY)$$

In the case, where J_2 >> 0, the remaining fraction of particles, $p_2(t)$, becomes zero for both kinetics. Consequently, for significant high resuspension rates all particles are resuspended irrespectively of the kinetic that was used. On the other hand, when J_2 = 0 the remaining fraction of particles is equal to 1 for both kinetics, which is expected since zero resuspension rate physically corresponds to no particle resuspension ($p_2(t) = 1$). Thus, it is demonstrated that the two models provide the same results at the boundary conditions. The difference between the two proposed kinetics originate from the values of the resuspension rate J, which are between the boundary conditions and correspond to a few cases according to Figure 5.13.

5.9.5 Resuspension from multiple layers

Multilayer resuspension rate was modelled using the FY model. The latter was chosen because the linearity of the system makes simulation of multiple layers much easier. Figure 5.14a presents the results of the fraction of remaining particles for a 3-layer deposit. It indicates that top layers (1 and 2) resuspend at considerably lower friction velocity than the bottom layer (3). Layers 1 and 2 that correspond to particle-particle interactions are detached easier compared to the bottom layer due to the reduced adhesion force. The present results are in agreement with Boor et al. (2013b), which conducted resuspension experiments in wind tunnels and found that canopy layers were easier resuspended compared to surface (bottom) layer.

In addition, Figure 5.14a demonstrates a relationship of the resuspension rate with exposure time to the flow. Accordingly, two regimes are identified: a short-term regime where the resuspension rate is high and a long-term regime, where the resuspension rate decays algebraically with time. Our numerical results are in agreement with previous studies (Reeks et al. 1988; Lazaridis and Drossinos 1998; Reeks and Hall 2001; Friess and Yadigaroglu 2002), where the short-term resuspension decays almost exponentially with exposure time and the long-term resuspension rate found to depend inversely with exposure time. This behavior is strongly associated with the balance of adhesive and aerodynamic forces (Reeks et al. 1988; Friess and Yadigaroglu 2001; Benito et al. 2015). At small timescales the low adhered particles are instantaneously resuspended, since the particles experience higher aerodynamic than adhesion forces and

high rates are observed, however, at higher exposure times the fraction of strongly adhered particles on the surface increases and the resuspension rate decreases considerably.

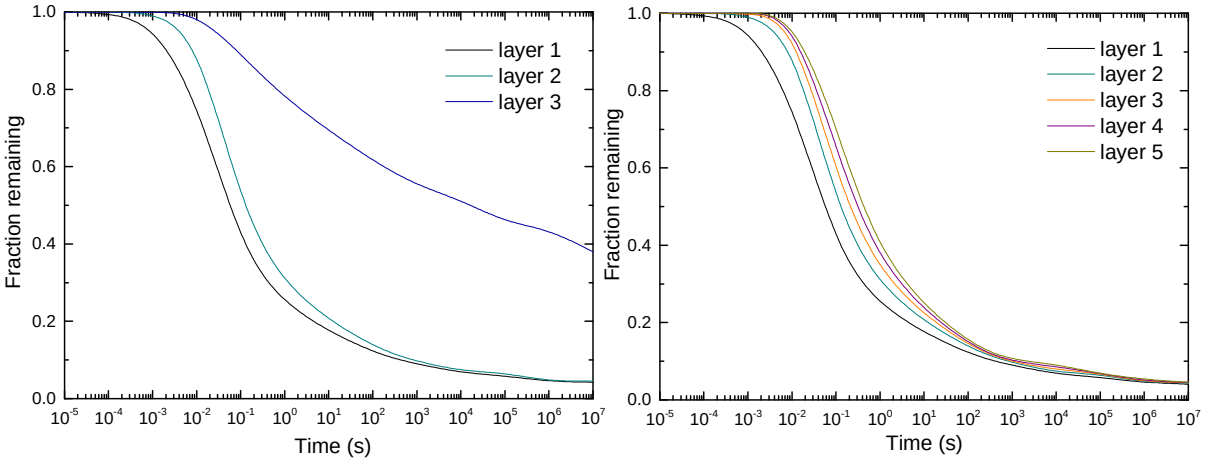

Figure 5.14: Fraction remaining of 50 μm stainless steel particles on a stainless steel surface at friction 0.5 m/s versus time for a) a 3-layer deposit and b) the first five layers in a 6-layer deposit. Standard deviation was chosen equal to 2.

Moreover, it is observed that top and bottom layers present a gap that increases with exposure time. Layers 1 and 2 that correspond to particle-particle interactions result in the same estimate of remaining particles, whereas, layer 3 that corresponds to a particle-surface interaction results in a higher estimate. Therefore, Figure 5.14a confirms the stronger adhesion force between the particles and the surface and is a reflection of model assumptions, that all layers that include particle-particle interactions involve the same adhesive force (but different kinetics). In fact, the model results suggest that irrespectively of the layer number in a multilayer deposit, a particle-particle interaction corresponds to the same adhesion. Thus, in terms of a long exposure to a constant fluid flow, the net result would indicate an identical remaining mass on the surface, since in the long-term regime all potentially resuspended particles are already removed.

Figure 5.14b plots the fraction of remaining particles for the first five layers in a 6-layer deposit. All interactions correspond to particle-particle interactions, thus the difference between each layer originates from the different kinetic used in each layer. It is demonstrated that after 10^3 s exposure (long-term) to the flow, all layers result at nearly the same remaining mass on the surface, where higher friction (removal force) is required to detach more particles. The results indicate that irrespectively of the layer number particle resuspension becomes identical for the first five layers in the long-term regime. Thus, for long

exposures and under the influence of a constant flow multilayer resuspension reaches a steady state condition characterized by a rate equal to J. On the other hand, for short-term regime, it is observed that as the layer number increases the difference between the layers becomes minimal, suggesting that for thicker deposits the resuspension rate at different layers becomes similar, although represented by different kinetic.

5.9.6 Fractional resuspension rate Λ(t)

5.9.6.1 Evolution of Λ(t) for a multilayer deposit

Figure 5.15 presents the evolution of the fractional resuspension rate with exposure time for a three-layer deposit. As seen previously, we can distinguish a short-term regime, where, the first (top) layer is characterized by the highest rates. Accordingly, all particles at the top layer are unobstructed from above thus free to resuspend as long as it is stochastically possible. However, Λ(t) at the second and third layer are substantially dependent on the layer above (layer 1 and 2 respectively). Therefore, a different behavior is observed: Λ(t) increases up to a maximum and later decreases inversely with time (long-term regime).

The increase of Λ(t) in short-term regime (10^{-5}-10^{-1} s) for layer 2 and 3 is associated with more particles detached from each layer as exposure time increases. Moreover, layer 2 is characterized by higher rates than layer 3 in short-term regime. As long as the number of detached particles increases from the top layer, the exposed particles at the second layer become more and the resuspension rate increases with time. Accordingly, the same condition applies for particles at layer 3. Thus, Λ(t) in the short-term regime is lower for higher layer number: particles at layers $i \geq 2$ require a short-time period in order to be uncovered. In general, for a thicker deposit it is expected that Λ(t) will preserve lower rates for higher layer number. Similar findings are reported in Zhang et al. (2013).

Additionally, Figure 5.15 implies a relationship of Λ(t) with the two regimes. Although, different behavior for the three layers is observed at short-term regime with Λ(t) strongly dependent on layer number, at long-term regime Λ(t) retains similar rates for all three layers. The results indicate that the fractional resuspension rate is independent of the layer position in the deposit at long-term regime. A common evaluation of the results presented in Figure 5.14a and the ones presented in Figure 5.15 indicates that layer 3, although characterized by significantly higher remaining mass on the surface, resuspends with rates almost equal to layer 1 and 2 in long-term regime. Obviously, after 10^{-1} s exposure time to the flow Λ(t) starts decreasing in all three layers such that particle resuspension evolves with the same reduced rate, whilst stronger adhesive force in layer 3 (particle-surface) and the reduction of unobstructed

positions from above results in higher remaining mass on the surface. Nonetheless, our numerical results imply that in long-term regime a steady state condition is reached where all layers experience similar Λ(t).

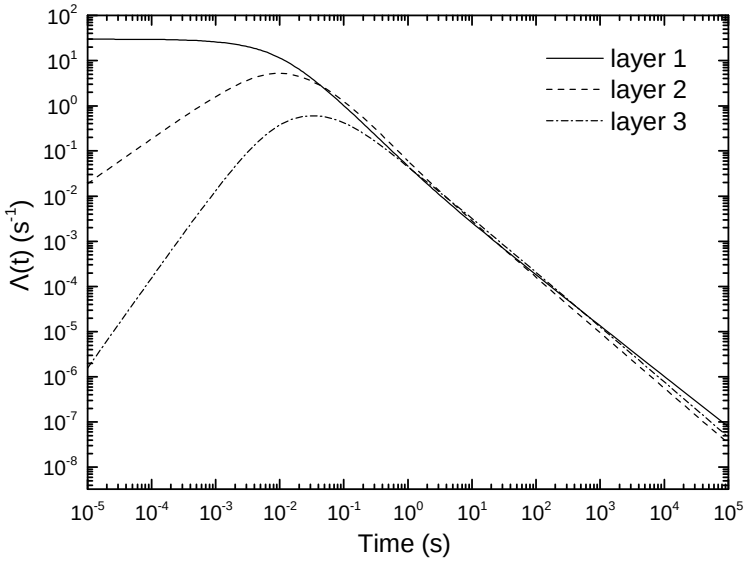

Figure 5.15: Fractional resuspension rate versus time for a three-layer deposit of 50 μm stainless steel particles on a stainless steel surface at friction 0.5 m/s. Standard deviation was chosen equal to 2.

5.9.6.2 Influence of exposure time and the $1/t$ *law*

Theoretical predictions (Wen and Kasper 1989; Reeks et al. 1988; Lazaridis et al. 1998; Reeks and Hall 2001; Friess and Yadigaroglu 2002) associate the long-term fractional resuspension rate with an inversely dependence on the exposure time to flow after an initial time. The inverse dependence of Λ(t) with time is shown in Figure 5.15, where, the fractional resuspension rate decreases linearly with exposure time for all three layers after a short time period corresponding to the short-term regime. The power law that determines the decay of the resuspension rate is in the form:

$$\Lambda(t) = constant\ t^{-\varepsilon} \tag{5.44}$$

where, ε represents the decay constant. Several authors have suggested that ε corresponds to values close to 1 (Wen and Kasper 1989; Lazaridis et al. 1998; Friess and Yadigaroglu 2002). Figure 5.16 presents the fractional resuspension rate versus exposure time for each layer of the three-layer deposit presented in Figure 5.15 and plotted for different friction velocities.

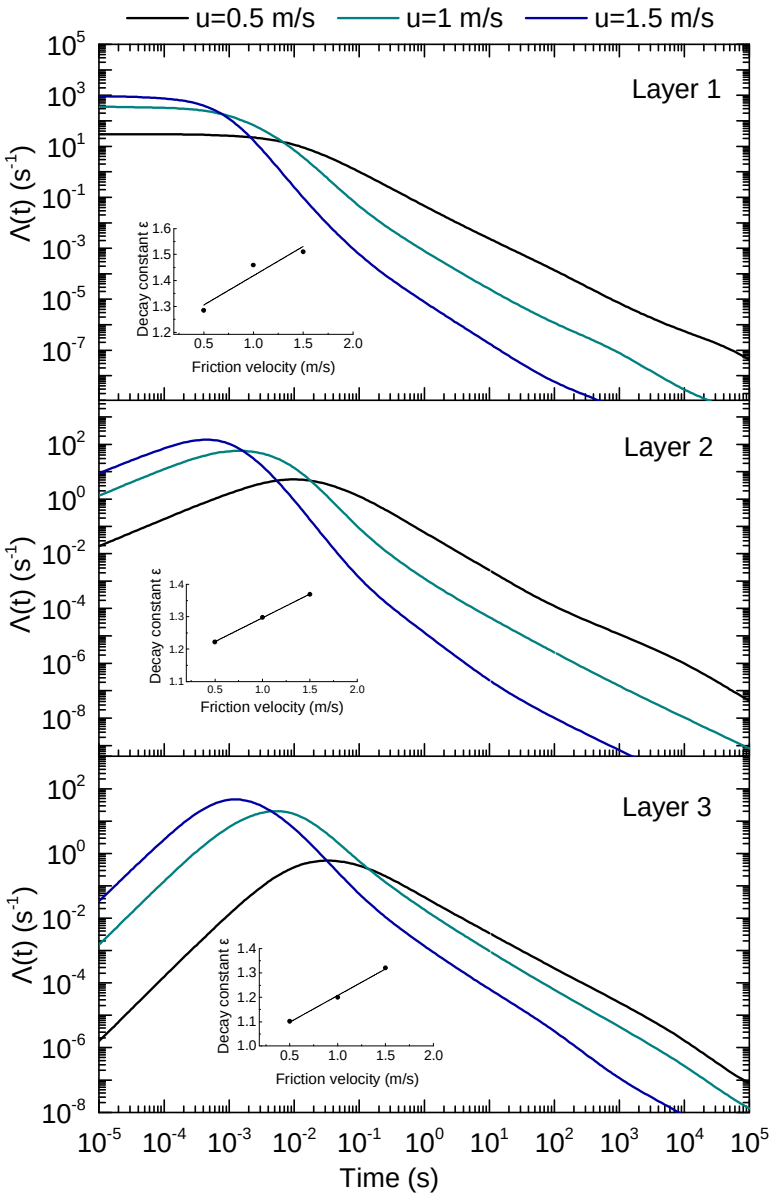

Figure 5.16: Fractional resuspension rate for each layer of a three-layer deposit of 50 μm stainless steel particles on a stainless steel surface versus exposure time. Comparison between different friction velocities. The inset represents the linear fit of ε with friction velocity. Standard deviation was chosen equal to 2.

At initial (short-term) resuspension particles resuspend with higher rates for higher friction due to enhanced aerodynamic forces represented herein by the friction velocity. However, at higher exposure time ($t > 10^{-2}$ s) $\Lambda(t)$ decays inversely with exposure time. Using Equation (5.44) to fit the numerical results of the model, values for ε were derived. Table 5.10 presents the fitted values of ε applied in Equation

(5.44) for each friction velocity and layer plotted in Figure 5.16. Our numerical results confirm the power law, although, the values of ε were scattered and usually above 1. Values higher than 1 are also reported in Benito et al. (2015). Hence, the present results indicate that the long-term fractional resuspension rate decays inversely with exposure time but with rates higher than the $1/t$law.

Moreover, Table 5.10 suggests that ε increases with friction velocity in all cases. It was found that the decay constant ε increases linearly with the friction velocity. The linear increase of ε with friction velocity is associated with enhanced decrease of the fractional resuspension rate at higher friction during long exposures. In other words, the remaining particles at long-term regime experience higher removal force at higher friction, hence, the resuspension rate decreases faster (at higher friction) since the particles that are possible for entrainment become fewer and as exposure time to the flow increases.

Table 5.10: Fitted values of the constant and ε of the power law (Equation 5.44) for each friction velocity in Figure 5.16.

Friction velocity, m/s	ε		
	Layer 1	Layer 2	Layer 3
0.5	1.285	1.222	1.102
1	1.459	1.298	1.200
1.5	1.511	1.369	1.321

5.9.6.3 Influence of friction velocity

In Figure 5.16 a swift between the curves is observed resulting in an inversion of the curves in the long-term regime. Although, higher friction corresponds to higher resuspension rate Λ(t) in short-term regime, the opposite behavior is found in long-term regime. Therefore, after long exposure to a flow, higher friction (aerodynamic forces) results in a significant decrease of the resuspension rate. Similar characteristic is reported in Benito et al. (2015), where the behavior of the curves was associated with the degree of the overlap between the aerodynamic and the adhesive force distributions.

In further investigation of the results, Figure 5.17 presents the dependence of the fractional resuspension rate with friction velocity at different standard deviations. It is demonstrated that Λ(t) presents a Gaussian distribution that reflects the adhesive force distribution. The resuspension rate is strongly related with the distribution of the adhesion force that the model incorporates to describe the distribution in magnitude and spread of the adhesive force between the particles. It also reveals the dependence of Λ(t) with friction velocity. The resuspension rate increases with friction velocity up to a maximum due to the higher removal force expressed by the friction but later it decreases since resuspension of particles becomes more

difficult. It is likely that the maximum in each distribution distinguishes the short- with the long-term regime. Then, the swift of the curves in Figure 5.16 is associated with the distribution of Λ(t) found in Figure 5.17. Although, at short-term regime Λ(t) increases with friction velocity, at long-term regime this behavior is inversed since all weakly adhered particles are already resuspended and the resuspension rate decreases substantially with higher friction velocity.

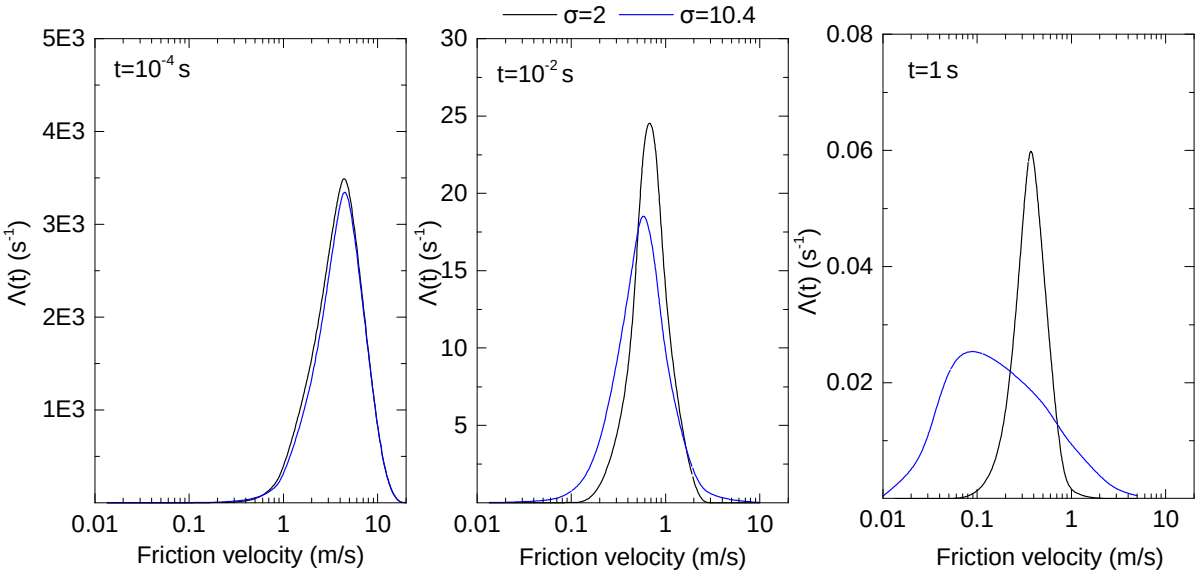

Figure 5.17: Fractional resuspension rate, Λ(t), of the top (exposed) layer of a two-layer deposit of 50 μm stainless steel particles versus friction velocity. Comparison between different standard deviations in adhesive force distribution at different exposure times.

Moreover, a comparison between different standard deviations is presented for exposure time 10^{-4}, 10^{-2} and 1 s. Figure 5.17 implies that the impact of σ_a becomes significant for higher exposure time, i.e. at long-term regime. At short-term regime (t=10^{-4} s) the two curves ($\sigma_a = 2$ or $\sigma_a = 10.4$) are almost identical, however, moving to higher exposure time results in a clear distinguish between them. At t=1 s, Λ(t) preserves a wider distribution with lower rates for $\sigma_a = 10.4$ corresponding to a broader distribution of adhesive forces. On the other hand, for $\sigma_a = 2$ the adhesive forces are considerably narrower and Λ(t) is characterized higher rates and a narrower distribution as well. These results indicate that σ_a has strong impact in the long-term regime probably because particles are more difficult to resuspend with the spread of the adhesive forces determine Λ(t), whereas, at short-term regime, where all weakly bound particles are easy detached the extend of the width of adhesive forces has minimal effect on Λ(t).

5.10 Conclusions

A stochastic model was adopted for particle resuspension by a turbulent flow and applied for a monolayer and a multilayer deposit. The model considered the interaction between the bodies (particle-particle, particle-surface) using the integrated Lennard-Jones potential. The particle-surface interaction was modelled with and without elastic deformation (flattening), whilst the particle-particle interaction was modelled only for rigid particles (no deformation). A kinetic approach was adopted to calculate the resuspension rate. The turbulence-induced aerodynamic removal forces were considered to arise from the joint contribution of the lift and the drag forces. The model also incorporated the reduction in adhesive forces due to surface roughness.

In the case of a monolayer deposit, particle resuspension was determined by force-balance approximations where the bound particle is detached when the moment of the lift and drag forces (generated by the flow) exceeds the adhesive force between the particle and the surface. Comparison with experimental data (Reeks and Hall 2001) identified the existence of two regimes. The first resuspension regime was characterized by particle resuspension at low friction velocities where elastic flattening was found to be significant for weakly (and large) adhered particles. The second regime was characterized by resuspension at higher friction velocities where the strongly (and small) adhered particles were modelled without the effect of particle deformation (no flattening). Results were interpreted by arguing that larger particles interact with a large amount of small-scale asperities: a common contact area is created as particles are considerably deformed (JKR theory). However, for smaller particles surface roughness becomes significant: particles rest on top of a small number of asperities and the surface contact characteristics may be reasonably approximated by those of a rigid body (DMT theory). The analysis of Ibrahim et al. (2003) suggested that the contact geometry is such that particles sit on top of two asperities. For the this set of experiments, the particles were larger and more monodisperse, in contact with a surface characterized by a considerably narrower distribution of adhesive forces. The roughness of the surface seen by the particles was best approximated by a rigid zone contact, and particles resting on top of asperities. The results summarized highlight the importance of particle size and the corresponding surface contact characteristics, in particular the interplay between particle size and surface roughness) in particle resuspension.

Evaluation of resuspension when electrostatic forces are present suggested that particles can be detached although the adhesive force is considerably enhanced due to particle charging. Even though the electrostatic force between the particle and the surface is strong, resuspension can occur under different

scenarios. The results showed that particle size and charge, along with surface roughness, contribute mainly to particle resuspension under the influence of a uniform charge on the particle surface.

In the case of a multilayer deposit, particle resuspension found to depend strongly on layer position in the deposit. Although, the single-layer resuspension rate was obtained by the same kinetic approach as in monolayer resuspension, particle resuspension is subject to its position in the deposit and an unobstructed cell from above is required in order to be detached. Therefore, top layers resuspend prior to bottom layers. Multilayer resuspension was also governed by two regimes depending on the time exposure to the flow. Accordingly, a short-term and a long-term regime was identified. The two regimes were associated with the adhesion force: at short-term regime higher rates applied for higher friction due to enhanced removal force and all weakly bound particles were instantaneously resuspended. On the other hand, at long-term regime only the strong adhered particles remained on the surface resulting in a substantially reduced rate, which, presented lower rates for higher friction. Finally, the numerical results imply that under steady flow conditions the resuspension rate at different layers becomes similar at long-term regime irrespectively of the layer number. Hence, it is suggested that the long-term regime corresponds to a steady state condition, where, multilayer resuspension evolves with similar rates at the different layers of the deposit.

Chapter 6

Modeling of particle resuspension due to surface vibration

6.1 Introduction

Particle resuspension may occur due to vibrational forces. In this case, the effect of the removal force on particles originates from the vertical vibration of the surface (mechanical displacement), which alters the conditions for detachment. In general, removal forces are size-dependent based on the removal mechanism, such that for air currents they have quadratic dependency and for vertical vibrations they have cubic dependency with particle diameter (Hinds 1999). Hence, it is expected that small particles are more difficult removed from a vibrational force compared to an airflow.

The present chapter employs a different approach for particle resuspension. Instead of a turbulent airflow acting upon the particles, resuspension is caused by surface vibration. In that sense, mechanical vibration is introduced through an external periodic force acting normal on a plate. Particle oscillations due to this external force are no longer parallel to the surface but free oscillations occur perpendicular. Implementation of the force causes deformation into the body of the plate, which propagates via elastic waves, namely bending waves. Local and spatial dependent displacements are sufficient to cause particle motion in a direction perpendicular to the surface as long as particle mass inertia is overcome.

The aim is to investigate the physical situation of particle resuspension under an external vibrating force. For this purpose, the theory of elasticity is implemented to get appropriate expressions for the displacement of the plate, which is responsible for particle displacement. The main goal is to determine the force whereby a particle oscillates when an external force is applied at distance R.

6.2 Bending waves as force propagator

The theory of elasticity describes the deformation of plates when an external force is applied on a body. The external force is considered to act normal on the surface and per unit area, hence, it can be expressed in units of pressure. Under the action of this force the body exhibits some deformation.

These deformations are considered small, thus, all the motions considered are small elastic oscillations. If the displacement is in the direction of the propagation (x direction), the wave is called longitudinal wave. On the other hand, if the displacement is perpendicular to the direction of propagation (y or z direction), the wave is called transverse wave.

Bending waves are the waves where the oscillations are perpendicular to the axis of the plate (z direction). For a plate of small thickness h, the wave length is large and the theory applies for finite media in the z direction but infinite extend in the x and y direction. Accordingly, the equation of free oscillations is given (Landau and Lifshitz 1986):

$$\rho h \frac{\partial^2 z}{\partial t^2} + \frac{E h^3}{12(1-\sigma^2)} \left(\frac{\partial^2}{\partial x^2} + \frac{\partial^2}{\partial y^2} \right)^2 z = 0 \tag{6.1}$$

where, E is the Young's modulus, σ is the Poisson's ratio, ρ is the material density of the plate, h is the plate thickness and z is the displacement in the z direction which depends on the x and y direction. Dividing with ρh, the propagation velocity of the wave is obtained from Equation (6.1) as:

$$c = \sqrt{\frac{E h^2}{12\rho(1-\sigma^2)}} \tag{6.2}$$

The problem essentially presented here is to determine the force that is required for a particle to oscillate in the z direction when a force is applied at distance R as shown in Figure 6.1.

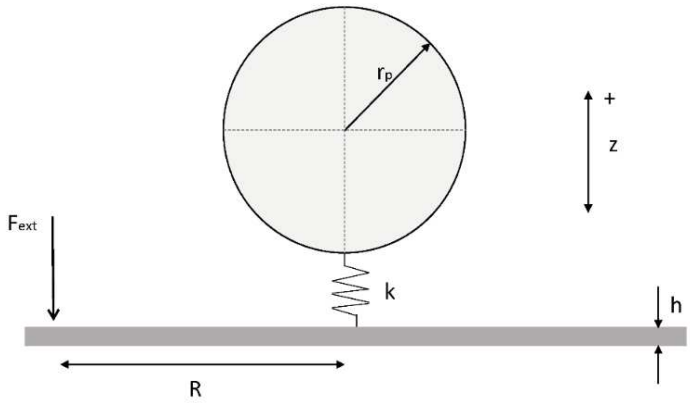

Figure 6.1: Model for particle oscillations.

The theory of elasticity is implemented to investigate particle resuspension caused by mechanical vibration. Accordingly, a driving term is added at the right hand side of Equation (6.1) to represent the external force applied on the surface. Recall that the theory applies in thin plates (z must be substantially smaller than x and y direction), thus plate thickness was assumed to be 1 cm in all subsequent calculations.

6.3 Condition for particle resuspension

The external force F_{ext} is the force that generates the waves and causes plate bending, i.e. infinitesimal oscillations in the body of the plate. Plate oscillations propagate according to the equation of motion described by Equation (6.1). The particle is assumed to be in static equilibrium before any motion begins and the force is assumed to apply at $t = 0$ and at distance R from the particle. Particle oscillations on the surface are considered by a simple harmonic oscillator of one-degree-of-freedom for a particle of a mass m_p and spring stiffness k (Figure 6.1).

Particle motion in the vertical direction (z) occurs due to momentum transfer from the plate. Herein, it is introduced through Newton's second law of motion for the particle ($F = ma$). Accordingly, a force is estimated, namely the force of oscillation, which corresponds to the force whereby the particle oscillates due to plate bending. Obviously, particle inertia due to its mass must be overcome, so the particle moves in the vertical direction. Hence, the force of oscillation is obtained as:

$$F_{osc} = m_p \frac{\partial^2 z}{\partial t^2} = \frac{4}{3}\pi r_p^3 \rho_p \frac{\partial^2 z}{\partial t^2} \tag{6.3}$$

where, r_p is the particle radius, ρ_p is the particle density, while the acceleration of the particle is derived from the second derivative of the displacement of the plate. Note that the particle is considered to follow the bending wave displacement since no other external force acts on it.

Particle resuspension due to this external applied force is manipulated deterministically in such a way that particle excitation is considered possible when the force of oscillation is higher than the adhesive force. The adhesive force was estimated by the JKR theory:

$$F_{adh} = \frac{3}{2}\pi \Delta\gamma r_p \tag{6.4}$$

When the force of oscillation exceeds the adhesive force the spring gets extended and eventually broken. Therefore, the particle will be resuspended when $F_{osc} > F_{adh}$.

6.4 Approximation of the force of oscillation

6.4.1 Approximation of the force of oscillation from an external force acting as a δ function in time and space

The first case involves a force that is applied instantaneously on the plate, thus, has the characteristic of the delta function both in time and in space. In practice, it acts once as a point force on the plate and preserves a peak value at the point of contact.

In consistency with the theory of elasticity, the force applied on the plate, F_0, is considered as a pressure, therefore, has the units of N/m^2. Appling the expression of this force in the right hand side of Equation (6.1), the equation of motion is obtained:

$$\frac{\partial^2 z}{\partial t^2} + \frac{Eh^2}{12\rho(1-\sigma^2)}\left(\frac{\partial^2}{\partial x^2} + \frac{\partial^2}{\partial y^2}\right)^2 z = -\frac{F_0}{\rho h}\delta(t)\delta(R) \tag{6.5}$$

where, the right hand side of Equation (6.5) corresponds to F_{ext}. The negative sign is used because the force is applied downwards, whereas, positive direction was considered upwards (Figure 6.1). Note that the quantity F_0/h represents the spatial force density (N/m^3). Expressing the solution of Equation (6.5) in Fourier space (k, ω), the displacement will be:

$$Z(R,t) = \frac{1}{(2\pi)^3}\int exp\left(i\vec{k}\vec{R}\right)dk \int exp(-i\omega t)z(k,\omega)d\omega \tag{6.6}$$

where,

$$z(k,\omega) = -\frac{a_0}{c^2k^4 - \omega^2} \tag{6.7}$$

where, a_0 ($a_0 = F_0/\rho h$) represents the acceleration of the body (herein plate) at a specified point and c is the propagation velocity (Equation 6.2). Translating Equation (6.6) back in (R,t) we obtain:

$$Z(R,t) = -\frac{1}{(2\pi)^3}\int exp(i\vec{k}\vec{R})dk \int_{-\infty}^{+\infty} exp(-i\omega t)\frac{a_0}{c^2k^4-\omega^2}d\omega \tag{6.8}$$

The frequency integral can be solved explicitly (Dennery and Krzywicki, 1996), while, selecting the angular direction in polar coordinates the first derivate can be solved. Importing these modifications into Equation (6.8), the final expression for the displacement will be:

$$z(R,t) = -\frac{a_0}{2\pi c}\int_0^{\infty}\frac{J_0(kR)\sin(ck^2t)}{k}dk \tag{6.9}$$

This is the displacement of the plate at distance R and time t due to the force applied on the surface of the plate, where, J_0 is the Bessel function of the zero-th order. Using Equation (6.3), the force of oscillation will read:

$$F_{osc}(R,t) = \frac{\rho_p}{\rho}\frac{2F_0r_p^3c}{3h}\int_0^{\infty} J_0(kR)\sin(ck^2t)\,k^3dk \tag{6.10}$$

F_{osc} has been taken positive upwards, in accordance with the direction of the plate displacement. Note that if the particle and the plate are made of the same material, the densities are simplified in Equation (6.10).

The present case involves an instantaneous force localized both in time and in space. For a more realistic point of view of the physical situation, the following subsections present a complete relaxation of both time and space constraints by substituting the δ function in time and space domain respectively.

6.4.2 Approximation of the force of oscillation from an external force acting as a function periodic in time and as δ function in space

Introducing a periodic function in the time domain but maintain the δ function in the space domain, will in practice produce an external vibrating force that still acts pointwise on the surface. This is a more realistic case, since it involves forces that cause harmonic oscillations of a specified frequency. Hence, the expression for the driving term will be in the form:

$$F_{ext} = F_0\cos(\omega_0 t)\delta(R) \tag{6.11}$$

where, the periodic term is represented by the sinusoidal driving term and F_0 represents again the pressure (N/m^2) that is applied on the plate surface. Substituting Equation (6.11) in the right hand side of the equation of motion (Equation 6.1) and solving for the displacement z, will produce:

$$Z(R,t) = -\frac{2\pi a_0}{2i(2\pi)^3}\int exp\left(i\vec{k}\vec{R}\right)dk\, exp(-i\omega t)\frac{\delta(\omega+\omega_0)-\delta(\omega-\omega_0)}{c^2k^4-\omega^2}d\omega \tag{6.12}$$

Using the appropriate transformations, the equation for the plate displacement in distance R and time t is given:

$$z(R,t) = \frac{a_0}{4\pi\omega_0 c}\cos(\omega_0 t)\left[\frac{\pi}{2}N_0\left(\sqrt{a}\right)+K_0\left(\sqrt{a}\right)\right] \tag{6.13}$$

where, N_0 and K_0 are the Neumann and Modified Bessel functions of the second kind respectively, and a is a quantity equal to $a = R^2\omega_0/\mathrm{c}$. Using the same methodology as previously, the force required for particle oscillation will be the second derivate of the displacement multiplied by the particle mass:

$$F_{osc}(R,t) = \frac{\rho_p}{\rho}\frac{F_0 r_p^3\omega_0}{3hc}\cos(\omega_0 t)\left[\frac{\pi}{2}N_0\left(\sqrt{a}\right)+K_0\left(\sqrt{a}\right)\right] \tag{6.14}$$

6.4.3 Approximation of the force of oscillation from an external force acting as a function periodic in time and Gaussian in space

In the present section the delta function in the space domain is substituted by a Gaussian function. This is a fundamentally different approximation compared to the previous two by a physical point of view, since, the force is assumed to preserve a spatial (Gaussian) distribution on the surface. Therefore, it peaks at the point of contact but is not a point force. Moreover, we do not associate any force density with the pressure and F_0 will now represent the maximum pressure at the point of contact. Thus, the external force will be in the form:

$$F_{ext} = F_0\cos(\omega_0 t)exp\left(-\frac{bR^2}{2}\right) \tag{6.15}$$

where, b is the dispersion parameter of the Gaussian function.

The dispersion parameter characterizes the width of the distribution, i.e. the extend of the applied force in the region around the central point. In the Fourier space it is defined as $b = 1/characteristic\ length^2$. The characteristic length retains an appropriated value defined by the thickness of the plate, thus, the characteristic length scale here is assumed as 1 cm. Although, model formulations were cancelling out the use of characteristics scales in the previous cases, in the present case it is necessary to divide with these scales and get the relevant pressure values. Note that for $b \longrightarrow \infty$, the width of the distribution becomes smaller (narrow distribution) so that the exponential function approaches $\delta(R)$, which takes us back to the previous analysis for the applied force (subsection 6.4.2).

Again, substituting Equation (6.15) to the right hand side of the equation of motion (Equation 6.1) and using the Fourier analysis we get the displacement of the plate per unit surface:

$$Z(R,t) = -\frac{a_0}{2\pi b}\cos(\omega_0 t)\int_0^\infty \frac{J_0(kR)e^{-\frac{k^2}{2b}}k}{c^2k^4 - \omega_0^2}\,dk \tag{6.16}$$

Adopting the same methodology for the calculation of the force· the force of oscillation per unit surface will now be:

$$F_{osc}(R,t) = \frac{\rho_p}{\rho}\frac{2F_0 r_p^3 \omega_0^2}{3bh}\cos(\omega_0 t)\int_0^\infty \frac{J_0(kR)e^{-\frac{k^2}{2b}}k}{c^2k^4 - \omega_0^2}\,dk \tag{6.17}$$

Hence, in order to retrieve the displacement of the plate and the force of oscillation of the particle, one should multiply with the characteristic scales.

6.5 Adhesive force distribution

Resuspension from surfaces is easier attainable due to surface roughness because it reduces considerably the adhesive force between the particle and the surface. Therefore, a more realistic approach of the present problematic would be to incorporate the surface roughness into the estimation of the adhesive force. A widespread way is to use a log-normal probability density function:

$$PDF = \phi(r_p')dr_p' = \frac{1}{(2\pi)^{1/2}\ln\sigma_a} exp\left\{-\frac{1}{2(\ln\sigma_a)^2}\left[\ln\frac{r_p'}{\overline{r_p'}}\right]^2\right\} d(\ln r_p') \quad (6.18)$$

where, $r_p' = r_{eff}/r_p$ is the normalized particle radius due to surface roughness (r_{eff} is the effective particle radius corresponding to the reduced adhesive force and r_p is the radius of a perfectly smooth particle), $\overline{r_p'}$ is the geometric mean of r_p' representing the reduction in adhesive forces and σ_a is the standard deviation representing the spread in adhesive forces.

Generally, both variables depend substantially on surface characteristics, therefore they define the reduction of the adhesive force. A good approximation for the geometric mean and the standard deviation was derived from Chapter 5 at 1000 and 10.4 for reduction and spread respectively, and were adopted herein as well.

6.6 Displacement of the plate

Consider a pressure of 100 N/m^2 of period 1 s that acts normally on the plate surface. The displacement of the plate in the z direction under this pressure is obtained as a function of the distance R and at time t from the contact point. Essentially, two cases were examined which correspond to a more realistic case for particle resuspension due to surface vibration (sinusoidal driving force and Gaussian distributed sinusoidal driving force) applied for a stainless steel and a glass plate. Table 6.1 lists the material properties used for each plate.

Table 6.1: Material properties.

Material	ρ (kg/m^3)	σ	E (10^{10} N/m^2)	$\Delta\gamma$ (J/m^2)
Stainless steel	8000	0.29	21	0.15
Glass	2400	0.27	8	0.4

Figure 6.2 presents the free oscillations of the plate for two different approximations of the driving force. It is observed that the two cases result in a rather similar magnitude (10^{-3} m) of the displacement, although a slightly higher displacement was obtained for the Gaussian distributed sinusoidal force for distances close to the point under stress. In addition, both approximations present a smooth reduction of the displacement as the distance from the contact point (0,0) increases. Eventually, for a distance far away

from the point of contact the displacement of the plate approaches zero values. By physical point of view free oscillations of the plate become minimal, thus, no oscillatory motion is any longer observed.

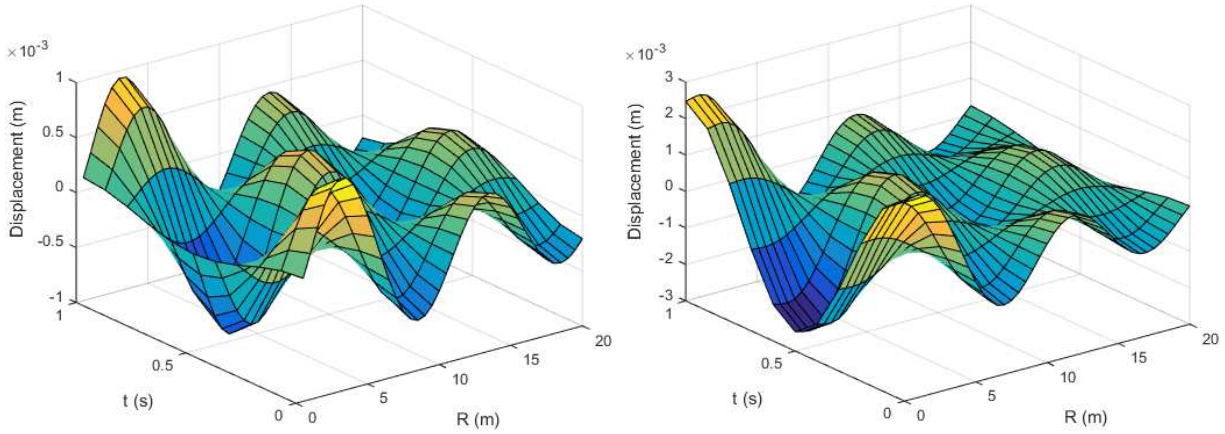

Figure 6.2: Displacement of a stainless steel plate at distance R and time t from the contact point (0,0) for a sinusoidal driving force (left plot-case 2) and a Gaussian distributed sinusoidal driving force (right plot-case 3). Pressure of 100 N/m^2 and period 1 s.

Moreover, material properties define the elasticity of the plate, thus, a hard material is expected to bend more difficult than a softer material. This case is presented in Figure 6.3, where, the displacement of a glass plate in the z direction is plotted as a function of distance R and time t for a sinusoidal driving force. It can be observed that bending of a plate made of glass is easier than that of the plate made of stainless steel (Figure 6.2, left plot) under the same stress because it exhibits higher oscillations (3 10^{-3}). This is mainly attributed to the hardness of the stainless steel (dense material, higher Young's modulus), whereas, a glass plate is softer and preserves higher oscillations.

Besides material properties, model variables with the most dominant effect on the plate bending are the magnitude and the period of the applied force. In practise, both variables define the characteristics of the applied force, thus the extend of the external force. Therefore, the choice of appropriate values for these variables determines the displacement of the plate. While, a value for the pressure F_0, depends on the type of the force that needs to be modelled (e.g. electric drill, human walking) and the range of F_0 has in practice no defined limits, the same does apply for the period T. In principle, the propagation of elastic waves in thin plates demands infinite extend in the x and y direction, where, the wave length λ is large compared to the thickness of the plate, $\lambda \gg h$. Accordingly, the equation of free oscillations (Equation 6.1) is applicable under this boundary condition. Hence, in order to apply the analysis presented in Section 6.4

the condition $\lambda \gg h$ has to be ensured. Table 6.2 presents the cases under which the driving period T of the applied force corresponds to the above criteria.

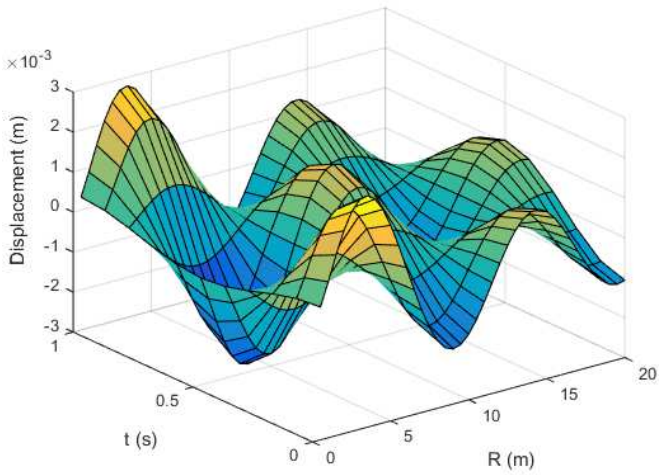

Figure 6.3: Displacement of a glass plate at distance R and time t from the contact point (0,0) for a sinusoidal driving force (case 2). Pressure of 100 N/m^2 and period 1 s.

Table 6.2: Conditions at which the driving period is accepted. The velocity of propagation (Equation 6.2) corresponds to a stainless steel plate of thickness 1 cm.

Plate thickness h, m	Velocity c, m\s	
0.01	15.45	
Period T, s	Wave length λ ($\lambda = cT$), m	Condition $\lambda >> h$
0.001	0.016	No
0.01	0.155	Yes
0.1	1.545	Yes
1	15.45	Yes
10	154.54	Yes

Table 6.2 suggests that the condition $\lambda \gg h$ is valid for a driving period of the external force at least 0.01 s. Recall that the velocity of propagation is a function of the material properties and the plate thickness. Hence, for the same plate the wave length depends only on the driving period. These results imply that the theory applies for a rather large period or small frequency of vibration. Moreover, the conditions presented in Table 6.2 obtained for a specific case (stainless steel plate, thickness 1 cm), however, generalization of the above results can be incorporated for other materials and conclude at the same finding: the frequency of vibration in thin plates is necessary to maintain small values in order implement the theory of bending waves.

6.7 Force of oscillation

Consider the same force that was applied on the plate in Section 6.6. The force of oscillation that the particle experiences is the force required to overcome the particle mass inertia, hence, the force at which the particle oscillates in the z direction caused by the plate displacement. Figure 6.4 presents the estimated F_{osc} for a 20 μm stainless steel particle on a plate of the same material under a sinusoidal (left plot) and a Gaussian distributed sinusoidal (right plot) applied force. It is easily seen that F_{osc} maintains the opposite direction from the displacement field (Figure 6.2) in both cases, however this is due to the negative sign used for the external force F_{ext} in the equation of motion. More importantly, Figure 6.4 suggests that the force of the oscillatory motion of the particle is substantially reduced (10^{-13} N) compared to the applied pressure F_0 (100 N/m^2) on the plate. These results indicate that momentum transfer through bending waves displacement creates a field where higher forces obtained close to the point of contact and that the force applied on the plate propagates but with several order of magnitude lower depending on particle size. Leung et al. (2013) also observed that high forces of several orders of magnitude are required in order to detach micron-sized particles in a vibration experiment, which is consistent with the theoretical predictions presented here.

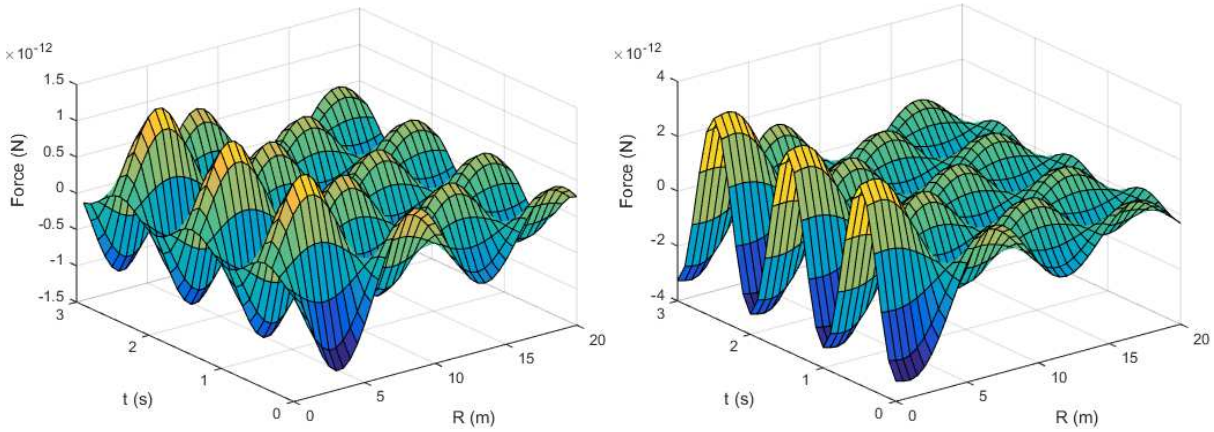

Figure 6.4: Oscillation force exerted on a 20 μm particle as a function of distance R and time t. Left plot correspond to a sinusoidal pressure of 100 N\m^2 and period 1 s (case 2). Right plot corresponds to a Gaussian distributed sinusoidal pressure of 100 N\m^2 and period 1 s (case 3). Plate and particle made of stainless steel.

In addition, applying a Gaussian distributed sinusoidal force results in higher oscillation force compared to a sinusoidal force. This is attributed with the displacement obtained in each case previously (Section 6.6),

and indicates that applying a Gaussian distributed force in the space domain results in higher oscillation force for distances close to the contact point. However, in larger distances both approximations result at approximately the same force.

The oscillation force for a 20 μm glass particle on the same stainless steel plate under a sinusoisal driving force is shown in Figure 6.5. It indicates that the force decreases by one order of magnitude compared to a stainless steel particle of the same size. These reuslts imply that particle mass inertia is more difficult to overcome for a more dense material (stainless steel) because the vibrating force created by the plate bending has to exceed the threshold of particle inertia.

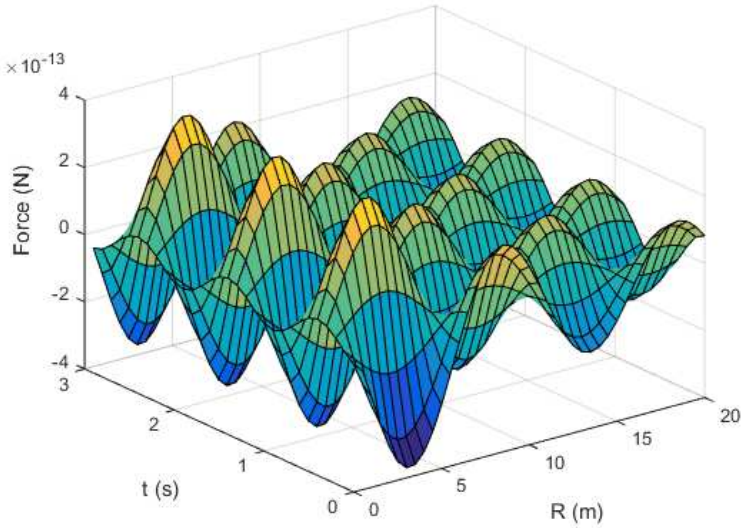

Figure 6.5: Oscillation force exerted on a 20 μm glass particle on a stainless steel plate as a function of distance R and time t for a sinusoidal pressure of 100 N\m^2 and period 1 s (case 2).

6.8 Particle resuspension

In the previous sections, the displacement of the plate and the force of oscillation were derived for a particle when an external force was applied on the surface of a thin plate at a distance R. Particle resuspension due to this external vibrating force was investigated using the condition as described in Section 6.3.

Table 6.3 presents several cases where the possibility of resuspension was examined, when a sinusoidal driving force was applied on the surface. The adhesive force was estimated using Equation (6.4) with and without the effect of surface roughness and is compared with the oscillation force due to plate bending.

According to Table 6.3 almost no case results in resuspension, if surface roughness is not incorporated when estimating the adhesive force, since $F_{osc} < F_{adh}$. Although, inclusion of the surface roughness reduces substantially the magnitude of the adhesive force, the force balance method suggests that resuspension is possible for larger particles or for higher applied forces, while approaching high frequencies. Recall, that the reduction in the adhesion force depends on the characteristics of the adhesive force distribution, however, the results presented here are representative of the effect of surface roughness.

Table 6.3: Possibility of resuspension under different scenarios for a sinusoidal driving force (case 2). Particle and plate made of glass.

Particle diameter (μm)	T (s)	F_0 (N/m^2)	F_{adh} (N)	F_{adh} PDF (N)	F_{osc} (N)	Possibility of resuspension
50	1	100	10^{-5}	10^{-9}	10^{-11}	No
100	1	100	10^{-5}	10^{-8}	10^{-10}	No
1000	1	100	10^{-4}	10^{-7}	10^{-7}	Possible
50	0.01	100	10^{-5}	10^{-9}	10^{-9}	No
100	0.01	100	10^{-5}	10^{-8}	10^{-8}	Possible
1000	0.01	100	10^{-4}	10^{-7}	10^{-5}	Yes
50	0.01	1000	10^{-5}	10^{-9}	10^{-8}	Yes
100	0.01	1000	10^{-5}	10^{-8}	10^{-7}	Yes
1000	0.01	1000	10^{-4}	10^{-7}	10^{-4}	Yes

The effect of the driving period has already discussed in terms of application of the bending waves theory. However, the driving period or frequency of the applied force has significant impact on the outcome as it is seen in Table 6.3. Small period (or high frequency) favors the possibility of resuspension because it increases the amplitude of particle oscillation upon the surface and the state of resonance can be potentially reached. However, the physical situation of the present application (Table 6.2) prevents the use of higher frequencies.

The natural frequency of vibration, ω_p, for the under study system was estimated (Lazaridis et al. 1998) approximately in the order of 10^8 s^{-1} suggesting that ω_p is at least five orders of magnitude higher than the upper limit of the driving frequency (10^2 s^{-1}). Even though, there is a significant difference between the two frequencies and in practice resonance cannot be reached, the physical problem is essentially captured, therefore, small driving period must be applied in order to enhance particle resuspension.

In addition, particle size has significant impact in resuspension. An increase in particle diameter results in an increase in the magnitude of F_{osc}. Higher particle size corresponds to stronger particle inertia due to its mass, thus a bigger particle is expected oscillate with higher force. Moreover, higher particle size corresponds to stronger adhesive force but an increase in the particle radius has greater effect on F_{osc} than on F_{adh}. Note that the adhesive force is proportional with r_p (Equation 6.4), while, the oscillation force is proportional with r_p^3 (Equation 6.14 or 6.17). The results in Table 6.3 indicate that the adhesive force increases one order of magnitude while considering a particle of 1000 μm. On the contrary, the oscillation force increases by several (3-4) orders of magnitude for the same particle size. Consequently, higher particle size favors resuspension because detachment form the surface is easily attainable because adhesives forces are easier to overcome compared to a smaller particle.

Higher pressure F_0 also results in higher F_{osc} because the magnitude of the external force is increased, therefore resuspension is easier. A comparison between the cases where T=0.01 s, shows that the condition $F_{osc} > F_{adh}$ is approached easier when the applied pressure is 1000 N/m^2. Higher pressure is expected to increase the likelihood for resuspension, whereas, smaller (100 N/m^2) results in a rather certain outcome depending on the conditions (particle size or driving period). Herein, no specific limits for F_0 were obtained, thus, the magnitude of the applied force depends on the physical situation that is under study. Human walking or running for example can reach values equal to a force of 1000 N/m^2 or even higher, whereas, several industrial applications (drill, laser beam) can cause vibration on a surface of reduced pressures.

6.9 Conclusions

Particle resuspension due to surface vibration was investigated. Accordingly, an external vibrating force was assumed to apply normal on the surface of a thin plate and at distance R from the particle. The vertical displacement of the plate was determined both in space and in time adopting the theory of elasticity where deformations occur according to the equation of motion for bending waves displacement. The displacement of plate found to depend strongly on the applied force and on material properties.

The particle was assumed to adhere on the surface via a force estimated by the JKR theory. Momentum transfer from the plate to the particle causes particle motion in the same direction as the plate (vertical) as long as its mass inertia is overcome. Hence, the particle exhibits a force (of oscillation) which was obtained by Newton's second law of motion. Accordingly, the force of oscillation was estimated by the second derivate of the plate displacement and particle mass.

The conditions for particle resuspension were obtained using a simple force balance, where a particle is likely resuspended when the force of oscillation exceeds the adhesive force. It was found that the magnitude of the applied force, particle size and forcing frequency play the most dominant role. Therefore, high frequencies and an increase in the magnitude of the applied pressure favors particle resuspension due to the enhanced vibrating force. Although, particle size increases its mass inertia, resuspension was easier attainable because adhesives forces were easily overcome compared to a smaller particle.

Chapter 7

Conclusions and recommendations for future work

7.1 General conclusions

7.1.1 Measurement campaigns

The characteristics of workplace environments in terms of mass and number concentration of indoor particles were in examined in Chapter 2. The measurements took place in several offices equipped with mechanical ventilation in two different countries (Greece and Norway). The indoor environment was evaluated acknowledging the operation of the ventilation system, occupation scheme and human related sources. Accordingly, it was found that the contribution from the outdoor environment indoors was dominant when the offices were vacant. Both number and mass concentrations of indoor particles followed the profile of the outdoor particle (number and mass) concentration indicating a significant infiltration of outdoor particles indoors. This behavior was reported in the Norway campaign in cases where mechanical ventilation was on, although low I/O ratios were obtained due to the successful capture of the majority of the outdoor particles through filters.

On the other hand, indoor sources associated with office equipment were identified as the main contribution of ultrafine particles indoors. The printers located in one of the offices in the Greece campaign had considerable impact on indoor particle number and mass concentrations of fine particles in the same room as well as to fine particles to other offices due to effective transport indoors. Door configuration, internal layout and airflows essentially played an important role on particle transport. However, both campaigns highlighted the impact of the physical presence of the occupants in the offices, when no source that generates particles was present. In this case, office occupation had significant impact to coarse particles, which is associated with human resuspension activities (walking, moving objects).

In summary, both campaigns although located in different countries with different working conditions demonstrate that environmental conditions indoors in terms of particle concertation are subject to both indoor and outdoor contributions where primary emissions and particle dynamics determine the impact to the indoor environment.

7.1.2 Modeling of particle infiltration and resuspension

Particle dynamics determine the characteristics of infiltration from outdoors as shown in Chapter 3. The infiltration factor, obtained as a function of the air exchange rate, deposition rate and penetration efficiency, suggested that the most effective penetration and suspension to the indoor air lies in the accumulation size fraction (0.1 - 0.7 μm). Particles in this size range found to become airborne more effectively while penetrating from outdoors compared to ultrafine (< 0.1 μm) or coarse particles (> 0.7 μm). This behavior was directly associated with losses due to Brownian motion for ultrafine particles and losses due to gravitational settling for coarse particles.

In addition, the particle resuspension rate induced by human walking was calculated in Chapter 4 and was found independent of the initial dust loading on the floor. This finding clearly indicated that particle resuspension is primarily subject to the external force (walking) and that the resuspension rate depends on its magnitude. The results have also shown that particle resuspension is easier attainable for bigger particles. On the other hand, the initial dust loading on the floor determined the level of indoor particle concentrations such as higher dust loading resulted in higher ambient concentration.

In further investigation of the characteristics of particle resuspension a stochastic model was adopted where the likelihood for resuspension was obtained as the competition between external excitations and adhesive forces for resuspension due to the act of a turbulent airflow (Chapter 5). The model was applied to both a monolayer and a multilayer deposit. Monolayer resuspension was evaluated with respect to intermolecular interactions and the role of particle size, surface roughness and particle charge. The results suggested that all three variables play a significant role in the process. Particle size and the corresponding surface contact characteristics determines contact characteristics, whilst particle charge enhances the adhesive force between the particle and the surface. On the other hand, multilayer resuspension was evaluated in respect to single-layer resuspension rate. It was found that position of the particles in the deposit plays a dominant role with particles at top layers resuspend first. Moreover, the influence of the exposure time and friction velocity of the flow was associated with the behavior of the resuspension rate in two regimes, a short-term and a long-term regime. The short-term regime was characterized by high rates where different rates obtained for different layers, whereas, in the long-term regime the resuspension rate was decreased inversely with exposure time. In the latter, lower rates were obtained for higher friction velocity, however similar rates were found at different layers irrespectively of the position in the deposit.

Finally, a different approach for particle resuspension was presented in Chapter 6, where resuspension occurs due to an external vibrating force acting at a distance from the particle. In this case, the particle is

subject to vertical displacements (oscillations) onto the surface due to momentum transfer from the force to the particle through the surface. Accordingly, the particle is detached and eventually resuspended when the force of the vertical oscillations of the particle exceeds the adhesive force between the particle and the surface. Model predictions suggest that inclusion of surface roughness is necessary for particle resuspension and that the possibility increases for bigger particles, higher magnitude of the external force and higher driving frequencies.

7.2 Recommendations

A comprehensive knowledge of the different workplace environments is missing, since few experimental studies in modern offices can be found in literature. Future studies can focus on measurements in real offices to examine thoroughly the impact of both indoor and outdoor sources. Open-air offices can also be selected to investigate the impact from the ventilation system as well as the internal layout to indoor air quality.

The methodology used in modeling particle infiltration can be further applied to other indoor environments thus examine the impact of building characteristic to natural penetration from outdoors. Moreover, specific measurements should be used to investigate the effect of the walking speed in resuspension due to human walking as well as environmental conditions, variables which are still not adequate investigated.

Although, there are several resuspension models that have studied sufficiently particle motion and resuspension under the act of a turbulent airflow the impact of the turbulence on the particles is not clear, especially in the case of a multilayer deposit. Moreover, the present thesis highlighted the significance of contact characteristics to particle resuspension, hence caution is necessary in modeling of the appropriate particle-surface interaction. Lastly, particle resuspension due to surface vibration should be experimentally studied in order to evaluate theoretical predictions.

References

Abadie M., Limam K., Allard F. (2001). Indoor particle pollution: effect of wall textures on particle deposition. *Building and Environment*, 36, 821-827.

Abdullahi K.L., Delgado-Saborit J.M., Harrison R.M. (2013). Emissions and indoor concentrations of particulate matter and its specific components from cooking: A review. *Atmospheric Environment*, 71, 260-294.

Abt E., Suh H.H., Catalano P., Koutrakis P. (2000). Relative contribution of outdoor and indoor particle sources to indoor concentrations. *Environmental Science and Technology*, 34, 3579-3587.

Aniya M. (1997). Estimation of critical constants from boiling temperature and atomic parameters. *Physica B*, 239, 144-150.

Austin J., Brimblecombe P., Sturges W. (2002). Air pollution science for the 21st century. United Kingdom, Elsevier.

Barth T., Preuß J., Müller G., Hampel U. (2014). Single particle resuspension experiments in turbulent channel flows, *Journal of Aerosol Science*, 71, 40-51.

Bateman A.P., Belessein H., Martin S.T. (2014). Impactor apparatus for the study of particle rebound: Relative humidity and capillary forces. *Aerosol Science and Technology*, 48, 42-52.

Benito J.G., Valenzuela Aracena K.A., Uñac R.O., Vidales A.M., Ippolito I. (2015). Monte Carlo modelling of particle resuspension on a flat surface. *Journal of Aerosol Science*, 79, 126-139.

Bennett D.H., Koutrakis P. (2006). Determining the infiltration of outdoor particles in the indoor environment using a dynamic model. *Journal of Aerosol Science*, 37, 766-785.

Betha R., Selvam V., Blake D.R., Balasubramanian R. (2011). Emission characteristics of ultrafine particles and volatile organic compounds in a commercial printing center. *Journal of the Air and Waste Management Association*, 61, 1093-1101.

Biggs S., Cain R.G., Dagastine R.R., Page N.W. (2002). Direct measurements of the adhesion between a glass particle and a glass surface in a humid atmosphere. *Journal of Adhesion Science and Technology*, 16, 869-885.

Boor B.E., Siegel J.A., Novoselac A. (2013a). Monolayer and multilayer particle deposits on hard surfaces: Literature review and implications for particle resuspension in the indoor environment. *Aerosol Science and Technology*, 47, 831-847.

Boor B.E., Siegel J.A., Novoselac A. (2013b). Wind tunnel study on aerodynamic particle resuspension from monolayer and multilayer deposits on linoleum flooring and galvanized sheet metal. *Aerosol Science and Technology*, 47, 848-857.

Brimblecombe P., Blades N., Camuffo D., Sturaro G., Valentino A., Gysels K., Van Grieken R., Busse H.-J, Kim O., Ulrych U., Wieser M. (1999). The indoor environmental of a modern museum building, the Sainsbury Centre for Visual Arts, Norwick, UK. *Indoor Air*, 9, 146-164.

Broday D.M., Georgopoulos P.G. (2001). Growth and deposition of hygroscopic particulate matter in the human lungs. *Aerosol Science and Technology*, 34, 144-159.

Calvo A.I., Alves C., Castro A., Pont V., Vicente A.M., Fraile R. (2013). Research on aerosol sources and chemical composition: Past, current and emerging issues. *Atmospheric Research*, 120-121, 1-28.

Camuffo D., Brimblecombe P., Van Grieken R., Busse H.J., Sturaro G., Valentino A., Bernardi A., Blades N., Shooter D., De Bock L., Gysels K., Wieser M., Kim O. (1999). Indoor air quality at the Correr Museum, Venice, Italy. *Science of the Total Environment*, 236, 135-152.

Camuffo D., Van Grieken R., Busse H.J., Sturaro G., Valentino A., Bernardi A., Blades A., Blades N., Shooter D., Gysels K., Deutsch F., Wieser M., Kim O., Ulrych U. (2001). Enviromental monitoring in four European museums. *Atmospheric Environment*, 35, 127-140.

Cao J.J., Lee S.C., Chow J.C., Cheng Y., Ho K.F., Fung K., Liu S.X., Watson J.G. (2006). Indoor/outdoor relationships for $PM_{2.5}$ and associated carbonaceous pollutants at residential homes in Hong Kong – case study. *Indoor Air*, 15, 197-204.

Challoner A, Gill L. (2014). Indoor/outdoor air pollution relationships in ten commercial buildings: $PM_{2.5}$ and NO_2. *Building and Environment*, 80, 159-173.

Chalvatzaki E., Kopanakis I., Kontaksakis M., Glytsos T., Kalogerakis N., Lazaridis M. (2010). Measurements of particulate matter concentrations at a landfill site (Crete, Greece). *Waste Management*, 30, 2058-2064.

Chao C.Y.H., Wan M.P., Cheng E.C.K. (2003). Penetration coefficient and deposition rate as a function of particle size in non-smoking naturally ventilated residences. *Atmospheric Environment*, 37, 4233-4241.

Chatoutsidou S.E., Mašková L., Ondráčková L., Ondráček J., Lazaridis M., Smolík J. (2015). Modeling of the aerosol infiltration characteristics in a cultural heritage building: The Baroque Library Hall in Prague. *Building and Environment*, 89, 253-263.

Chatoutsidou S.E., Ondráček J., Tesar O., Tørseth K., Zdimal V., Lazaridis M. (2015). Indoor/outdoor particulate matter number and mass concentration in modern offices. *Building and Environment*, 92, 462-474.

Chen C., Zhao B. (2011). Review of relationship between indoor and outdoor particles: I/O ratio, infiltration factor and penetration factor. *Atmospheric Environment*, 45, 275-288.

Chen C., Zhao B., Zhou W., Jian X., Tan Z. (2012). A methodology for predicting particle penetration factor through cracks of windows and doors for actual engineering application. *Building and Environment*, 47, 339-348.

Chu C.-R., Chiu Y.-H., Tsai Y.-T., Wu S.-L. (2015). Wind-driven natural ventilation for buildings with two openings on the same external wall. *Energy and Buildings*, 108, 365-372.

Chung T.-H., Lee L.L., Starling K.E. (1984). Applications of kinetic gas theories and multiparameter correlation for prediction of dilute gas viscosity and thermal conductivity. *Industrial and Engineering Chemistry Fundamentals*, 23, 8-13.

Coleman B.K., Lunden M.M., Destaillats H., Nazaroff W.W. (2008). Secondary organic aerosol from ozone-intiated reactions with terpene-rich household products. *Atmospheric Environment*, 42, 8234-8245.

Congrong H., Morawska L., Gilbert D. (2005). Particle deposition rates in residential houses. *Atmospheric Environment*, 39, 3891-3899.

Corsi R.L., Siegel J.A., Chiang C. (2008). Particle resuspension during the use of vacuum cleaners on residential carpet. *Journal of Occupational and Environmental Hygiene*, 5, 232-238.

Czarnecki W.S., Schein L.B. (2004). Electrostatic force acting on a spherically symmetric charge distribution in contact with a conductive plane. *Journal of Electrostatics*, 61, 107-115.

D'Agostino D., Congedo P.M. (2014). CDF modeling and moisture dynamics implications of ventilation scenarios in historical buildings. *Building and Environment*, 79, 181-193.

Dennery P., Krzywicki A. (1996). Mathematics for physicists, Dover.

Derjaguin B.W., Muller V.M., Toporov Yu.P. (1975). Effect of contact deformation on the adhesion of particles. *Journal of Colloid and Interface Science*, 53, 314-326.

Destaillats H., Maddalena R.L., Singer B.C., Hodgson A.T., McKone T.E. (2008). Indoor pollutants emitted by office equipment: A review of reported data and information needs. *Atmospheric Environment*, 42, 1371-1388.

Diapouli E., Chaloukakou A., Koutrakis P. (2013). Estimating the concentration of indoor particles of outdoor origin: A review. *Journal of the Air and Waste Management Association*, 63, 1113-1129.

Ekberg L. (1996). Relationships between indoor and outdoor contaminants in mechanically ventilated buildings. *Indoor Air*, 6, 41-47.

El Orch Z., Stephens B., Waring M.S. (2014). Predictions and determinants of size-resolved particle infiltration factors in single-family homes in the U.S. *Building and Environment*, 74, 106-118.

Feuillebois F., Gensdarmes F., Mana Z., Ricciardo L., Monier C., Le Meur G., Reynaud C., Rabaud M. (2016). Three dimensional motion of particles in a shear flow near a rough wall. *Journal of Aerosol Science*, 96, 69-95.

Feng J.Q., Hays D.A. (2003). Relative importance of electrostatic forces on powder particles. *Powder Technology*, 135-136, 65-75.

Ferro A.R., Kopperud R.J., Hildemann L. (2004). Source strengths for indoor human activities that resuspend particulate matter. *Environmental Science and Technology*, 38, 1759-1764.

Fisk W.J., Faulkner D., Sullivan D., Mendell M.J. (2000). Particle concentrations and sizes with normal and high efficiency air filtration in a sealed air-conditioned office building. *Aerosol Science and Technology*, 32, 527-544.

Franck U., Herbarth O., Röder S., Schlink U., Borte M., Diez U., Krämer U., Lehmann I. (2011). Respiratory effects of indoor particles in young children are size dependent. *Science of the Total Environment*, 409, 1621-1631.

Friess H., Yadigaroglu G. (2001). A generic model for the resuspension of multilayer aerosol deposits by turbulent flow. *Nuclear Science and Engineering*, 138, 161-176.

Friess H., Yadigaroglu G. (2002). Modeling of the resuspension of particle clusters from multilayer aerosol deposits with variable porosity. *Journal of Aerosol Science*, 33, 883-906.

Ghedini N., Ozga I., Bonazza A., Dilillo M., Cachier H., Sabbioni C. (2011). Atmospheric aerosol monitoring as a strategy for the preventive conservation of urban monumental heritage: The Florence Baptistery. *Atmospheric Environment*, 45, 5979-5987.

Godoi R.H.M., Carneiro B.H.B., Paralovo S.L., Campos V.P., Tavares T.M., Evangelista H., Van Grieken R., Godoi A.F.L. (2013). Indoor air quality of a museum in a subtropical climate: The Oscar Niemeyer museum in Curitiba, Brazil. *Science of the Total Environment*, 452-453, 314-320.

Goldasteh I., Ahmandi G., Ferro A.R. (2013). Monte Carlo simulation of micron size spherical particle removal and resuspension from substrate under fluid flows. *Journal of Aerosol Science*, 66, 62-71.

Goldasteh I., Tian Y., Ahmadi G., Ferro A.R. (2014). Human induced flow field and resultant particle resuspension and transport during gait cycle. *Building and Environment*, 77, 101-109.

Gomes C., Freihaut J., Bahnfleth W. (2007). Resuspension of allergen-containing particles under mechanical and aerodynamic disturbances from human walking. *Atmospheric Environment*, 41, 5257-5270.

Guingo M., Minier J.-P. (2008). A new model for the simulation of particle resuspension by turbulent flows based on a stochastic description of wall roughness and adhesion forces. *Journal of Aerosol Science*, 39, 957-973.

Gysels K., Delalieux F., Deutsch F., Van Grieken R., Camuffo D., Bernardi A., Sturaro G., Busse H.-J., Wieser M. (2004). Indoor environment and conservation in the Royal Museum of Fine Arts, Antwerp, Belgium. *Journal of Cultural Heritage*, 5, 221-230.

He C., Morawska L., Taplin L. (2007). Particle emission characteristics of office printers. *Environmental Science and Technology*, 41, 6039-6045.

Henry C., Minier J.-P. (2014). Progress in particle resuspension from rough surfaces by turbulent flows. *Progress in Energy and Combustion Science*, 45, 1-53.

Hinds W.C. (1999). Aerosol Technology. New York, John Wiley & Sons**.**

Huang Y., Ho K.F., Ho S.S.H., Lee S.C., Yau P.S., Cheng Y. (2011). Physical parameters effect on ozone-initiated formation of indoor secondary organic aerosols with emissions from cleaning products. *Journal of Hazardous Materials*, 192, 1787-1794

Hussein T., Dada L., Juwhari H., Faouri D. (2015). Characterization, fate and re-suspension of aerosol particles (0.3-10 µm): The effects of occupancy and carpet use. *Aerosol and Air Quality Research*, 15, 2367-2377.

Hussein T., Glytsos T., Ondrácek J., Dohányosová P., Zdímal V., Hämeri K., Lazaridis M., Smolík J., Kulmala M. (2006). Particle size characterization and emission rates during indoor activities in a house. *Atmospheric Environment*, 40, 4285-4307.

Hussein T., Hruška A., Dohányosová P., Džumbová L., Hemerka J., Kulmala M., Smolík J. (2009). Deposition rates on smooth surfaces and coagulation of aerosol particles inside a test chamber. *Atmospheric Environment*, 43, 905-914.

Hu T., Lee S., Cao J., Chow J.C., Watson J.G., Ho K., Ho W., Rong B., An Z. (2009). Characterization of winter airborne particles at Emperor Qin's Terra-cotta Museum, China. *Science of the Total Environment*, 407, 5319-5327.

Ibrahim A.H., Dunn P.F., Brach R.M. (2003). Microparticle detachment from surfaces exposed to turbulent air flow: controlled experiments sand modeling. *Journal of Aerosol Science*, 34, 765-782.

Ibrahim A.H., Dunn P.F., Qazi M.F. (2008). Experiments and validation of a model for microparticle detachment from a surface by turbulent air flow. *Journal of Aerosol Science*, 39, 645-656.

Israelachvili J. (1992). Intermolecular and Surface Forces. Academic Press, London.

Jamriska M., Morawska L., Ensor D.C. (2003). Control strategies for sub-micrometer particles indoors: model study of air filtration and ventilation. *Indoor Air*, 13, 96-105.

Jiang Y., Matsusaka S., Masuda H., Qian Y. (2008). Characterizing the effect of substrate surface roughness on particle-wall interaction with the airflow method. *Powder Technology*, 186, 199-205.

Johnson K.L., Greenwood J.A. (1997). An adhesion map for the contact of elastic spheres. *Journal of Colloid Interface Science*, 192, 326-333.

Johnson K.L., Kendall K., Roberts A.D. (1971). Surface energy and the contact of elastic solids. *Proceedings of the Royal Society of London A*, 324, 301-313.

Kao H.M., Chang T.J., Hsieg Y.F., Wang C.H., Hsieg C.I. (2009). Comparison of airflow and particulate matter transport in multi-room buildings for different natural ventilation patterns. *Energy and Buildings*, 41, 966-974.

Koivisto A.J., Hussein T., Niemelä R., Tuomi T., Hämeri K. (2010). Impact of particle emissions of new laser printers on modeled office room. *Atmospheric Environment*, 44, 2140-2146.

Kopanakis, I., Chatoutsidou, S.E., Torseth, K., Glytsos, T., Lazaridis, M. (2013). Particle number size distribution in the eastern Mediterranean: Formation and growth rates of ultrafine airborne atmospheric particles. Atmospheric *Environment* 77, 790-802

Krupińska B., Van Grieken R., De Miel K. (2013). Air quality monitoring in a museum for preventive conservation: Results of a three-year study in the Plantin-Moretus Museum in Antwerp, Belgium. *Microchemical Journal*, 110, 350-360.

Kubota Y., Higuchi H. (2013). Aerodynamic particle resuspension due to human foot and model foot motions. *Aerosol Science and Technology*, 47, 208-217.

Kulkarni P., Barron P.A., Willeke K. (2011). Aerosol measurement: Principles, techniques and applications. Third Edition, John Wiley & Sons**.**

Lai A.C.K. (2002). Particle deposition indoors: a review. *Indoor Air*, 12, 211-214.

Lai A.C.K., Fung J.L.S., Leung K.Y. (2012). Penetration of fine particles through rough cracks. *Atmospheric Environment*, 60, 436-443.

Lai A.C.K., Nazaroff W.W. (2000). Modeling indoor particle deposition from turbulent flow onto smooth surfaces. *Journal of Aerosol Science*, 31, 463-476.

Landau LD., Lifshitz E.M. (1986). Theory of elasticity. Pergamon Press 3rd Edition.

LaRosa L.E., Buckley T.J., Wallace L.A. (2002). Real-time indoor and outdoor measurements of black carbon in an occupied house: An examination of sources. *Journal of the Air and Waste Management Association*, 52, 41-49.

Lazaridis M., Drossinos Y., Georgopoulos P.G. (1998). Turbulent resuspension of small nondeformable particles. *Journal of Colloid Interface Science*, 204, 24-32.

Lazaridis M., Drossinos Y. (1998). Multilayer resuspension of small identical particles by turbulent flow. *Aerosol Science and Technology*, 28, 548-560.

Lazaridis M., Dzumbova L., Kopanakis I., Ondracek J., Glytsos T., Alexandropoulou V., Voulgarakis A., Katsivela E., Michalopoulos N., Eleftheriadis K. (2008). PM_{10} and $PM_{2.5}$ levels in the Eastern Mediterranean (Akrotiri research station, Crete, Greece). *Water Air and Soil Pollution,* 189, 85-101.

Lecrivain G., Vitsas A., Boudounis A.G., Hampel U. (2014). Simulation of multilayer particle resuspension in an obstructed channel flow. *Powder Technology*, 263, 142-150.

Leighton D., Acrivos A. (1985). The lift on a small sphere touching a plane in the presence of a simple shear flow. *Journal of Applied Mathematics and Physics*, 36, 174-178.

Leung W.T., Fu S.C., Sze To G.N., Chao C.Y.H. (2013). Comparison of the resuspension behaviour between liquid and solid aerosols. *Aerosol Science and Technology*, 47, 1239-1247.

Liao C.M., Huang S.J., Yu H. (2004). Size-dependent particulate matter indoor/outdoor relationships for wind-induced naturally ventilated airspace. *Building and Environment*, 39, 411-420.

Liddament M.W. (2000). A review of ventilation and the quality of ventilation air. *Indoor Air*, 10, 193-199.

Liu D.-L., Nazaroff W.W. (2001). Modeling pollutants penetration across building envelopes. *Atmospheric Environment*, 35, 4451-4462.

Long C.M., Sarnat J.A. (2004). Indoor-outdoor relationships and infiltration behavior of elemental components of outdoor $PM_{2.5}$ for Boston-area homes. *Aerosol Science and Technology*, 38, 91-104.

Long C.M., Suh H.H., Catalano P.J., Koutrakis P. (2001). Using time- and size- resolved particulate data to quantify indoor penetration and deposition behavior. *Environmental Science and Technology*, 35, 2089-2099.

López-Aparicio S., Smolík J., Mašková L., Součková M., Grøntoft T., Ondráčková L., Stankiewicz J. (2011). Relationship of indoor and outdoor air pollutants in a naturally ventilated historical building envelope. *Building and Environment*, 46, 1460-1468.

Martinez R.C., Sweeney L.G., Finlay W.H. (2009). Aerodynamic forces and moment on a sphere or cylinder attached to a wall in Blasius boundary layer. *Engineering Applications of Computational Fluid Mechanics*, 3, 289-295.

Matson U. (2005). Indoor and outdoor concentrations of ultrafine particles in some Scandinavian rural and urban areas. *Science of the Total Environment*, 343, 169-176.

Maugis D. (1992). Adhesion of spheres: the JKR-DMT transition using a Dugdale model. *Journal of Colloid and Interface Science*, 150, 243-269.

McAuley T.R., Fisher R., Zhou X., Jaques P.A., Ferro A.R. (2010). Relationships of outdoor and indoor ultrafine particles at residences downwind of a major international border crossing in Buffalo, NY. *Indoor Air*, 20, 298-308.

McGarry P., Morawska L., He C., Jayaratne R., Falk M., Tran Q., Wang H. (2011). Exposure to particles from laser printers operating within office workplaces. *Environmental Science and Technology*, 45, 6444-6452.

McGrath J.A., Byrne M.A., Ashmore M.R., Terry A.C., Dimitropoulou C. (2014). Development of a probabilistic multi-zone multi-source computational model and demonstration of its applications in predicting PM concentrations indoors. *Science of the Total Environment*, 490, 798-806.

Morawska L., Asfari A., Bae G.N., Buonanno G., Chao C.Y.H., Hänninen O., Hofmann W., Isaxon C., Jayarantne E.R., Pasanen P., Salthammer T., Waring M., Wierzbicka A. (2013). Review Article, Indoor aerosols: from personal exposure to risk assessment. *Indoor Air*, 23, 462-487.

Morawska L., He C., Johnson G., Jayaratne R., Salthammer T., Wang H., Uhde E., Bostrom T., Modini R., Ayoko G., McGarry P., Wensing M. (2009). An investigation into the characteristics and formation mechanisms of particles originating from the operation of laser printers. *Environmental Science and Technology*, 43, 1015-1022.

Morawska L., Salthammer T. (2003). Indoor environment, Airborne particles and settled dust. Willey-VCH GmbH & Co. KGaA.

Muller V.M., Yushchenko V.S., Derjaguin B.M. (1980). On the influence of molecular forces on the deformation of an elastic sphere and its sticking to a rigid plane. J*ournal of Colloid and Interface Science*, 77, 91-101.

Nazaroff W.W. (2004). Indoor particle dynamics. *Indoor Air*, 14, 175-183.

Nazaroff W.W., Weschler C.J. (2004). Cleaning products and air fresheners: exposure to primary and secondary air pollutants. *Atmospheric Environment*, 38, 2841-2865.

Nicholson K.W. (1988). A review of particle resuspension. *Atmospheric Environment*, 22, 2639-2651.

Nøraard A.W., Kudal A.W., Kofoed-Sørensen V., Koponen I.K., Wolkoff P. (2014). Ozone-initiated VOC and particle emissions from a cleaning agent and an air freshener: Risk assessment of acute airway effects. *Environmental International*, 68, 209-218.

Oberoi R.C., Choi J., Edwards J.R., Rosati J.A., Thornburg J., Rodes C.E. (2010). Human-induced particle re-suspension in a room. *Aerosol Science and Technology*, 45, 216-229.

O'Neil M.E. (1968). A sphere in contact with a plane wall in a slow linear shear flow. *Chemical Engineering Science*, 23, 1293-1298.

Ott W.R., Siegmann H.C. (2006). Using multiple continuous fine particle monitors to characterize tobacco, incense, candle, cooking, wood burning, and vehicular sources in indoor, outdoor, and in transit settings. *Atmospheric Environment*, 40, 821-843.

Park J.S., Jee N.-Y., Jeong J.-W. (2014). Effects of types of ventilation system on indoor particle concentrations in residential buildings. *Indoor Air*, 6, 629-638.

Poling B.E., Prausnitz J.M., O'Connell J.P. (2001). The properties of gases and liquids. McGraw-Hill, New York.

Pope C.A. III, Dockery W.D (2006). Health effects of fine particulate air pollution: Lines that connect. *Journal of the Air and Waste Management Association*, 56, 709-742.

Prokopovich P., Starov V. (2011). Adhesion models: From single to multiple asperity contacts. *Advances in Colloid and Interface Science*, 168, 210-222.

Qian J., Ferro R. (2008). Resuspension of dust particles in a chamber and associated environmental factors. *Aerosol Science and Technology*, 42, 566-578.

Qian J., Ferro R., Fowler K.R. (2008). Estimating the resuspension rate and residence time of indoor particles. *Journal of the Air and Waste Management Association*, 58, 502-516.

Qian J., Peccia J., Ferro A.R. (2014). Review: Walking-induced particle resuspension in indoor environments. *Atmospheric Environment*, 89, 464-481.

Quang T.N., He C., Morawska L., Knibbs L.D. (2013). Influence of ventilation and filtration on indoor particle concentrations in urban office buildings. *Atmospheric Environment*, 79, 41-52.

Reche C., Rivas I., Pandolfi M., Viana M., Bouso L., Àlvarez-Pedrerol M., Alastuey A., Sunyer J., Querol X. (2015). Real-time indoor and outdoor measurements of black carbon at primary schools. *Atmospheric Environment*, 120, 417-426.

Reeks M.W., Reed J., Hall. D. (1988). On the resuspension of small particles by a turbulent flow. *Journal of Physics D: Applied Physics*, 21, 574-589.

Reeks M.D., Hall D. (2001). Kinetic models for particle resuspension in turbulent flows: theory and measurement. *Journal of Aerosol Science*, 32, 1-31.

Rim D., Wallace L., Persily A. (2010). Infiltration of outdoor ultrafine particles into a test house. *Environmental Science and Technology*, 44, 5908-5913.

Rim D., Persily A., Emmerich S., Dols W.S., Wallace L. (2013). Multi-zone modelling of size-resolved outdoor ultrafine particle entry into a test house. *Atmospheric Environment*, 69, 219-230.

Rosati J.A., Thornburg J., Rodes C. (2008). Resuspension of particulate matter from carpet due to human activity. *Aerosol Science and Technology*, 42, 472-482.

Saleh R., Shihadeh A. (2007). Hygroscopic growth and evaporation in an aerosol with boundary heat and mass transfer. *Journal of Aerosol Science*, 38, 1-16.

Salthammer T., Schripp T., Uhde E., Wensing M. (2012). Aerosols generated by hardcopy devices and other electrical appliances. *Environmental Pollution*, 169, 167-174.

Sangiorgi G., Ferrero L., Ferrini B.S., Lo Porto C., Perrone M.G., Zangrando R., Gambaro A., Lazzati Z., Bolzacchini E. (2013). Indoor airborne particle sources and semi-volatile partitioning effect of outdoor fine PM in offices. *Atmospheric Environment*, 65, 205-214.

Sarigiannis D.A., Karakitsios S.P., Gotti A., Liakos I.L., Katsoyiannis A. (2011). Exposure to major volatile organic compounds and carbonyls in European indoor environments and asssociated health risk. *Environmental International*, 37, 743-765.

Sarwar G., Olson D.A., Corsi R.L., Weschler C.J. (2004). Indoor fine particles: The role of terpene emissions from consumer products. *Journal of the air and Waste Management Association* 54, 367-377.

Schneider T., Kildesø J., Breum N.O. (1999). A two compartment model for determining the contribution of sources, surface deposition and resuspension to air and surface dust concentration levels in occupied rooms. *Building and Environment*, 34, 583-595.

Schripp T., Wensing E.U., Salthammer T., He C., Morawska L. (2008). Evaluation of ultrafine particle emissions from laser printers using emission test chambers. *Environmental Science and Technology*, 42, 4338-4343.

Seinfeld J.H., Pandis S.N. (2006). Atmospheric chemistry and physics: From air pollution to climate change. New York, John Wiley & Sons**.**

Serfozo N., Chatoutsidou S.E., Lazaridis M. (2014). The effect of particle resuspension during walking activity to PM_{10} mass and number concentrations in an indoor microenvironment. *Building and Environment*, 82, 180-189.

Shaughnessy R., Vu H. (2012). Particle loadings and resuspension related to floor coverings in chamber and in occupied school environments. *Atmospheric Environment*, 55, 515-524.

Soltani M., Ahmadi G. (1995). Particle detachment from rough surfaces in turbulent flows. *Journal of Adhesion*, 51, 105-123.

Stephens B., Siegel J.A. (2012). Penetration of ambient submicron particles into single-family residences and associations with building characteristics. *Indoor Air*, 22, 501-513.

Szigeti T., Kertész Z., Dunster C., Kelly F.J., Záray G., Mihucz V.G. (2014). Exposure to $PM_{2.5}$ in modern office buildings through elemental characterization and oxidative potential. *Atmospheric Environment*, 94, 44-52.

Tabor D. (1977). Surface forces and surface interactions. *Journal of Colloid and Interface Science*, 58, 2-13.

Takeuchi M. (2006). Adhesion forces of charged particles. *Chemical Engineering Science*, 61, 2279-2289.

Taylor J., Shrubsole C., Davies M., Biddulph P., Das P., Hamilton I., Vardoulakis S., Mavrogianni A., Jones B., Oikonomou E. (2014). The modifying effect of the building envelope on population exposure to $PM_{2.5}$ from outdoor sources. *Indoor Air*, 24, 639-651.

Taylor B.J., Webster R., Imbabi M.S. (1999). The building envelope as an air filter. *Building and Environment*, 34, 353-361.

Thatcher T.L., Layton D.W. (1995). Deposition, resuspension, and penetration of particles within a residence. *Atmospheric Environment*, 29, 1487-1497.

Thatcher T.L., Lunden M.M., Revzan K.L., Sextro R.G., Brown N.J. (2003). A concentration rebound method for measuring particle penetration and deposition in the indoor environment. *Aerosol Science and Technology*, 37, 847-864.

Thornburg J., Ensor D.S., Rodes C.E., Lawless P.A., Sparks L.E., Mosley R.B. (2001). Penetration of particles into buildings and associated physical factors. Part I: Model development and computer simulations. *Aerosol Science and Technology*, 34, 284-296.

Tian Y., Sul K., Qian J., Mondal S., Ferro A.R. (2014). A comparative study of walking-induced dust resuspension using a consistent test mechanism. *Indoor Air*, 24, 592-603.

Tian L., Zhang G., Jinghua T., Zhou J., Zhang Q. (2009). Mathematical model of particle penetration through smooth/rough building envelop leakages. *Building and Environment*, 44, 1144-1149.

Tsai C.-J., Pui D.Y.H., Liu B.Y.H. (1991). Elastic flattening and particle adhesion. *Aerosol Science and Technology*, 15, 239-255.

Tunno B.J., Shields K.N., Cambal L., Tripathy S., Holguin F., Lioy P., Clougherty J.E. (2015). Indoor air sampling for fine particulate matter and black carbon in industrial communities in Pittsburg. *Science of the Total Environment*, 536, 108-115.

Vainshtein P., Ziskind G., Fichman M., Gutfinger C. (1997). Kinetic model of particle resuspension by drag force. *Physical Review Letters*, 78, 551-554.

van Hout R. (2013). Spatially and temporally resolved measurements of bead resuspension and saltation in a turbulent water channel flow. *Journal of Fluid Mechanics*, 715, 389-423.

Varas-Muriel M.J., Fort R., Martínez-Garrido M.I., Zorona-Indart A., López-Arce P. (2014). Fluctuations in the indoor environment in Spanish rural churches and their effects on heritage conservation: Hydro-thermal and CO_2 conditions monitoring. *Building and Environment*, 82, 92-109.

Vette A.F., Rea A.W., Lawless P.A., Rodes C.E., Evans G., Highsmith V.R., Sheldon L. (2001). Characterization of indoor-outdoor aerosol concentration relationships during the Fresno PM exposure studies. *Aerosol Science and Technology*, 34, 118-126.

Viana M., Díez S., Reche C. (2011). Indoor and outdoor sources and infiltration processes of PM1 and black carbon in an urban environment. *Atmospheric Environment*, 2011, 6359-6367.

Wallace L.A., Emmerich S.J., Howard-Reed C (2004). Effect of central fans and in-ducts filters on deposition rates of ultrafine and fine particles in an occupied townhouse. *Atmospheric Environment*, 38, 405-13.

Walton O.R. (2008). Review of adhesion fundamentals for micron-scale particles. *Kona Powder and Particle Journal*, No.26.

Wang H.-C. (1990). Effects of inceptive motion on particle detachment from surfaces. *Aerosol Science and Technology*, 13, 386-393.

Wang X., Chen R., Meng X., Geng F., Wang C., Kan H. (2013). Associations between fine particle, coarse particle, black carbon and hospital visits in a Chinese city. *Science of the Total Environment*, 458-460, 1-6.

Wang S., Zhao B., Zhou B., Tan Z. (2012). An experimental study on short-time particle resuspension from inner surfaces of straight ventilation ducts. *Building and Environment*, 53, 119-127.

Wen H.Y., Kasper G. (1989). On the kinetics of particle re-entrainment from surfaces. *Journal of Aerosol Science*, 20, 483-498.

Wensing M., Schripp T., Uhde E., Salthammer T. (2008). Ultra-fine particles release from hardcopy devices: Sources, real-room measurements and efficiency of filter accessories. *Science of the Total Environment*, 407, 418-27.

Weschler C.J. (2000). Ozone in the indoor environments: Concentration and chemistry. *Indoor Air*, 10, 269-288.Worobiec A., Samek L., Karaszkiewicz P., Kontozova-Deutsch V., Stefaniak E.A., Van Meel K, Krata A., Bencs L., Van Grieken R. (2008). A seasonal study of atmospheric conditions influenced by the intensive tourist flow in the Royal Museum of Wawel Castle in Cracow, Poland. *Microchemical Journal*, 90, 99-106.

Worobiec A., Samek L., Krata A., Van Meel K., Krupinska B., Stefaniak E.A., Karaszkiewicz, Grieken R.V. (2010). Transport and deposition of airborne pollutants in exhibition areas located in historical buildings-study in Wawel Castle Museum in Cracow, Poland. *Journal of Cultural Heritage*, 11, 354-359.

Wu Y.-L., Davidson C.I., Russel A.G. (1992). Controlled wind tunnel experiments for particle bounceoff and resuspension. *Aerosol Science and Technology*, 17, 245-262.

Xu M., Nematollahi M., Sextro R.G., Gadgil A.J. (1994). Deposition of tobacco smoke particles in a low ventilation room. *Aerosol Science and Technology*, 20, 194-206.

Zhang X., Ahmadi G., Qian J., Ferro A.R. (2008). Particle detachment, resuspension and transport due to human waling in indoor environments. *Journal of Adhesion Science and Technology*, 22, 591-621.

Zhang F., Reeks M., Kissane, M. (2013). Particle resuspension in turbulent boundary layers and the influence of non-Gaussian removal forces. *Journal of Aerosol Science*, 58, 103-128.

Zhao L., Chen C., Wang P., Chen Z., Cao S., Wang Q., Xie G., Wan Y., Wang Y., Lu B. (2015). Influence of atmospheric fine particulate matter ($PM_{2.5}$) pollution on indoor environment during winter in Beijing. *Building and Environment*, 87, 283-291.

Zhou H., Götzinger M., Peukert W. (2003). The influence of particle charge and roughness on particle-surface substrate adhesion. *Powder Technology*, 135-136, 82-91.

Zhu Y., Yang L., Meng C., Yuan Q., Yan C., Dong C., Sui X., Yao L., Yang F., Lu Y., Wang W. (2015). Indoor/outdoor relationships and diurnal/nocturnal variations in water-soluble ion and PAH concentrations in the atmospheric $PM_{2.5}$ of a business office area in Jinan, a heavily polluted city in China. *Atmospheric Research*, 153, 276-285.

Ziskind G., Fichman M., Gutfinger C. (1995). Resuspension of particulates from surfaces to turbulent flows-Review and analysis. *Journal of Aerosol Science*, 26, 613-644.

Ziskind G., Fichman M., Gutfinger C. (1997). Adhesion moment model for estimating particle detachment from a surface. *Journal of Aerosol Science*, 28, 623-634.

Appendix A: Publications

The following journal and conference articles were published or presented within the present phd thesis.

A.1 Scientific Journals (Peer Reviewed)

Relative to the present thesis

1. Serfozo N., **Chatoutsidou S.E.**, Lazaridis M. The effect of particle resuspension during walking activity to PM_{10} mass and number concentrations in an indoor microenvironment. Building and Environment 2014, 82, 180-89.

2. **Chatoutsidou S.E.**, Mašková L., Ondráčková L., Ondráček J., Lazaridis M., Smolík J. Modeling of the aerosol infiltration characteristics in a cultural heritage building: The Baroque Library Hall in Prague. Building and Environment 2015, 89, 253-263.

3. **Chatoutsidou S.E.**, Ondráček J., Tesar O., Tørseth K., Zdimal V., Lazaridis M. Indoor/Outdoor particulate matter number and mass concentration in modern offices. Building and Environment 2015, 92, 462-474.

4. **Chatoutsidou S.E.**, Drossinos Y., Tørseth K., Lazaridis M. Modeling of particle resuspension by a turbulent flow and the role of particle size, surface roughness and electric charge. Submitted in Journal of Adhesion Science and Technology.

5. **Chatoutsidou S.E.**, Serfozo N., Glytsos T., Lazaridis M. Multi-zone measurement of particle concentrations in a HVAC building with massive printer emissions: influence of human occupation and transport indoors. Under preparation.

6. **Chatoutsidou S.E.**, Drossinos Y., Lazaridis M. Modeling of particle resuspension from multilayer deposits in a turbulent boundary layer: evaluation of the resuspension rate and single-layer kinetics. Under preparation.

7. **Chatoutsidou S.E.**, Kevrekidis P.G., Drossinos Y., Lazaridis M. Particle resuspension due to surface vibration. Under preparation.

Other

1. Kopanakis I., **Chatoutsidou S.E.**, Torseth K., Glytsos T., Lazaridis M. Particle number size distribution in the eastern Mediterranean: Formation and growth rates of ultrafine airborne atmospheric particles. Atmospheric environment 2013, 77, 790-802.

2. Lazaridis M., Serfozo N., **Chatoutsidou S.E.**, Glytsos T. New particle formation events arising from painting materials in an indoor microenvironment. Atmospheric Environment 2015, 102, 86-95.

A.2 Conferences

1. **Chatoutsidou S.E.**, Serfozo N., Kopanakis I., Glytsos T., Lazaridis M. The effect of controlled indoor activities on the particulate matter mass and number concentrations. European Aerosol Conference, Prague, Czech Republic, 1-6 September 2013.

2. **Chatoutsidou S.E.**, Mašková L., Lazaridis M., Smolík J. Modeling of particulate matter infiltration in the Baroque Library Hall in Prague. 11th International Conference Indoor Air quality in Heritage and Historic Environments, Prague, Czech Republic, 13-16 April 2014**.**

3. **Chatoutsidou S.E.**, Drossinos Y., Lazaridis M. A stochastic model of particle resuspension by turbulent fluid flow. Conference on Aerosol Technology, Karlsruhe, Germany, 16-18 June 2014.

4. **Chatoutsidou S.E.**, Drossinos Y., Lazaridis M. Multilayer resuspension rate of deposits in turbulent flows. European Aerosol Conference, Milan, Italy, 6-11 September 2015.

5. **Chatoutsidou S.E.**, Ondráček J., Tesar O., Tørseth K., Zdimal V., Lazaridis M. Indoor particle number and mass concentrations in modern offices in Norway. 4th Workplace and Indoor Aerosols Conference, Barcelona, Spain, 20-22 April 2016.

6. **Chatoutsidou S.E.**, Serfozo N., Glytsos T., Lazaridis M. Multi-zone measurement of particle number/mass concentrations and black carbon in a HVAC building equipped with a printer room. European Aerosol Conference, Tours, France, 4-9 September 2016.

7. **Chatoutsidou S.E.**, Drossinos Y., Lazaridis M. Role of particle size and surface roughness on intermolecular interactions during particle resuspension from a turbulent flow. European Aerosol Conference, Tours, France, 4-9 September 2016.